Monte Carlo Simulation of Medical Accelerator Electron Treatment Heads

Tuathan O'Shea

August 2011

Submitted in accordance with the requirements for the degree of Doctor of Philosophy

School of Physics,
National University of Ireland Galway,
Ireland

Research Supervisor: Mark J. Foley, Ph.D.

Declaration

This candidate confirms that the work submitted is his own and that appropriate credit has been given to the work of others. The work in this thesis has not been submitted elsewhere for any other degree or qualification.

Table of Contents

List of Tables

List of Figures

Abstract

Monte Carlo simulation is an accurate and detailed method of modelling the complex electron source configurations and geometries seen in radiation therapy. It is known to be very accurate when used properly for patient specific dose calculations. This thesis was concerned with the development of accelerator treatment head models which could provide the details of the beam incident on the patient needed for complex electron treatment planning. An accurate treatment head model was developed which accounted for the measured asymmetries in the actual beam. This included the influence of a magnetic field in the treatment head previously unaccounted for. The treatment head model was used to investigate a novel method of electron beam delivery for breast treatment. The method was found to produce dose distributions similar to the conventional method, with the potential for faster and more complex treatments.

Acknowledgements

I would like to start by thanking my supervisor Dr. Mark Foley for enabling me to undertake this Ph.D. project and his support and guidance throughout this work. I would equally like to thank Prof. Bruce Faddegon for allowing me to contribute to his research and his supervision while I carried out research at University of California San Francisco.

I would like to thank Dr. David Rajasekar, Ms. Margaret Moore, Dr. Christoph Kleefeld and Prof. Wil van der Putten (University Hospital Galway) for useful discussion and information during the course of this work. I would also like to thank the medical physics team in the radiotherapy department at University Hospital Galway for the physical measurements used in chapter 2.

I would like to thank Dr. Patrick Downes (Cardiff University) and Dr. Darren Sawkey (Varian Medical Systems, Inc) for discussion and critique during this project. Special thanks to Erwin Garde and Omar Chacon (Engineers at University of California San Francisco) who were always there to help me out when the research accelerator (chapter 3 and 4) invariably had operational issues. Thanks also to Prof. James Lockhart (San Francisco State University) for the loan of the Tesla-meter which was used to make the magnetic field measurements in chapter 4. Thanks to Dr. Yuanyuan Ge (University of Sydney) for her assistance in taking the physical measurements used in chapter 5 and Dr. Naomi Schechter, MD (University of California San Francisco) for use of the patient data.

I would like to acknowledge the friendship of fellow graduate students and post-docs at National University of Ireland Galway and University of California San Francisco including: Arlene, Brendan, Jeff, Julian, Jungwook, Mareike, Punit and Utako. Thanks to Megan for her love and support during a large part of this work. I would also like to thank all my friends for their friendship and interest.

Finally I wish to acknowledge and thank my family who have always been there for me, shown interest and been supportive throughout this work (special thanks to my sister Marysia for reading).

1. Introduction

1.1 BIOLOGICAL EFFECTS AND THE GOAL OF RADIATION THERAPY

Biological effects of radiation are primarily the result of damage to the deoxyribonucleic acid (DNA) in the cell nucleus. When cells are exposed to ionizing radiation, radiochemical damage can occur either by direct or indirect action. Direct action occurs when radiation creates ions which physically break one or both of the sugar phosphate backbones or break the base pairs of the DNA. Direct action is the dominant process for high (> 10 keV / μm) linear energy transfer (LET) particles, such

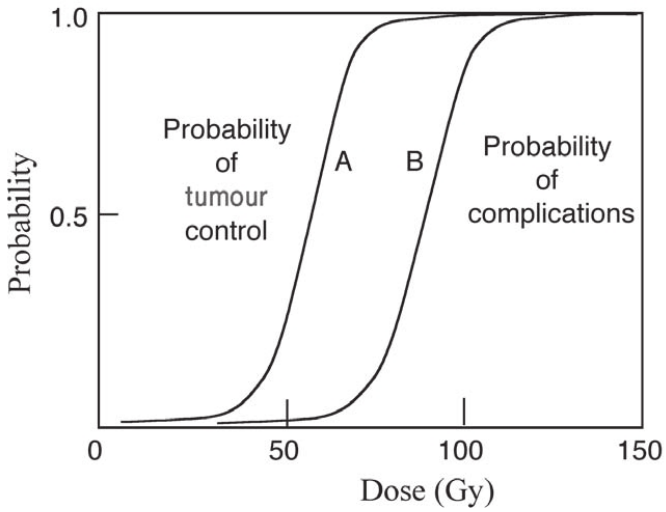

Figure 1.1 Tumour control probability (TCP) and normal tissue complication probability (NTCP) as a function of dose (reproduced from Podgorsak 2005).

as, neutrons, protons and heavy charged particles. Ionising radiation can also damage cells indirectly. The radiation interacts with molecules and atoms (mainly water) to create free radicals, such as, H_2O^+ and OH·, which can diffuse in the cell and damage the DNA. Approximately two thirds of the biological damage caused by low LET radiation, for example, megavoltage x-rays and electrons (LET < 0.5 keV/μm), is the result of this indirect action.

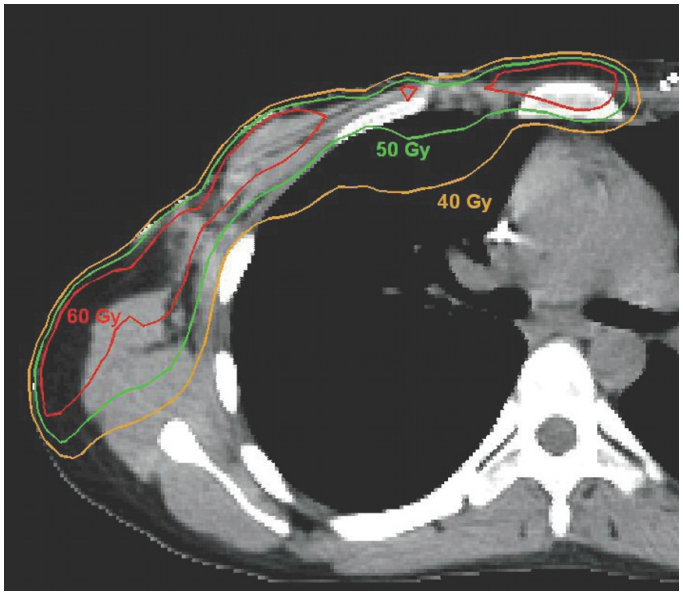

Figure 1.2 Treatment plan for right chest wall using one gantry angle and treatment table position and four electron beam segments with energies ranging from 6 to 16 MeV. The aim is to conform the radiation dose to the chest wall and limit the dose to the underlying lung and heart tissue (reproduced from Klein et al. 2009).

The goal of radiation therapy is to erradicate the tumour while maintaining - as

low as possible - a risk of irreversible complications to surrounding healthy tissues. Figure 1.1 shows the trade-off between tumour control (TCP) and normal tissue complication (NTCP) probablities. An optimum radiation dose delivery technique will maximise TCP while simulataneously minimising NTCP. Typical values of TCP and NTCP for an optimised radiation treatment are ≥0.5 and ≤0.05, respectively. From Figure 1.1 it is apparent that the larger the distance of curve B (NTCP) from curve A (TCP), the less likely it is that a treatment will cause unwanted complications. However, living tissues have different radiosensitivities and in some cases curves A and B will not be as widely seperated. For example, treatment of breast carcinoma requires an absorbed dose of 60 – 70 Gy, however, the normal tissue tolerance for the underlying lung tissue is approximately 20 Gy (Goldman et al. 2010). The ability to achieve the goal of a radiation therapy treatment is dependent on many factors including dose rate, LET, design of the treatment plan and accuracy of implementation of the treatment plan. Continual research effort is concerned with achieving higher dose conformality to the target (tumour), while sparing the surrounding normal tissues (e.g. figure 1.2).

1.2 DEVELOPMENT OF THE MEDICAL LINEAR ACCELERATOR

The x-ray was discovered by Wilhelm Röntgen on November 8th 1895. On December 22nd, Röntgen succesfully took the first x-ray image which showed the bones of his wife's hand (figure 1.3). Within weeks of this discovery, Henri Becquerel observed that

uranium salts emitted these *rays* and radioactivity had been discovered. Becquerel and others developed erythema from carrying small samples of uranium in their pockets. Several physicians learned of this and began investigating the effects on malignant tumours. The first therapeutic use of x-rays is reported to have taken place on January 29th 1899 for the treatment of a breast carcinoma.

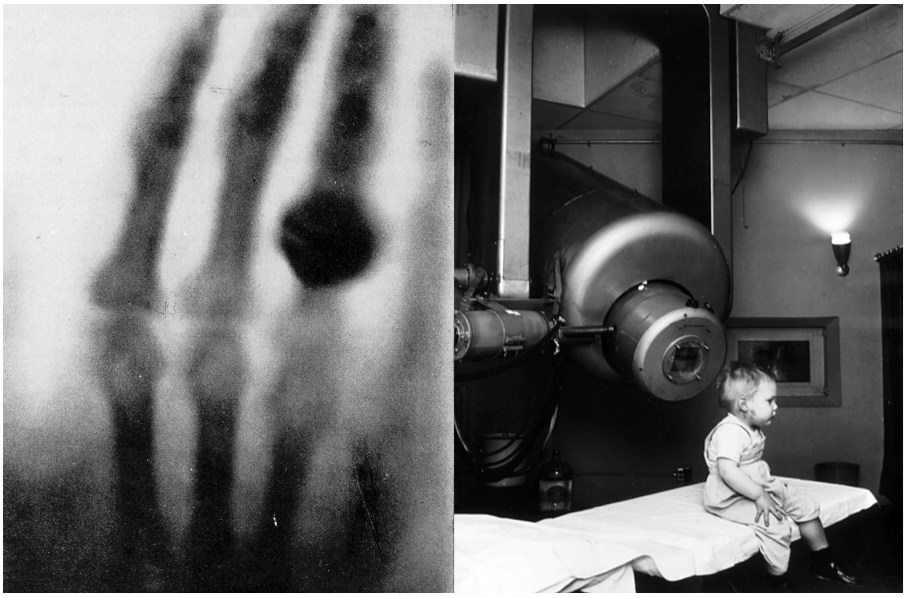

Figure 1.3 The first x-ray image (1895, left) and the first patient treated with linear accelerator radiation therapy for retinoblastoma (1957, right).

Prior to the 1950s, nearly all external beam radiation therapy was carried out with x-rays generated at voltages below 300 kVp. Superficial units operating at 50 - 120 kVp had poor penetrating ability with a high dose at the skin surface. In the 1920s

William Collidge invented a vacuum x-ray tube capable of operating at 200 – 250 kVp. This ortho-voltage device was capable of treating deeper tumours without excessive injury to the overlying skin.

The first linear accelerator (linac) was developed by Wideroe in 1928. Wideroe showed that heavy ions could be accelerated across the gaps between a series of drift tubes using an oscillating radio frequency voltage (Wideroe 1928). Although this was useful for heavy ions, the method was impractical for accelerating electrons because the high velocity of the electrons would require unrealistically long drift tubes. During World War II, high power and frequency microwave power sources were developed for RADAR applications. These microwave power sources, the klystron and magnetron, had intensities and frequencies high enough for linear acceleration of electrons to megavolt energies.

Teletherapy units employing cobalt-60 (^{60}Co) developed in the 1950s were a significant breakthrough, making megavoltage beams affordable and practical. High energy betatrons were introduced at approximately the same time as cobalt-60 units. Betatrons used varying magnetic fields to accelerate electrons in a circular path. The high energy beam could then be extracted for therapeutic application. Mega-voltage beams offered improved percentage depth dose (cf. figure 1.12) and skin sparing, as the maximum dose was deposited at some depth under the skin surface. Another advantage was that the high energy beam was more forward directed and had sharper penumbra

(field edge). This allowed treatment with higher doses to the lesion thereby reducing erythema or damage to lateral tissue.

Between the late 1940s and mid 1950s, the first electron linacs were designed and built by two groups working independently in Great Malvern, England and Palo Alto, California. The first clinical linac was installed at Hammersmith Hospital, London in June 1952 with the first patient treatment in August 1953 (Batchelor et al. 1959). The linac utilised a 2 MW magnetron and 3 m waveguide with a rotatable 90° magnet at the end. The 8 MeV x-ray beam was typically operated at 100 cGy/min. Following these early successes, Varian Associates (now Varian Medical Systems, Inc.) introduced a fully rotational 6 MeV linac in 1962 and 4 MeV x-ray linac in 1969 (Ginzton and Nunan 1985). The design was extremely reliable and became one of the keys to the widespread acceptance of linacs by the radiation therapy community.

1.3 THE MODERN LINEAR ACCELERATOR

In strict context, the linear accelerator is only one component of the radiation treatment system in which electrons are accelerated to a required mega-voltage energy. Modern linear accelerators provide several clinical electron and x-ray (photon) beams in the nominal kinetic energy range of approximately 4 MeV to 25 MeV. Megavoltage x-ray beams may be used to treat deep-seated tumours, with the characteristics of the dose

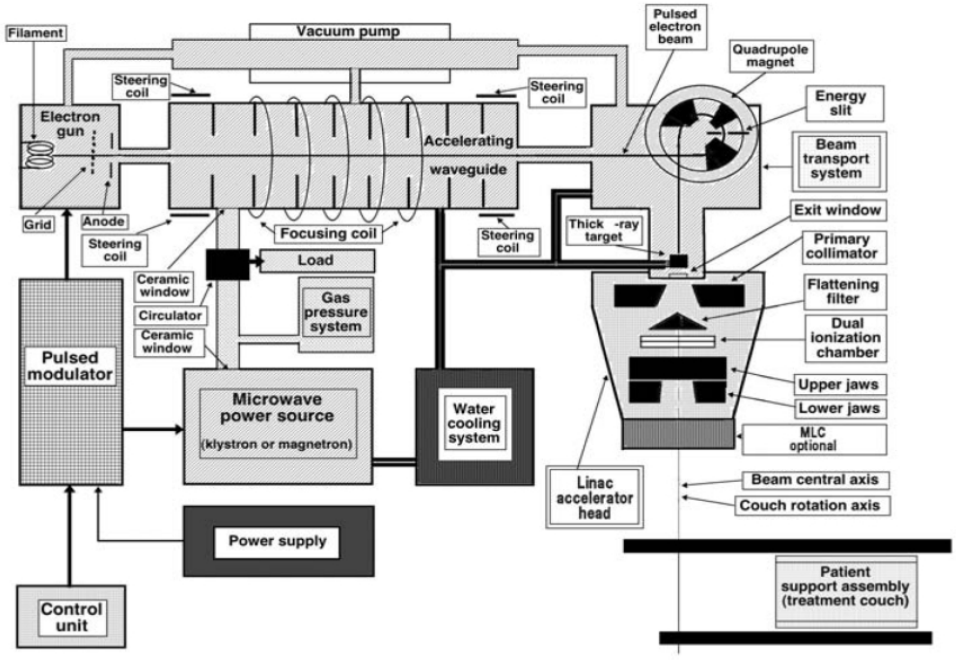

Figure 1.4 Block diagram of generic medical linear accelerator (reproduced from Podgorsak 2005).

distribution affording some sparing of the overlying tissue (skin). Conversely, the characteristics of clinical electron beams are advantageous in the treatment of superficial targets, especially when dose to underlying tissue is a concern. Figure 1.4 shows a block diagram of the various components of a modern accelerator which are required for the generation of a clinically useful treatment beam. While there are slightly different components available to perform many of these functions, this section will provide an overview of the components and methods relevant to the Oncor

(Siemens Oncology Care, Erlangen, Germany) medical linear accelerator, and specifically the production of a clinical electron beam, which was relevant to this thesis.

1.3.1 Electron Beam Generation

Electrons with initial energy of up to 15 kV are generated by thermionic emission in the electron gun and injected, in pulses, into an evacuated accelerating waveguide. In the waveguide, high power micro-waves (2998 MHz) generate radio-frequency (RF) fields which transfer energy to the electrons. The electrons are accelerated in linear trajectories through the same potential difference multiple times, in a cyclical manner. The high power RF fields used for acceleration are generated through the process of decelerating electrons in a evacuated device called magnetron or klystron. Due to thermal and other constraints, the RF power generator can not continuously provide the 2 – 6 MW (peak power) used for acceleration, as the cooling system would be unable to dissipate power losses. If the peak power is delivered at a low duty cycle (approximately 0.1%), acceptable mean power (~ 10^3 W) can be supplied to accelerate the electrons. The electron gun and RF source (a klystron in the case of a Siemens Oncor accelerator) are pulsed so that electrons are injected into the waveguide at the same time as it is energized by microwaves. This is performed by a device called the pulse modulator. Pulses typically have a duration of 4 μs and pulse repetition frequency of up to 220 Hz.

Linear accelerators use one of two types of accelerating waveguide: (i)

travelling wave structure or (ii) standing wave structure. The Siemens Oncor is a standing wave accelerator. In this type of accelerator, the waveguide is terminated at each end by a conducting disc. This causes microwave power to be reflected (with a phase change of π/2) and, as a result, standing waves build up in the accelerator structure. In standing wave type accelerators, every second cavity provides no energy increase to the electron. These cavities can therefore be moved out to the side of the waveguide, effectively reducing its length by 50%. In the waveguide, peak power is not established instantaneously as it takes the standing waves a finite amount of time (~ 1 μs) to reach maximum amplitude. During this time electron acceleration would not be efficient. This problem is addressed by using a triode type electron gun.

The triode gun contains a heated filament cathode, perforated anode and component called a grid. The electrons generated by thermionic emission in the cathode are focused into a pencil beam and accelerated by electrostatic fields supplied by the pulse modulator. Injection of electrons into the waveguide is controlled by the pulsed voltage applied to the grid. This is, in turn, synchronised with the pulses supplied to the microwave source. A delay in the injection of electrons accounts for the time required for the standing waves in the waveguide to reach maximum amplitude and ensures electrons are accelerated to the same energy. As a result of this delay, electron acceleration takes place during the final 3 μs of the typical 4 μs pulse only.

1.3.2 The Beam Transport System

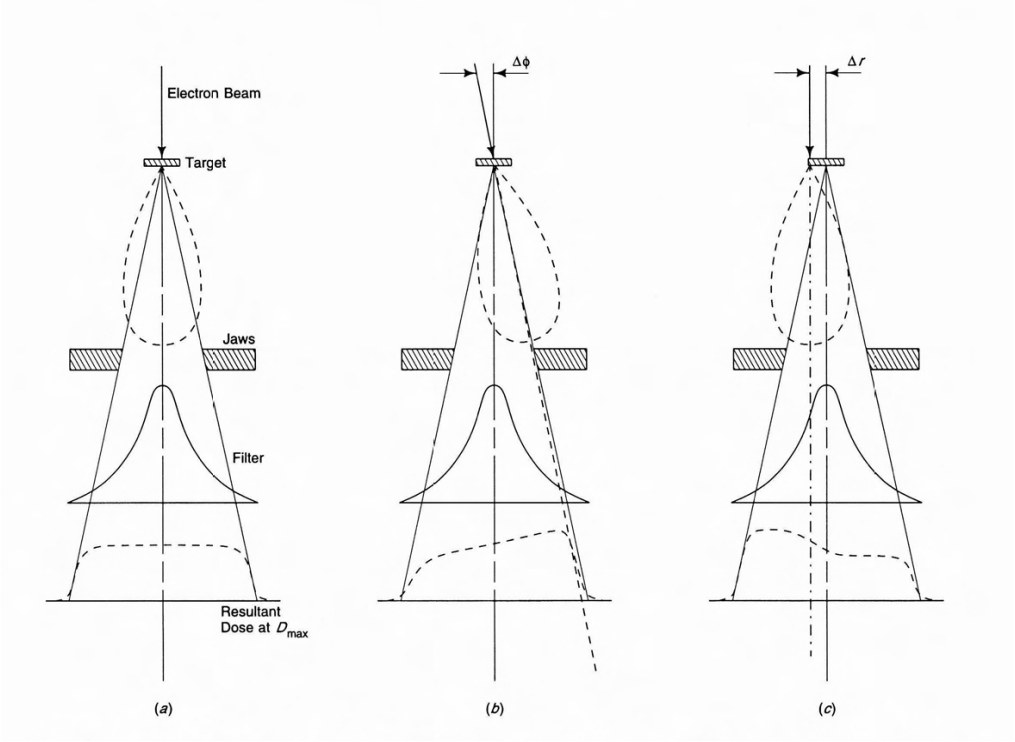

Figure 1.5 The effect of the (a) symmetric, (b) angled ($\Delta\phi$) and (c) displaced (Δr) electron beam incident on the x-ray target on the dose profile in water at the depth of maximum dose, D_{max} (reproduced from Karzmark 1993).

The electrons accelerated in the waveguide tends to diverge, partly due to Coulomb repulsion but mainly because the electric field has a radial component. The electron beam can also be displaced or obtain an angle relative to the waveguide axis. These effects could lead to very undesirable characteristics in the resulting treatment beam (figure 1.5). Divergence and displacement of electrons is therefore limited by using

magnetic fields to focus and steer the beam. The beam transport system is composed of three key components which control the path of the beam through the waveguide and into the treatment head: (i) the steering coils, (ii) the focusing coils and (iii) the bending magnet.

A magnetic field, *B*, normal to the direction of motion of an electron exerts a force which is perpendicular to both the direction of motion and the direction of the field. If the direction of motion is not normal to the magnetic field (i.e. has an angular component θ), then the force (*F*) on the charged particle is given by:

$$F = qVBsin\theta \tag{1.1}$$

where *q* is the charge of the particle (electron) and *V* is the speed of the particle.

Electrons travelling through the accelerator waveguide will not travel exactly along the central axis, in part due to engineering tolerances and mechanical misalignments and also due to the influence of external factors e.g. the earths magnetic field (~ 50 μT, for which the force (*F*) is clearly dependent on the waveguide orientation). Because of these effects, the electron beam has to be actively steered through the accelerating structure. This is performed by two orthogonal dipoles which, used in pairs, form the beam steering coils. One set of coils is positioned near the entrance to the waveguide (electron guide end) and can be used to correct for geometric misalignments in the gun. The second set of coils are located near the exit of the

waveguide (high energy end) and are used to correct for deflections caused by external magnetic fields and other influences and guide the beam onto the x-ray target (or electron scattering foil) via the bending magnet. The current in each set of steering coils can be preset to position the electron beam on the central axis, and in some cases, is dynamically adjusted via feedback signals from the monitor chamber in the treatment head (see below).

The electrons in the accelerator, under the influence of mutual repulsion and the small radial component of the microwave field, tend to diverge. It is therefore also necessary to "re-focus" the beam as it travels through the waveguide. This is accomplished by the use of a series of solenoids which are positioned outside the waveguide. The function of the focussing coils are two-fold; firstly they control the divergence of the electrons and stops the beam from hitting the walls of the waveguide; secondly they bring the electron beam (spot) to the required size (focus) at the end of the accelerator structure.

After the electron beam has been accelerated to the required energy it enters the treatment head where it is directed onto an x-ray target or electron scattering foil and further conditioned and collimated, making it suitable for patient treatments. In a modern accelerator the treatment head is usually mounted on a gantry which can be rotated around a fixed point in space called the isocentre. For high energy linear accelerators, straight-through mounting of the waveguide and treatment head would

lead to an unacceptable isocentre height. A bending magnet is therefore employed to transport the electron beam into the treatment head. While in practice it is more complex, the bending magnet can be thought of as a simple magnetic dipole. The coils of two electromagnets form the north and south poles. In a region of uniform field between the poles, an electron will follow a circular path of radius, *R*. From equation (1.1), the Lorentz force on a relativistic electron in a constant magnetic field is:

$$F = \frac{dp}{dt} = -ev \times B \tag{1.2}$$

where the momentum, $p = \gamma mv$, e is the electron charge, v is the velocity of the particle perpendicular to the field and γ is the Lorentz factor:

$$\gamma = \frac{1}{\sqrt{1-\beta^2}} \tag{1.3}$$

where $\beta = v/c$. In a static magnetic field, the rate of energy change of the electron is:

$$\frac{dE_e}{dt} = \frac{d}{dt}(\gamma mc^2) = 0 \tag{1.4}$$

$$\therefore \gamma = constant \tag{1.5}$$

The equation for the force on the electron (1.2) can therefore be written as:

$$\frac{dp}{dt} = \gamma m \frac{dv}{dt} = -ev \times B \tag{1.6}$$

For an electron travelling in a circular trajectory in the magnetic field the centripetal

acceleration, $a = -v^2/R$, and equation (1.6) becomes:

$$\gamma m(-\frac{v^2}{R}) = -ev \times B \tag{1.7}$$

Rearranging this, the radius of curvature of a relativistic electron in a static magnetic field is given by:

$$R = \frac{\gamma mv}{eB} \tag{1.8}$$

It can be seen from equation (1.8) that as a beam of electrons pass through a dipole magnet, the deflection (radius of curvature, R) is dependent on the electron energy. Low energy electrons will be deflected the most, with the more energetic electrons deflected less. A dipole magnet therefore acts as an energy spectrometer. The bending magnet in a linear accelerator is therefore also involved in selecting the energy of the treatment beam, as set by the current in the electromagnet coils.

Modern linear accelerators employ 270° bending magnet systems to achieve achromatic bending and focusing (Enge 1963). The various methods used are reviewed by Karzmark (1984). These systems are designed so that ideally all electrons traverse the exit window and hit the x-ray target or electron scattering foil at the same point, independent of kinetic energy. To accomplish achromatic bending, a 270° bending magnet incorporates a region where the pole gap is none uniform and the magnetic field (B) increases radially in the plane of the electron beam. An electron which enters

the bending magnetic will follow a curved trajectory dependent on its energy and the local magnetic field strength. Higher energy electrons will travel further into the magnetic field than those at lower energy (as they have a larger radius of curvature, *R*), however, at this point they will experience a stronger force from the magnetic field.

The Siemens Oncor accelerator utilises a bending magnet with locally tilted pole pieces to focus a range of entrant momenta, lateral displacements and divergences to be geometrically equivalent at the output and rotated by 270° (Oline et al. 1990). The system combines both uniform and non-uniform magnetic fields and was designed to bring the beam to a focus just beyond the exit window and at the x-ray target (or electron scattering foil). The entrance and exit pole faces are angled and have fringe fields which are used for radial and transverse focusing of the beam. In addition, the mid-magnet (at 135° of rotation) contains two angled poles which provide a radial field gradient. Higher momenta particles travel through a higher magnetic field while lower energy particles travel through a lower magnetic field. The angle of the poles is chosen so that electrons of different energy are re-converged at a single spot. In theory, the distribution of particles in the spot at the exit window will be the same as in the beam cross section that enters the magnet.

1.3.3 The Treatment Head

After transportation through the bending magnet, the electron beam emerges into the

treatment head through a thin low density exit window. The treatment head contains several components involved in the production, shaping (collimation) and monitoring of clinical x-ray or electron beams suitable for treating patients. The important components of current generation linear accelerator treatment heads include several retractable x-ray targets, flattening filters and primary electron scattering foils, a secondary electron scattering foil, primary and adjustable secondary collimators, dual transmission ionisation (monitor) chambers, a multi-leaf collimator and electron applicators.

Figure 1.6 shows a diagram of the treatment head of a Siemens Oncor accelerator configured for both clinical x-ray beam or clinical electron beam generation. In x-ray mode, the electron pencil beam emerging from the bending magnet is directed onto a high atomic number (Z) target. The emerging unfiltered beam gives a very sharply peaked dose distribution on the beam central axis. A flattening filter is therefore used to flatten the dose distribution by differentially absorbing the x-rays towards the centre of the beam. A tungsten primary collimator, conical in shape, is used to define the maximum available circular field size. A mirror is used to reflect a field light which illuminates an area representative of the radiation treatment field. Secondary collimation is provided by thick independently movable (asymmetric) rectangular tungsten jaws which can generate asymmetric square and rectangular fields. Modern accelerators also incorporates a multi-leaf collimator (MLC) which consist of

10 – 100s of independently driven tungsten leaves which can be used to generate complex treatment field shapes. Leaves are typically several centimeters thick to provide adequate attenuation of the primary beam and and narrow for sufficient spatial resolution in the direction normal to leaf motion (typically 1 cm at isocentre).

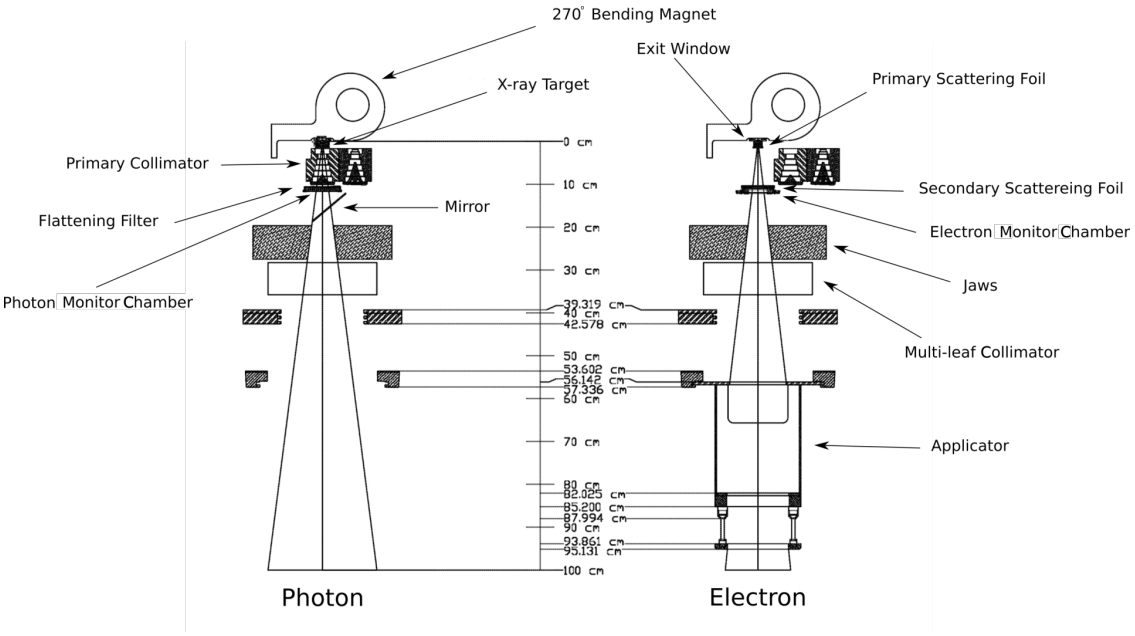

Figure 1.6 Treatment head of a Siemens Oncor linear accelerator showing the configuration for clinical x-ray (photon) and electron beams.

When the accelerator is operated in electron mode the x-ray target, flattening filter, x-ray monitor chamber and mirror are retracted from the beam path and replaced with a primary and seconday electron scattering foil combination and an electron monitor chamber. The primary scattering foil is used to widen the narrow (0.1 – 0.3 cm

diameter) pencil beam emerging from the exit window. Each discrete nominal kinetic energy electron beam requires its own scattering foil and each foil is chosen to give the best trade-off between scattering properties, energy loss and contaminant bremsstrahlung (x-ray) production.

The beam produced by the primary scattering foil has an approximate Gaussian profile, generally unsuitable for patient treatment. Modern accelerators therefore also utilise a secondary scattering foil. Each point irradiated by electrons scattered from the primary foil becomes a source of further scattered electrons and the overall effect is the creation of a much more uniform beam.

Electrons scatter significantly in the air between the scattering foils and patient surface. In order to generate a uniform dose distribution with sharp edges (penumbra), an electron applicator is typically used to collimate the beam at distances of 5 - 10 cm from the patient's skin. The applicator is attached to the treatment head and the x-ray jaws and MLC are usually set and interlocked to generate a field several centimeters larger than the field defined by the applicator. Optimal positioning of the secondary collimators leads to an improvement in electron beam uniformity and also reduces radiation leakage problems (Karzmark 1993). In earlier accelerators, electrons scattered from the walls of the electron applicator were also used to significantly improve the beam uniformity (Greene and Williams 1997). The use of dual scattering foils in modern accelerators, however, has meant that scatter from the applicator (which

primarily improved the dose distributions at shallow depth) is no longer need for this purpose and the applicator has been re-designed as a simple set of collimating diaphragms (or scrapers) which have a marginal effect on beam uniformity. In addition to the electron applicator, custom field shapes are often constructed from lead or lead-alloys and used to further conform the electron beam to the target volume (tumour).

Dual transmission ionisation chambers are used to monitor the x-ray or electron beam output (dose and dose rate) and the angular and positional distribution. The chamber is composed of electrodes divided into several sectors and is usually positioned below the flattening filter or secondary foil. It is designed to operate under saturation conditions and sealed so that response is independent of ambient temperature and pressure. The signal from the x-ray monitor chamber is used in a feedback circuit with the beam steering system. In this way, variation in the beam position due to, for example, the gantry (waveguide) rotation in earth's magnetic field, can be monitored and corrected (by adjusting the current in the beam steering coils). As well as monitoring output, the electron monitor chamber is primarily concerned with stabilising the dose rate. The dose rate signal from the monitor chamber can be used as a servo signal to the electron gun or for a triode gun, used to control the grid voltage and phase. In this way the required beam current can be maintained.

1.4 ELECTRON BEAMS IN RADIATION THERAPY

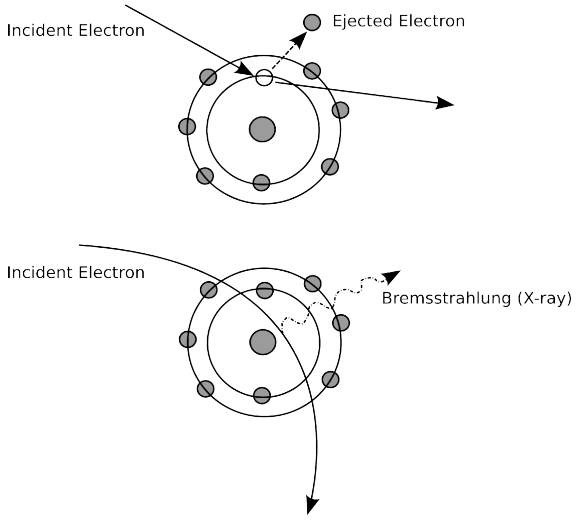

Figure 1.7 Inelastic interactions of an incident electron with an oxygen atom.

1.4.1 Electron Interactions

Electron interactions with matter (e.g. tissue or water) are the result of Coulomb forces between the electric field of the travelling particle and the electric field of orbital electrons and the nuclei of atoms. These collisions may be elastic or inelastic. In an elastic collision, the incident electron is deflected from its original path but there is negligible energy loss. The angular and spatial spread of pencil electron beam that undergoes multiple scattering in an absorber medium, can be approximated by a Gaussian distribution. The multiple scattering of an electron beam traversing a path length through an absorbing medium is usually described by the mean square of the

scattering angle θ which is proportional to the mass thickness of the medium. ICRU report 35 (1984) defines the mass scattering power *(T/ρ)* as:

$$\frac{T}{\rho} = \frac{1}{\rho}\frac{d\overline{\theta}^2}{dl} \qquad (\text{rad}^2 \cdot \text{cm}^2 / \text{g}) \qquad (1.9)$$

where *dl* is the pathlength and ρ is the density of the material. The scattering power varies approximately as the square of the atomic number of the absorbing medium and inversely as the square of the kinetic energy of the incident electron.

During an inelastic collision, in addition to a deflection of the incident electron from its orginal path, energy is also transferred to an orbital electron or emitted as bremsstrahlung (figure 1.7). In water and soft tissue, electron energy loss is mainly due to ionisation and excition resulting in deposition of energy or absorbed dose in the medium. If the ionisation process transfers sufficient energy to the orbital electron it creates an ionisation track of its own. This ejected electron is known as a secondary electron or δ-ray (delta ray). Because its mass is relatively small, an electron may also interact with the electric field of a nucleus. The subsequent rapid deceleration results in the electron losing part of its energy as bremsstrahlung (x-rays). For low atomic number material (e.g. soft tissue), electrons lose energy primarily through ionising events with atomic electrons. Bremsstrahlung production is of more importance at higher energy electrons and for higher atomic number materials (e.g. lead) as the rate of energy loss per unit path length increases with electron energy and the square of the atomic number

(Z^2) (Hendee et al. 2005). The angle at which x-ray emission intensity is maximum can be evaluated by:

$$\theta = arccos\left[\frac{1}{3\beta}\left(\sqrt{1+15\beta^2}-1\right)\right] \tag{1.10}$$

From this equation it is clear that in the diagnostic x-ray energy range (where $\beta \rightarrow 0$) bremsstrahlung are mainly emitted at 90° to the initial electron beam path. However, as the velocity of the particle increases ($\beta \rightarrow 1$), most x-ray photons are emitted in the direction that the electron beam hits the target material.

The inelastic energy losses by an electron travelling through a medium are expressed in terms of stopping power. The total mass stopping power represents the kinetic energy lost *dE* by collisions and emission of radiation over a path length *dl* in matter of density ρ:

$$\left(\frac{S}{\rho}\right)_{tot} = \frac{1}{\rho}\frac{dE}{dl} \qquad \text{(MeV·cm}^2\text{ / g)} \tag{1.11}$$

$(S/\rho)_{tot}$ is composed of two components: the mass collision stopping power $(S/\rho)_{col}$ which results from electron-orbital electron interactions and the mass radiative stopping power $(S/\rho)_{rad}$ which results from electron-nucleus interactions (ICRU 35 1984).

$$\left(\frac{S}{\rho}\right)_{tot} = \left(\frac{S}{\rho}\right)_{col} + \left(\frac{S}{\rho}\right)_{rad} \tag{1.12}$$

1.4.2 Measurement of Absorbed Dose

In conditions where (i) bremsstrahlung x-rays escape the volume of interest and (ii) secondary electrons are absorbed on the spot, the absorbed dose to the medium can be calculated using (Attix 1986):

$$D_{med} = \Phi_{med} \left(\frac{S_{col}}{\rho} \right)_{med} \tag{1.13}$$

where $(S_{col}/\rho)_{med}$ is the unrestricted mass collision stopping power of the medium at the energy of the electron and Φ_{med} is the electron fluence. Realistically, even for an initially monoenergetic starting electron kinetic energy, after traversing a medium the fluence spectum will range in energy from zero to maximum energy. The absorbed dose to the medium is therefore obtained from (Attix 1986):

$$D_{med} = \int_0^{E_{max}} \Phi_{med,E}(E) \left(\frac{S_{col}}{\rho} \right)_{med} (E) dE \tag{1.14}$$

where $\Phi_{med,\,E}$ denotes the primary fluence spectrum.

Electron interactions with an absorber medium result in the creation of energetic δ-rays which can carry energy away from the primary interaction site. If the total mass stopping power is used to estimate the absorbed dose in a given volume, then the absorbed dose will be overestimated due to the inclusion of these δ-rays. In radiation dosimetry the concept of restricted stopping power (S_Δ/ρ) is used to calculate the energy transferred to a region of interest. Restricted stopping powers account for the

component of the collision stopping power $(S/\rho)_{col}$ which includes all soft collisions plus hard collisions that result in creation of δ-rays with energies less that a cut-off value Δ. In this way, highly energetic secondary particles with energy above Δ are allowed to escape the region of interest.

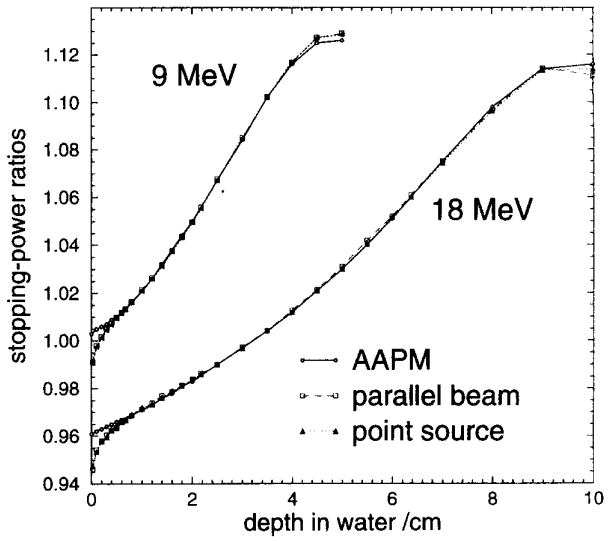

Figure 1.8 Spencer – Attix water to air stopping power ratios calculated by Monte Carlo code SPRRZ and compared with those used in previous AAPM dosimetry protocol (reproduced from Ding et al. 1995).

In radiation therapy the value of Δ is usually taken as 10 keV (Attix 1986). This energy is equivalent to the distance an electron may travel across the airgap of Farmer type or parallel-plate ionisation chamber. Spencer-Attix cavity theory relates the absorbed dose in the sensitive volume of the dosimeter medium (air) to the surrounding

medium containing the detector (e.g. water) (Burns et al. 1996). The Spencer-Attix relationship between dose to medium and the dose to the cavity is given by (Spencer and Attix 1955):

$$D_{med}/D_{cav} = s_{med,cav} \tag{1.15}$$

where $s_{med,cav}$ is the ratio of the mean restricted mass collisions stopping powers of the medium to that of the cavity. For real chambers, the presence of the ionisation chamber and cavity will affect the electron fluence spectrum and therefore additional corrections to Spencer-Attix theory are required. The absorbed dose to water for a parallel plate chamber, for example, is given by:

$$D_{med} = D_{gas}\, s_{med,gas}\, P_{wall}\, P_{repl} \tag{1.16}$$

where the wall correction factor, P_{wall}, accounts for the fact that chamber wall is a different material to that of the phantom and P_{repl} is composed of two components P_{gr} and P_{fl} which correct for (i) the changes in electron fluence spectrum and (ii) the upstream shift of the effective point of measurement of the ion chamber due to the presence of the cavity, respectively (Buckley and Rogers 2006). In addition to the role played in absolute measurements of absorbed dose, stopping power ratios are also important in performing accurate relative dose measurements where the energy of the secondary electrons change from one point in the medium to another. This is of particular relevance to measurement of electron beam relative dose where the restricted stopping power ratio is found to vary significantly with depth (figure 1.8).

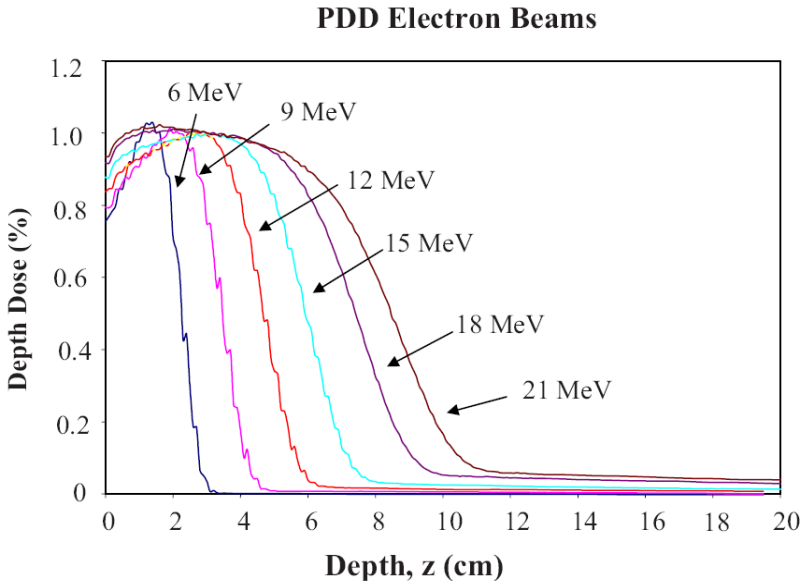

Figure 1.9 Effect of water ripple due to high scanning speed on low energy electron beam depth dose curves (reproduced from Das et al. (2008)).

Clinical electron beams are usually characterised by ionisation chamber dose measurements in a water phantom (tank). Measurement of the dose from electron beams can be divided into two categories: (1) absolute point dose measurements (Gy) and (2) relative dose distribution measurements (%). Measurement of absolute dose requires careful calibration of absorbed dose to water using a calibrated ionisation chamber in reference conditions and the relevant dosimetry protocol (e.g. Almond et al. 1999, Thwaites et al. 2003). Relative dose measurements include measurement of the variation of dose with depth in water on the central axis (depth dose curves, figure 1.9),

off-axis dose profiles and isodose curves and relative output factors. Guidelines on the measurement of relative dose are contained within AAPM task group reports 25 and 70, including discussion of the advantages and disadvantages of commonly used ionisation chamber and diode detectors (Khan et al. 1991, Gerbi et al. 2009). Das et al. (2008) have also published extensive recommendations on how to obtain accurate relative dose data and methods to reduce measurement errors (figure 1.9).

1.4.3 Characterisation of Clinical Electron Beams

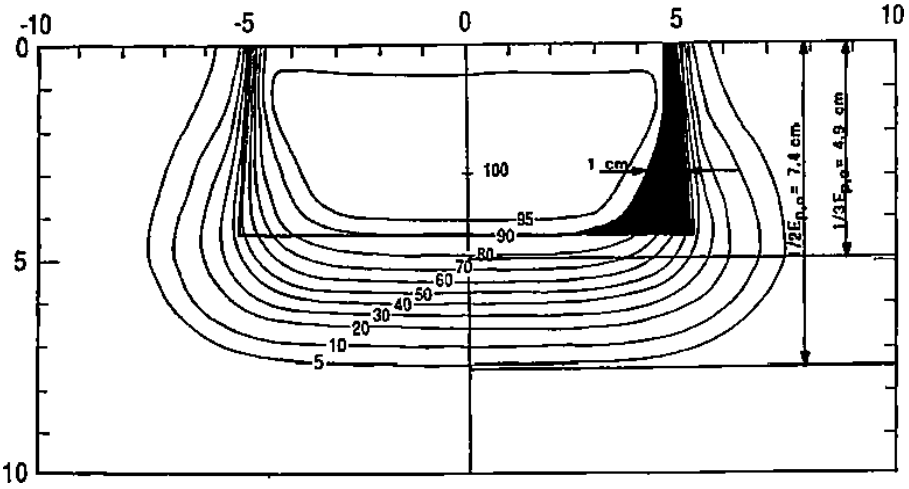

Figure 1.10 Plot of isodose curves in water for a 15 MeV electron beam and 10 × 10 cm² field size at 100 cm SSD. Lateral and distal dose fall-off determines the minimum margin between the target (tumour) and surrounding healty tissue and also the tumour and beam egde (reproduced from Hogstrom 1991).

Electron beams have been an important treatment modality in radiation therapy since

the 1950s. A single beam can deliver a relatively uniform 'plateau' of dose from 90% to 100% of maximum central-axis dose, with steep fall-off both laterally and distally (figure 1.10) (Hogstrom and Almond 2006). This has allowed superficial tumours (with distal margins < 6 cm from the patient skin) to be treated with minimal dose to underlying tissue and critical structures, generally not possible with x-ray beams. Electron beams in the 6 – 21 MeV energy range are mainly used in the treatment of (i) skin and lip cancers, (ii) chest-wall and neck cancers, (iii) shallow respiratory tract lesions and (iv) boost treatments of lymph nodes, surgical scars and residual tumour in surgical margins.

The electron beam which enters the treatment head has low spatial dispersion and a narrow energy spectrum. The electron envelope, or in some accelerator models, an energy slit is used to limit the electron beam energy spread to less than ±10% of the designated energy (Karzmark 1993, Oline et al. 1990) while spatial dispersions are controlled by the beam transport system. Scattering and energy loss interactions (section 1.4.1) with the various components of the treatment head lead to broadening of the energy spectrum and angular spread of the beam (figure 1.11). Radiative interactions also lead to the addition of a contaminant bremsstrahlung x-ray component. The beam at the patient surface contains both direct and indirect (scattered) components (Zhang et al. 1999). Electrons which experience at least one scattering event off field defining components (i.e. jaws, MLC, applicator or insert) belong to the

scattered component of

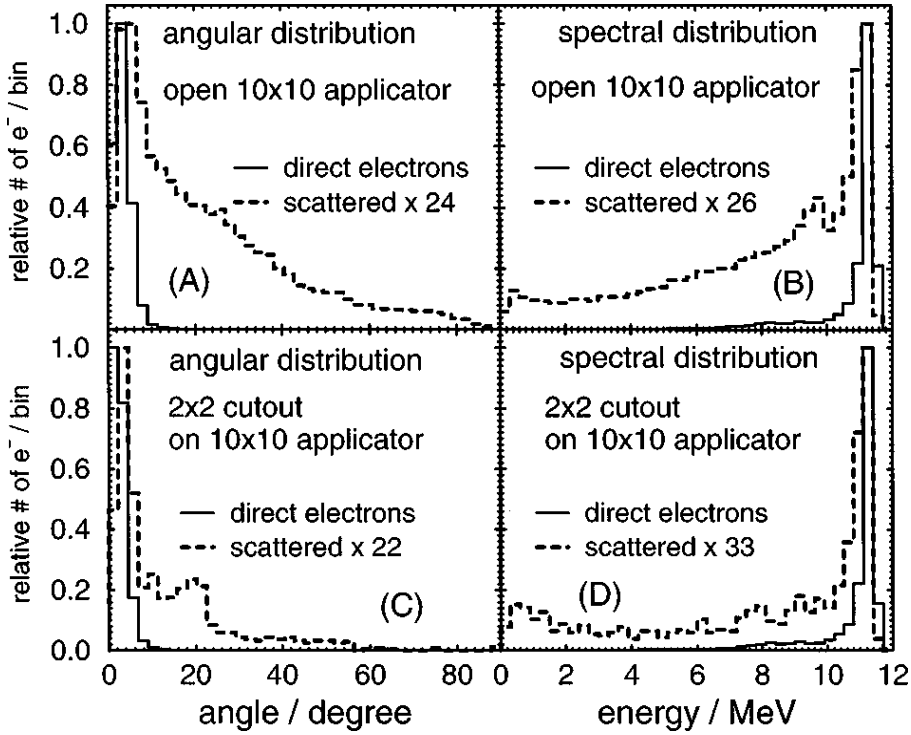

Figure 1.11 Monte Carlo calculated angular and spectral distributions inside a 11 MeV electron beam collimated with an open 10 × 10 cm² applicator (A and B) and a 2 × 2 cm² cutout (C and D). Most of the direct electrons are forward directed and have high energy. The scatter contribution (normalised to the peak of the direct component) has a much wider spectral and angular distribution. It can be seen that the cutout out preferentially allows through scattered electrons that are more forward peaked (reproduced from Zhang et al. 1999).

the beam, whereas, those which undergo multiple scattering in the exit window, scattering foils, monitor chamber or intervening air are catagorised as direct electrons. Dose deposition in the patient or water phantom is a complex function the treatment

head design, method of beam collimation and distance from the nominal source position to patient skin or water surface.

Percentage depth dose curves (PDD) for electron beams are characterised by relative uniformity within the first centimeters of tissue (or water), followed by a rapid fall-off of dose (figure 1.12). The build-up region (from the surface to R_{max}) results from scattering interactions between the electrons of the incident beam and atoms of the absorber, and also due to the liberation of secondary electrons. The surface dose increases with electron beam energy. At lower energies, the scattering power is much higher and electrons are scattered more easily and through larger angles. As a result, dose builds up over a shorter distance and the ratio of surface dose to maximum dose is lower. The range of the electron beam increases with increasing energy, with the mean energy at the phantom surface related to the depth of 50% of maximum dose, R_{50}, by:

$$\overline{E}_0 = C R_{50} \tag{1.17}$$

where the constant, C = 2.33 MeV cm^{-1} for water (Thwaites et al. 2003). Scattering and continous energy loss result in the sharp dose fall-off seen beyond the depth of maximum dose, R_{max}. For lower beam energies the gradient ($G = Rp / (Rp - Rq)$) of the dose fall-off is steeper because lower energy electrons are scattered at larger angles away from the central axis. Bremsstrahlung x-rays produced in the accelerator head, in air and in the irradiated medium lead to the tail in the depth dose curve beyond the maximum range of electrons. Bremsstrahlung contamination (D_x) increases with

increasing electron beam energy. To maximise sparing of distal healthy tissue while at the same time providing relatively homogeneous target coverage, electron treatments are usually prescribed to the depth of 80% of maximum dose, R_{80}. In this case, the depth R_{80} (cm) is defined as the therapeutic range. The electron beam energy is usually selected so that R_{80} coincides with the distal treatment margin.

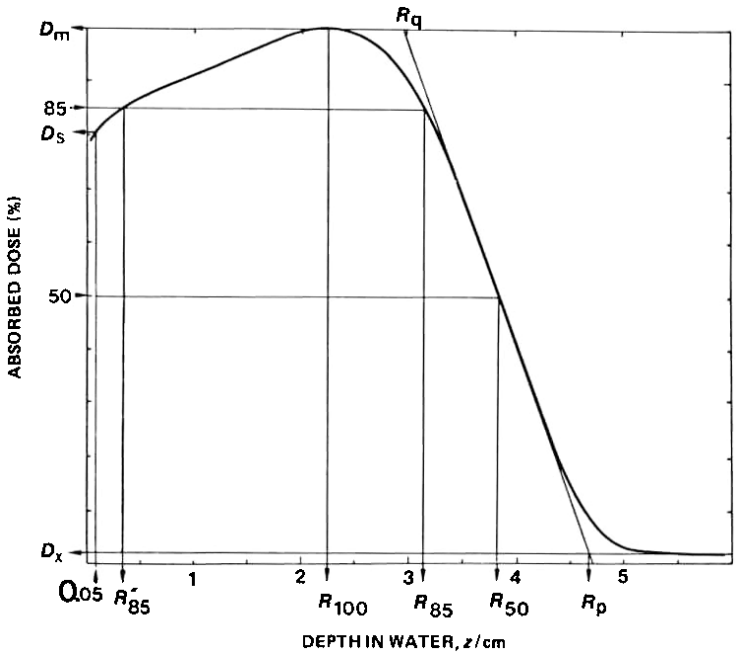

Figure 1.12 A typical percentage depth dose curve. The dose is normalised to 100% (D_{max}) at the depth of maximum dose, R_{max} (R_{100}). The depth of 50% dose, R_{50} is also shown. D_x represents the percentage dose from the contaminant x-ray component of the beam (reproduced from ICRU (1984)).

Figure 1.10 showed a typical isodose curves for an electron beam normally

incident on water at 100 cm source-to-surface (SSD). As the electron beam penetrates the medium it quickly expands below the surface due to scattering. There is bulging of the lower value (< 20%) isodose curves due to the increase in electron scattering angle with decreasing energy. For higher energy beams (> 15 MeV), there is considerable constriction of the higher value isodose curves (> 80%) as the depth increases to R_{80}. The field-size defined at the phantom surface will therefore have a smaller effective size across the 80% isodose curve. This must be taken into account in the treatment planning process.

Dose profiles, measured transverse to the beam direction, are also used for electron beam characterisation. They are particularly important for monitoring the beam uniformity. The dose profile is usually characterised by a relatively flat region of dose within the points of 80% of maximum dose on the central axis. The penumbra is defined as the region at the edge of radiation beam where the dose changes rapidly with distance from the central axis. At a given depth in the medium, the penumbra is a function of (i) geometric penumbra – due to electron source diameter and depth, (ii) transmission penumbra – due to transmission of radiation through the edge of the beam collimators and (iii) scattered radiation. In order to limit lateral irradiation of healthy tissue, it is usually desirable to have as narrow a penumbra as possible.

For an accelerator with applicators, measurement of electron beam output as a function of field size is required for each applicator and beam energy. The relative

output factor (*ROF)* for a given field size F at any source-to-surface distance SSD_F is defined as the ratio of dose D, on the central axis at the depth of maximum dose for that field, $R_{max}(F)$, to the dose for the reference field size F_0, (usually 10 × 10 cm^2 or 15 × 15 cm^2) and standard SSD_F0 (usually 100 cm) at the depth of maximum dose for the reference field used in absolute dose calibration, $R_{max}(F_0)$:

$$ROF = \frac{D(R_{max}(F), F, SSD_F)}{D(R_{max}(F_0), F_0, SSD_{F_0})} \tag{1.18}$$

Output factors for electron beams vary in a complicated manner with beam energy and field geometry (Kapur et al. 1998). They are known to depend in a fairly unpredictable way on the electron energy and the geometry of the jaws, applicator and final field-defining cut-out (Verhaegen et al. 2001).

1.4.4 Extended Source-to-surface Distance

Electron beam therapy is typically performed at a standard source-to-surface distance (SSD) where the beam data is measured. In certain circumstances, the physical size of the electron applicator and/or the patient surface contours preclude set-up at the standard SSD. This situation commonly occurs in the treatment of head and neck cancers. In addition, larger fields may be required for certain treatments and this can be achieved by using an extended SSD. For these situations, it is important to accurately determine the dosimetric effects of applying the treatment beam at extended distances.

Using an extended SSD causes a large change in (relative) output and some

alterations of the PDD (Saw et al. 1994). The PDD is modified over the entire range for small field sizes. For large field sizes, there are only small effects seen in the build-up region where relative dose is decreased (Cygler et al. 1997). The effects of extended SSD on the dose profile are represented by a loss of field flatness and an enlargement of the penumbra, particularly at lower beam energies (< 10 MeV) and for smaller field sizes (Das et al. 1995). The reduction in beam flatness can potentially lead to underdosage of lateral tissue.

Unlike an x-ray beam, an electron beam does not emanate from a physical source in the accelerator head (Khan 2003). The electron beam appears to diverge from a point known as the virtual source (Meyer et al. 1984). The inverse square law assumes we are dealing with a primary (direct) beam with no scatter (indirect) component and cannot be used for electron beams without making corrections. The virtual source can be determined as the point in space that appears as the point-source position for the electron beam. The effective point source (Khan 1984), based on the virtual source position, can be used to correct the output for non-standard SSDs when applying the inverse square law.

1.4.5 Field-size Dependence

The field size dependence of electron beam output and shape of the PDD is due to variations in scattered electrons and also occlusion of the primary beam. For field sizes

larger than the practical range (R_p) of the electron beam, the PDD is relatively unaffected by further increase in field size, since electrons from the field edges are not scattered sufficiently to contribute to the dose on the central axis. When the field size is reduced and the radius is comparable to the radius required for lateral scatter equilibrium, the output decreases, the PDD gradient (G) becomes less steep, surface dose increases and R_{max}, R_{80} and R_{50} shift towards the surface (Khan et al. 1991, Gerbi et al. 2009). The practical range R_p is unaffected by field size and depends only on electron beam energy.

Relative output factors vary in a complicated manner with field size (Khan et al. 1991). As outlined in section 1.4.3, the dose deposited at R_{max} depends on the number of electron tracks which come directly from the source (direct electrons) and those which are scattered from the secondary collimators and applicator (indirect or scattered electrons). Which component contributes most to the change in output with field size depends on the electron beam energy, secondary collimator setting and field size (applicator size). For output measurements it is important to firstly determine the depth of maximum dose which, for small fields, will occur at shallower depths than for the reference field size. In addition, stopping power ratios decrease when the field size is less than 3×3 cm^2 and, ignoring the change in stopping power ratio due to the change in R_{max} as the field gets smaller, could lead to a significant overestimation of output factors (Zhang et al. 1998).

1.4.6 Conformal Therapy

Conformal electron therapy uses modulation of energy, intensity and/or beam angle to conform (shape) a homogeneous, or prescribed heterogeneous, dose distribution to a superficial target volume and deliver minimal dose to underlying critical structures and healthy tissue (Hogtrom et al. 2003). Modulated electron therapy can be achieved using (i) bolus (a waxy tissue equivalent material), (ii) segmented fields (Zackrisson and Karlsson 1996) and/or (iii) intensity modulation (Ma et al. 2003). Energy modulation can be performed in continuous steps using bolus or discrete steps of about 3 MeV on current accelerators. Intensity modulation uses multiple electron fields, each with a different energy and intensity to conform the therapeutic dose to the target. On current accelerators, intensity modulation can be performed using a multi-leaf collimator (MLC) or in a rather impractical way, using multiple applicator inserts (cutouts).

Bolus conformal electron therapy (BCET) uses a single electron beam energy with a variable thickness bolus to conform the therapeutic depth (usually R_{90} or R_{80}) to the distal extent of the target and deliver minimal dose to surrounding normal tissue. BCET has found application in treatment of the head and neck (Kudchadker et al. 2002) and postmastectomy chest wall (Perkins et al. 2001, cf. figure 1.13). Segmented field conformal electron therapy (SCET) uses multiple electron fields, each sharing the same virtual source position, but having their own discrete energy and beam weighting, to achieve the same dose delivery objectives as BCET. SCET can be delivered using

multiple cutouts (Vatanen et al. 2009) or a MLC (Klein et al. 1998). Some of the advantages of BCET over SCET include (1) finer control of the therapeutic depth because it does not rely on the discrete energies of the accelerator, (2) increased dose homogeneity due to lack of field abutment and (3) less bremsstrahlung dose because of the use of a single field (Hogstrom et al. 2003). However, SCET may be advantageous when sharper distal dose fall-off is required as lower beam energies can be selected when the target is at shallower depths. In addition, if a MLC is used to shape the field, then there are no further patient set-up requirements.

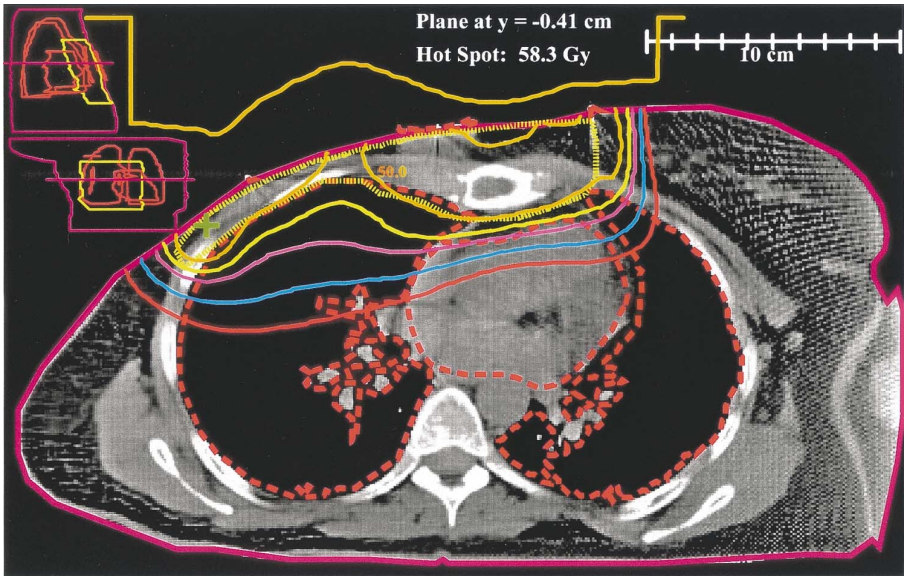

Figure 1.13 Conformal irradiation of postmastectomy chest wall using a 16 MeV electron beam and custom 3D electron bolus to modulate the beam penetration across the treatment field (reproduced from Perkins et al. 2001).

1.5 MONTE CARLO SIMULATION IN RADIATION THERAPY

The complex nature of electron-tissue interactions means that electron beams are generally difficult to model. Electrons can create bremsstrahlung photons and secondary electrons (δ-rays) and, in addition, they scatter significantly in a medium. In electron beam therapy, calculation of collimator scatter and leakage and the prediction of dose in small fields, situations involving sudden changes in surface contours, small inhomogeneities and oblique beam incidences are particularly challenging. Analytical radiation transport, based on work by Eyges (1948) and Brahme (1975), has perhaps had the most impact on electron beam transport calculations to date (e.g. Hogstrom et al. 1981). However, measurements have shown that dose calculations based on Fermi-Eyges theory exhibit significant discrepancies, of 10 – 20% or more, in some situations (Ostwald et al. 1994, Faddegon et al. 1998) and while there has been some work to improve these dose calculation algorithms (Shiu and Hogstrom 1991), large discrepancies (20%) remain in some situations (Boyd et al. 2001).

Monte Carlo simulation is considered to be the most accurate method of electron dose calculation and is now having an increasing influence in electron beam therapy (Ma and Jiang 1999, Chetty et al. 2007). Monte Carlo simulation can provide a wide range of accurate data, including data which is difficult or impossible to measure (Rogers 2006). Some of the early uses of the Monte Carlo method included calculation

of mass stopping power ratios and the relationship between mean energy at the phantom surface and the practical range of the electron beam as recommended for electron beam dosimetry by ICRU Report 35 (Berger and Seltzer 1969, ICRU 1984). Monte Carlo has the potential to solve many of the electron transport problems, particularly in patient heterogeneities, encountered with conventional treatment planning algorithms (Reynaert et al. 2007). The main drawback of Monte Carlo simulation as applied to radiation transport has been long calculation times. However, the development of faster codes, optimised for radiation therapy applications, and improvements in processor speeds, have significantly reduced calculation times. Today all codes of practice for absolute dose calibration use Monte Carlo derived water-to-air stopping power ratios, $s_{water,air}$ (Almond et al. 1999, Thwaites et al. 2003) and additionally, a number of commercial vendors have begun to adopt Monte Carlo algorithms for electron treatment planning (Neuenschwander et al. 1995, Kawrakow 2001).

1.5.1 The Monte Carlo Method

The Monte Carlo method, as applied to radiation transport problems, uses random numbers to sample the probability distributions of various quantities in order to simulate the random trajectories, interactions and energy deposition of individual particles in matter. The term “Monte Carlo” was coined by Metropolis, von Neumann and Ulam while using random sampling methods to investigate nuclear weapons

technology during the Manhattan project at the end of WWII (Metropolis and Ulam 1949, Metropolis 1987). This was also the first use of the method in radiation transport problems. Section 1.5.2 provide details on the Monte Carlo simulation of electron and photon transport. What follows is a basic overview of a Monte Carlo simulation as applied to a generic problem in radiation therapy.

The Monte Carlo code starts by reading in user specified information. This includes the desired source (energy, particle type, direction and angle), geometry (e.g. a detector model), transport parameters (e.g. low energy cut-off below which a particle track is terminated), tally or score specifications (e.g. fluence or dose in an arbitrary region) and number of histories (i.e. the number of initial particles to simulate). A pseudorandom number generator ("pseudo" since it is not possible for a computer program to generate a completely random number) is used to create a particle. During its lifetime, the particle's interactions may result in the creation of secondary particles. Each particle (history) is transported based on physics interaction probabilities (cross-sections) and tracked until it reaches the specified energy limit (cut-off) or a discard boundary. At this point a new random number is used to generate the next particle history to be transported through the geometry.

Each history is an independent sample which contributes to a tally and therefore the accuracy of the result will depend on the number of histories simulated. When calculating a quantity of interest (tally) in a Monte Carlo radiation transport simulation

(e.g. fluence or dose) there is a statistical uncertainty associated with that quantity. The number of histories is therefore usually decided on by the user based on the statistical uncertainty requirements. The statistical uncertainty, or variance, for the tally can be calculated on a history-by-history basis using (Walters et al. 2002):

$$s^2 = \frac{1}{N-1}\left(\frac{\sum_{i=1}^{N} X_i^2}{N} - (\frac{\sum_{i=1}^{N} X_i}{N})^2\right) \tag{1.19}$$

where s^2 is the variance, N is the number of independent events (histories) and X_i is the quantity scored e.g. dose.

The statistical uncertainty is proportional to the inverse square root of the number of histories. Therefore, to reduce the uncertainty by half it is necessary to run four times as many histories. Once the number of histories simulated is large enough, quantitative information can be extracted by averaging over all the histories.

1.5.2 Coupled Electron and Photon Transport

In the external beam therapy (megavoltage) energy range, photons interact with matter by four main processes (listed in order of importance): (i) Compton scattering with atomic electrons, (ii) pair production in the nuclear or electrons electromagnetic fields, (iii) photo-electric absorption and (iv) Rayleigh scattering. The first three processes result in a transfer of energy from the incident photon to electrons or positrons. In most cases, Compton scattering is the dominant process, however, pair production becomes

increasingly important at higher energies and, in particularly, in higher Z materials (e.g. the tungsten secondary collimators of an accelerator treatment head). Electron interactions with matter have been discussed in section 1.4.1, including the two main energy loss processes: inelastic collisions with orbital electrons and radiative losses. Radiative energy losses (bremsstrahlung) transfer energy back to photons and this leads to the “coupling” of electron and photon transport in the medium.

The Monte Carlo method attempts to solve the Boltzmann transport equation which is applied to particle transport in a material. Analogue Monte Carlo simulation can provide an exact solution to particle transport problems for any energy range and geometry and material composition. In an analogue simulation all particle (including secondary particle) interactions are simulated explicitly, until the particle's energy drops below a user-defined cut-off. Analogue Monte Carlo simulation is the conventional method used for the transport of neutral particles (photons). The typical steps in an analogue transport are as follows:

(1) Select the distance to the next interaction

(2) Transport the particle through the geometry to the interaction site

(3) Select the interaction type

(4) Simulate the interaction

Analogue simulation of charged particle transport is impractical due to the very

large number of interactions a charged particle undergoes before its energy drops below a pre-determined cut-off. For example, electrons typically undergo 7000 elastic interactions while slowing down from 0.5 MeV to 0.25 MeV in gold (Berger and Wang 1988). To resolve this issue, the culmulative effects of a number of interactions are approximated by a single simulation step. This approximation method, reviewed by Nahum (1999), is known as the “condensed history” approach and is used in all general purpose Monte Carlo codes for charged particle transport.

The condensed history technique was first described by Berger (1963) and is based on the fact that the majority of electron interactions lead to only small changes in the electrons energy and direction. Berger defined two classes of condensed history algorithm. In class I algorithms all particles are subject to grouping, using continuous energy loss models - to describe energy loss, and multiple-scattering theory - to describe angular deflections. In a class II scheme, however, events above a specified threshold, or cut-off energy, are simulated explicity i.e. in an analogue manner (also known as “hard” collisions), while, only events below this cut-off energy are grouped together, using restricted stopping powers (known as “soft” collisions). As with analogue transport, class II condensed history methods also use a transport energy cut-off and this cut-off is often set to the same value as the threshold separating “hard” and “soft” collisions. Below the cut-off for “hard” collisions, a method is needed to decide when an electron undergoes its next 'multiple scattering' event. Most general purpose

codes address this issue by using a constant continuous energy loss over the step.

The condensed history method introduces step-size as an artificial parameter and if too large a step size is selected, artefacts may be introduced into calculated results (Bielajew and Rogers 1988). An important example of this is in the simulation of ionisation chambers where the sensitive volume has a low density and therefore accurate modelling requires that the step size be made extremely short in the wall and gas volume of the chamber (Nahum 1999). This issue can also be resolved by resorting to single scattering (i.e. analogue) simulation when in the vicinity of the boundary between two regions (which is the method employed by EGSnrc (section 1.5.3)).

In concluding this section it is important to highlight that the accuracy of the result (or tally) provided by a class II condensed history electron transport algorithm is highly dependent on appropriate selection of a number of parameters. These parameters usually include (using EGSnrc (section 1.5.3) notation): *ECUT* - the energy below which an electron history is terminated; *ESTEPE* - the maximum fractional energy loss per electron step; *AE* - the energy below which secondary electron losses are treated as continuous; *SMAX* - the maximum electron step length. It is important for the user to ensure that the desired result e.g. dose to a specified volume, spectral or angular distribution, is largely independent of the values of all these parameters.

1.5.3 EGSnrc and User-codes: BEAMnrc, DOSXYZnrc and MCRTP

A number of accurate Monte Carlo simulation packages have been developed which can be used for coupled electron-photon transport in radiation therapy. Some of these codes are discussed by Rogers (2006) and Chetty et al. (2007). The EGSnrc code was selected for use in this thesis because of its accurate electron transport simulation (Kawrakow 2000), relevance to radiation therapy applications and widespread use. EGSnrc comes with a number of user codes for calculating quantities of interest for ionisation chambers, detector response and energy deposition in XYZ and RZ geometries. Additionally, the EGSnrc user codes BEAMnrc (Rogers et al. 2009, originally BEAM (Rogers et al. 1995)), DOSXYZnrc (Walters et al. 2011, originally DOSXYZ (Rogers and Bielajew 1990)) and MCRTP (Faddegon et al. 1998) have been developed specifically for modelling of medical accelerator treatment heads and calculation of dose in phantom or patient models.

The EGSnrc code allows Monte Carlo simulation of coupled electron and photon transport through arbitrary geometry for particles in the dynamic energy range of 1 keV to ~ 10 GeV. In addition to the four main photon interactions outlined in section 1.5.2, EGSnrc also simulates the following electron interactions: (i) bremsstrahlung, (ii) inelastic collisions with atomic electrons and (iii) elastic collisions with nuclei and atomic electrons. EGSnrc is based largely on the EGS4 Monte Carlo code (Nelson et al. 1985) but includes many improvements in electron transport

(Kawrakow 2000). A full description of the EGSnrc code is provide by Kawrakow et al. (2011) including details on simulation of photon and electron interactions, electron step and boundary crossing algorithms and methods of variance reduction.

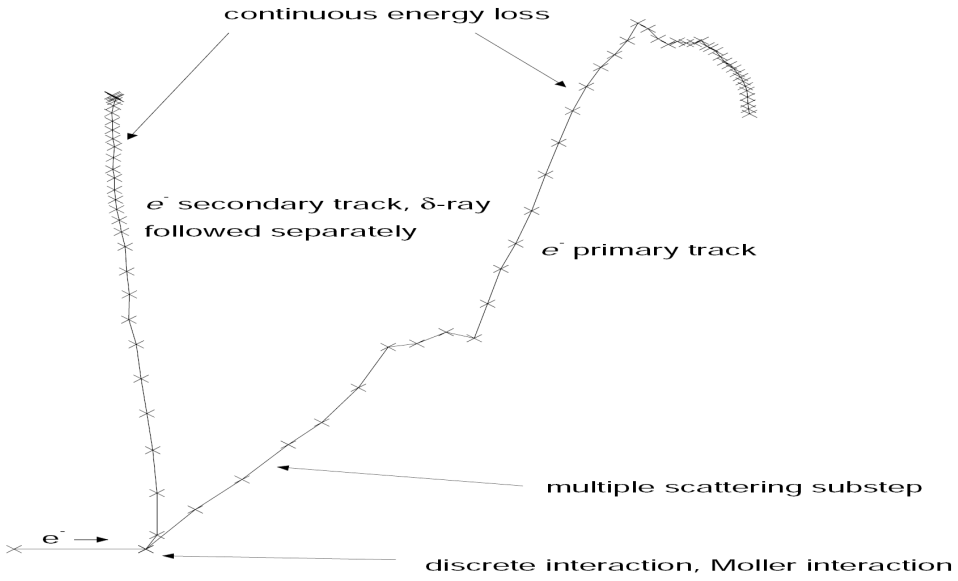

Figure 1.14 A typical electron transport simulated in EGSnrc (Kawrakow et al. 2011).

Electron transport in EGSnrc employs the class II condensed history method (Berger 1963). Figure 1.14 shows a graphic of a typical electron transport. "Hard" interactions (section 1.5.2) above a user specified cut-off are simulated discretely using the "event-by-event" model (including the creation of bremsstrahlung photons and secondary electrons), while interactions below the cut-off energy are approximated by continual energy loss using restricted stopping powers. Discrete electron-electron inelastic interactions utilise Møller cross sections (ICRU report 37 1984) for collisions

that result in the creation of secondary particles with energies greater than the user specified threshold.

Multiple scattering theory is used to simulate the effects of the large number of elastic interactions which occur below the specified cut-off energy. Electron multiple scattering in EGS4 was based on the multiple scattering theory of Moliere (Bethe 1953). This implementation of multiple scattering has been shown to lead to significant errors, of up to 6% in some situations (Ross et al. 2008). Kawrakow and Bielajew (1998) developed a more accurate model of multiple scattering based on the work of Goudsmit and Saunderson (1940) and this was implemented in the EGSnrc code (Kawrakow 2000). Investigations have found that the multiple scattering implemented in EGSnrc appears to 'slightly' under-estimate scatter (compared to measurements) from various foils (including Al, Ti and Au foils - of relevance to treatment head simulation) placed in the beamline of a highly constrained research linear accelerator operating at 13 MeV and 20 MeV (Ross et al. 2008, Faddegon et al. 2009). However, the differences between measured and simulated characteristic (scattering) angles were generally within 1.5%, with a maximum difference of 4%.

The accuracy of the EGSnrc code has been further validated with a thick-target bremsstrahlung experimental benchmark (Faddegon et al. 2008). That study demonstrated that the code is capable of an accuracy of 5% in photon yield for 10 – 30 MV beams incident on thick Be, Al and Pb targets. Based on these benchmarks it can

be concluded that the electron and photon fluence calculated with EGSnrc is approaching the accuracy needed for accurate simulation of radiation therapy beams (Faddegon et al. 2009).

1.5.4 Monte Carlo Accelerator Treatment Head and Patient Simulation

A full simulation of the electron treatment head using Monte Carlo methods can potentially provide the accurate beam data (fluence) required for electron beam treatment planning (Ma and Jiang 1999). Extending the Monte Carlo simulation (of coupled electron-photon transport) through the patient specific collimators and compensators, and into a model of the actual patient geometry (and scoring the absorbed dose), can resolve many of the problems encountered with analytical dose calculation algorithms (Faddegon et al. 1998, Rogers et al. 2005, Reynaert et al. 2007, Chetty et al. 2007). Faddegon et al. (1998) have discussed the realistic accuracy goals of Monte Carlo-based treatment planning for electron beam therapy. Table 1.1 summarises some of the uncertainties associated with electron dose delivery (for both Fermi-Eyges-based or Monte Carlo-based dose calculation). Based on this data, a realistic goal for uncertainty in dose delivery would be 5% in absolute dose, normalised to a given maximum, or 0.5 cm in the position of the isodose line (or 5% / 0.5 cm). This overall accuracy in absolute dose can be achieved if dose to water, relative to reference conditions, is calculated to an accuracy of 2% / 0.2 cm (Faddegon et al. 1998).

Table 1.1 Summary of some of the uncertainties in electron dose delivery, excluding patient set-up uncertainties (reproduced from Faddegon et al. 1998).

Source of Uncertainty	Conventional	Monte Carlo
Output / Energy calibration	2% / 0.2 cm	~
Drift in Calibration	2% / 0.2 cm	~
ROF, incl. Extended SSD	4%	2%
90% isodose, incl. Extended SSD	0.4 cm	0.2 cm
Field Flatness	5%	2%
Surface Contour	2% / 0.2 cm	2% / 0.2 cm
Inhomogeneities	10% / 1.0 cm	2% / 0.2 cm
Overall Estimate	10% / 1.0 cm	5% / 0.5 cm

A Monte Carlo-based dose calculation (treatment plan) which involves full treatment head simulation is usually broken up into 2-3 steps. During the first step particles are transported through the patient independent, or fixed, components of the treatment head and a phase-space file is generated. This phase-space file contains phase-space information on all particles that cross a user specified scoring plane. The phase-space information includes the energy, position, direction, charge and may also include details on particle's interaction history. The advantage of this techniques is that this part of the calculation can be reused as necessary (as it is independent of the patient). In the next step particles are transported through the patient specific collimators and either stored in another phase-space file or transported through the patient model in the same simulation.

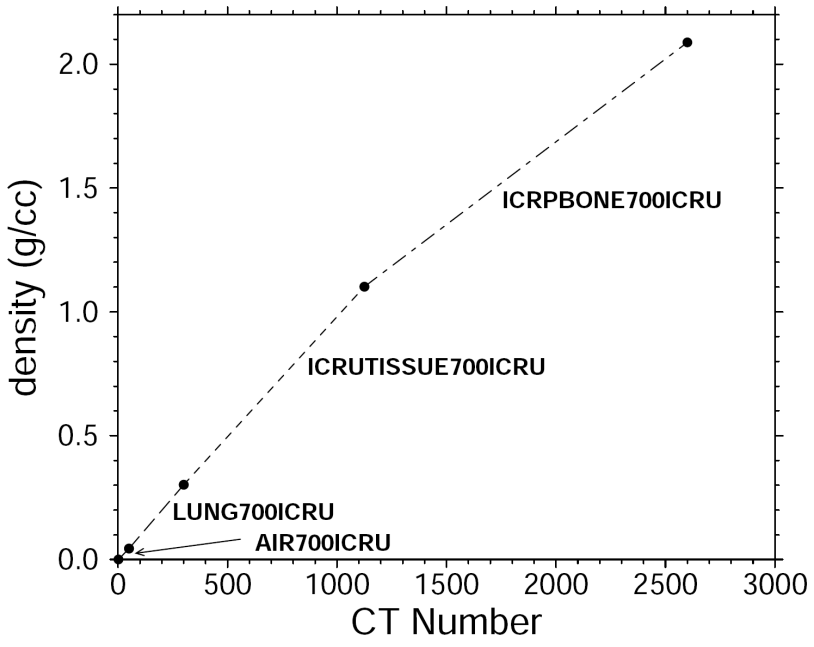

Figure 1.15 CT number to material and density conversion ramp (reproduced from Kawrakow et al. 1996).

Simulation of the treatment head of linear accelerators using a detailed descriptions of the geometry has become an important aspect of radiation therapy. The accuracy of the model is usually assessed by comparison of (water phantom) measured and Monte Carlo calculated output factors and dose distributions. Monte Carlo treatment head simulation has few free parameters, making calculations highly sensitive to errors in the beam characterisation. For this reason it is important to be aware of the sensitivity of Monte Carlo simulation results to details of the initial electron beam (source) and geometry of the treatment head (and also the necessity for accurate

measured data). For example, the electron beam range (R_{50}) in water is highly sensitive to the initial electron energy (0.1 cm change per 0.2 MeV) and the source energy is therefore the primary tuning parameter in electron beam simulations. However, electron beams are also very sensitive to all components in the beam path and therefore accurate geometric descriptions of all treatment head components is required (Chetty et al. 2007).

Once the accuracy of the fluence from the treatment head model has been validated, Monte Carlo simulation can be used to transport the particles through a patient model and calculate the absorbed dose. In radiation therapy planning, patient anatomical information is represented by a CT dataset. CT numbers are expressed in Hounsfield Units (HU), which are related to the linear attenuation coefficient, μ:

$$HU = 1000\left(\frac{\mu}{\mu_w} - 1\right) \tag{1.20}$$

where μ_w is the linear attenuation coefficient in water. This results in a HU value of -1000 for vacuum and 0 for water.

Conversely, Monte Carlo algorithms use actual material density and atomic composition when performing particle transport. It is therefore neccesary to convert CT HU values into material and density values. While it is not possible to determine materials directly from HU, it is possible to perform an estimate. Material compositions can be indirectly approximated by estimating the mass density from the electron density

and assigning a material according to this (du Plessis et al. 1998, Siebers et al. 2000). Figure 1.15 shows the default CT ramp used by the EGSnrc user-code DOSXYZnrc to convert from HU to material and density. In this case four distinct materials are used to describe all possible tissue types.

Once a Monte Carlo calculated dose distribution has been obtained, it is important to be aware of the statistical uncertainty and resolution of calculated dose (Chetty et al. 2007). Monte Carlo simulation invariably involves the calculation of dose in a volume of interest or voxel and the statistical uncertainty in the dose is affected by the size of a voxel. For a large volex, there tends to be an increase in dose deposition and therefore the uncertainty is smaller. When choosing the voxel size, it is important to choose the size appropriately. For example, in the calculation of transverse dose profiles it is important to choose the voxel size such that it does not average the dose in the penumbral region. Additionally, in Monte Carlo treatment planning, it has been shown that using too large a voxel size can cause details to be missed due to incorrect material and density assignment (Cygler et al. 2004).

1.6 THESIS OBJECTIVES

Conventional treatment planning systems cannot accurately model electron beams. This has meant that some treatment techniques are not utilised (e.g. skin collimation and variable thickness bolus), new technologies have seen slow implementation (e.g.

modulated electron beams) and electron beam therapy, as a whole, is under-utilised. Monte Carlo simulation is known to be very accurate when used accurately for treatment planning, accounting accurately for collimator scatter, airgap and tissue heterogeneities (Ma and Jiang 1999, Chetty et al. 2007).

This study investigated the simulation of clinical electron treatment heads using Monte Carlo methods. Accurate implementation of Monte Carlo patient dose calculations requires knowledge of the radiation beam from the accelerator. A detailed simulation of the treatment head can provide accurate details of the beam incident on the patient needed for complex planning. Additionally, the treatment head model can improve understanding of clinical beam characteristics, aid accelerator and beam model design and improve the accuracy of clinical dosimetry by provision of more realistic fluence data.

The EGSnrc/BEAMnrc Monte Carlo simulation code was used to model the electron treatment head of a Siemens Oncor medical accelerator. As a starting point, the treatment head was modelled using electron source and geometry specifications provided by the accelerator manufacturer. Invariably, during the accelerator commisioning process the beam energy and in some cases treatment head geometry (e.g. secondary scattering foil lateral position) is altered from specification. Therefore the source and geometry in the Monte Carlo model required adjustment to match measured applicator-defined field dose distributions. With a calibrated treatment head

model some of the characteristics of electron beams at non-standard treatment distances were investigated.

There are known limitations to modelling the electron treatment head using the above approach (Faddegon et al. 2005). Therefore, this study also investigated the accuracy of treatment head models developed with electron source and treatment head geometry details based on measurement of non-conventional large electron field dose distributions. With measured (relative) dose distributions normalised to 100% on the central axis, the accuracy of dose calculated by this method is capable of approaching 2% difference in dose, 0.2 cm in the field edge of the dose profile or 0.1 cm in the depth penetration (R_{50}). These values were taken as the accuracy goals in this work.

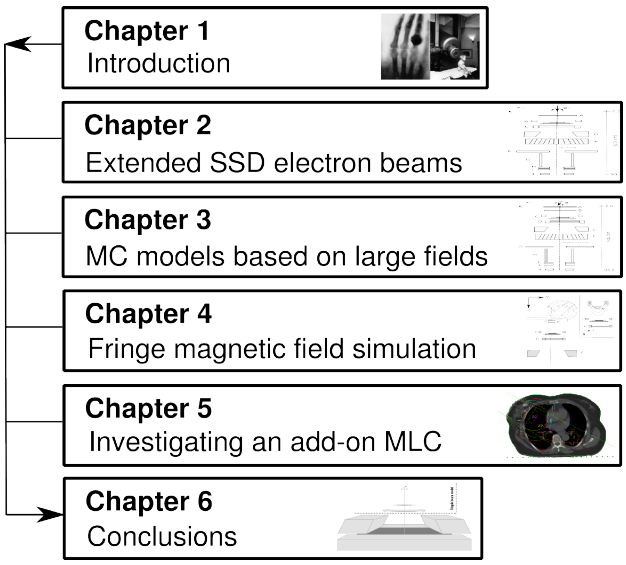

Figure 1.16 Overview of thesis structure and contents.

Finally, the accurate treatment head models developed were used to compare a conventional and a novel electron beam collimation and dose delivery technique. This included the use of Monte Carlo simulation to model a patient treatment plan.

A flow diagram of the thesis structure is shown in figure 1.16.

2. Monte Carlo Simulation of Electron Beams at Extended Source-to-surface Distances

2.1 INTRODUCTION

Electron-beam therapy is usually performed at the standard source-to-surface distance (SSD) of 100 cm. At this distance, the characteristics of the radiation beam such as percentage depth dose, off-axis profiles, and output factors are known. In certain situations, anatomic constraints may dictate the use of an extended SSD (for example, 110 cm SSD). In the treatment of the lateral neck region, for instance, a patient's shoulder may obstruct the positioning of the electron applicator. At extended SSD, the output and dose profile characteristics of the radiation beam are altered, leading to uncertainty in treatment. The effects of non-standard SSD on machine output and dose distributions must be assessed to ensure accurate patient treatment (Khan et al. 1991).

The main effects of extended SSD on clinical electron-beam characteristics have been outlined by Cygler et al. (1997) and Khan (2003). These changes to the radiation beam characteristics are mainly a result of the variations in scattered electron tracks at various levels. Monte Carlo simulation methods can be used to extract detailed

information on particle history and investigate how the electron scattering from the various components of the linear accelerator treatment head affect dose distributions and beam output.

Electron-beam output does not follow the inverse square law (ISL) as photon beam output does. Two methods of output correction are typically used, namely, the effective SSD method (Khan 1984) and the virtual SSD method (Meyer et al. 1984). The dose deposited at the depth of maximum dose, R_{max} depends on the number of electron tracks traversing the measuring volume. As discussed in section 1.4, some electrons come directly from the source, traversing the scattering foils and dose chambers, scattering only in the intervening air (the direct component of the beam). The remainder are scattered by the jaws, the multi-leaf collimator, and the scrapers of the electron applicator (the indirect or scatter component of the beam).

This chapter details the modelling of a Siemens Oncor accelerator (electron) treatment head for standard applicator defined fields. This included the validation of the model against measured dose data. Monte Carlo simulation methods were then used to investigate the influence of the direct and indirect (scatter) components of the electron beam on dose in a water phantom, which included the influence of field size and SSD.

2.2 MATERIALS AND METHODS

2.2.1 Measurements

Central axis percentage depth dose curves and R_{max} dose profiles were measured for 6, 9 and 12 MeV electron beams and fields 5 cm in diameter, 10×10 cm^2, 15×15 cm^2, and 20×20 cm^2 at 100 cm SSD. These measurements were performed in a water phantom using a 1 mm^2 p-type Si diode detector 2.5 µm thick (PTW, Freiburg, Germany) and a 0.3 cm^3 thimble chamber (PTW) respectively.

Extended SSD factors (i.e. beam outputs relative to the output at 100 cm SSD) were measured using a Roos chamber (PTW) with an active volume of 0.35 cm^3. This device was calibrated (NPL, Teddington, U.K.) with a reported uncertainty of 1.6%. Measurements were taken at the depth of maximum dose, R_{max}, for each setup, typically 1.3 cm, 2.05 cm, and 2.7 cm for 6 MeV, 9 MeV, and 12 MeV, respectively. All measurements and subsequent conversions to dose were performed using Institute of Physics and Engineering in Medicine Code of Practice (Thwaites et al. 2003).

2.2.2 Monte Carlo Calculations

2.2.2.1 Accelerator Treatment Head Modelling

BEAMnrc (Rogers et al. 2005) was used to model the Siemens Oncor accelerator

treatment head using manufacturer provided specifications for 6 – 12 MeV beam energies and 100 cm, 110 cm and 120 cm SSD. The data provided by the manufacturer included estimates of electron beam energy and spot size incident on the primary scattering foil and therefore the exit window was not modelled. Figure 2.1 shows the treatment head components included in this study. Component modules (CM) were used in BEAMnrc to model the primary scattering foil, secondary scattering foil, electron monitor chamber, jaws and multi-leaf collimator, respectively. The 6 MeV electron beam does not use a primary scattering foil (A) and is broadened by the secondary scattering foil (B) only.

The applicator, which is positioned between z = 56 cm and z = 95 cm from nominal source, comprises of 5 main parts. For the purposes of this work, these parts were designated as scrapers 1 – 5 respectively. Scraper 1 was the upper trimmer, nearest the nominal source and was composed of aluminium. Scraper 2 formed the applicator side walls and was also aluminium. Scraper 3 and 4 were composed of steel and aluminium, respectively, and together formed the middle trimmer. Finally, scraper 5, composed of brass, was the final field defining component nearest to the phantom surface.

The electron source, incident on the primary scattering foil, was modeled as a mono-energetic electron beam with Gaussian spatial spread. The manufacturer estimated beam energies incident on the primary scattering foil were 6.64 MeV, 9.82

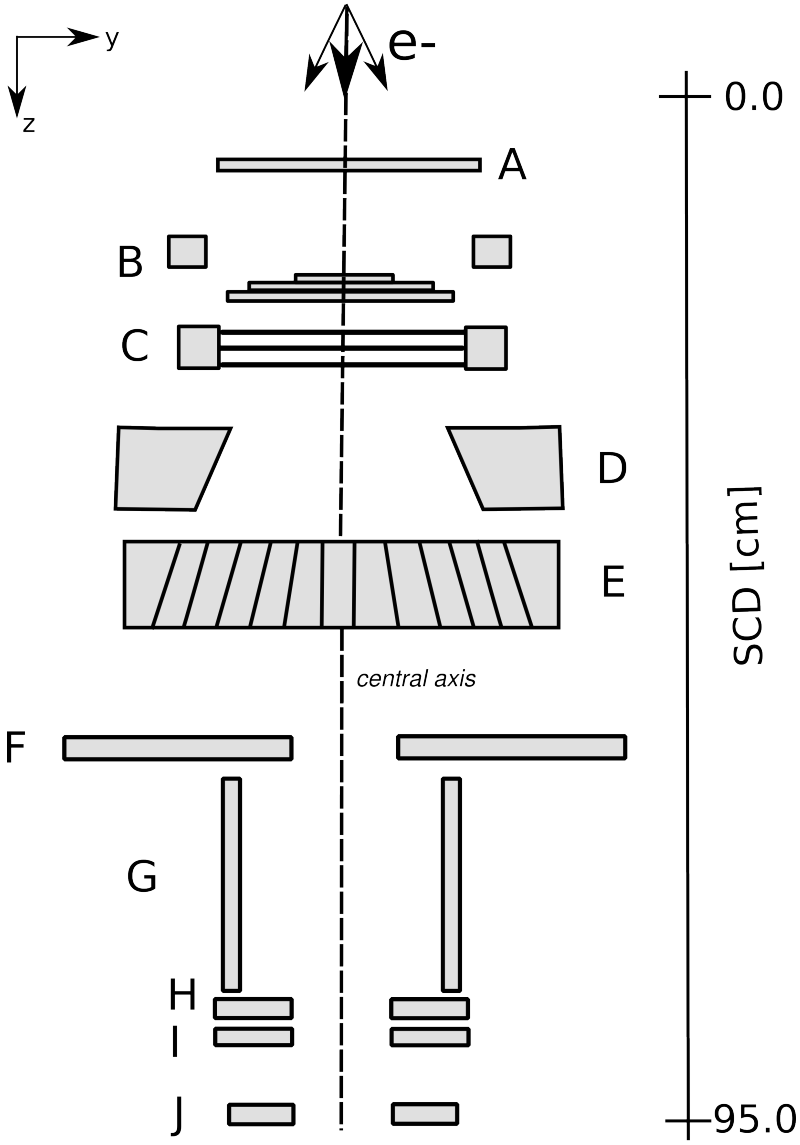

Figure 2.1 Schematic of the Siemens Oncor (Siemens Healthcare, Erlangen, Germany) treatment head, showing components included in BEAMnrc Monte Carlo simulations. A: primary scattering foil (CM FLATFILT), B: secondary scattering foil (CM CONESTAK), C: electron monitor chamber (CM CHAMBER), D: jaws (CM JAWS), E: multi-leaf collimator (CM MLC) and applicator (CM APPLICAT) scrapers 1 - 5, labelled F - J, respectively.

MeV and 13.12 MeV for the 6 MeV, 9 MeV and 12 MeV beams with the bending magnet energised with currents of 12.7 A, 18.1 A and 23.7 A, respectively. These energies were initially used in Monte Carlo simulation.

Each CM in the accelerator model was assigned a LATCH bit. This particle tracking variable allows detailed particle interaction history to be extracted upon completion of the simulation. The main EGSnrc/BEAMnrc input parameters used were ECUT=AE and PCUT=AP of 0.521 and 0.01 MeV, respectively. The default global SMAX and ESTEPE values of 5.0 cm and 0.25 were used, respectively. The boundary crossing algorithm was PRESTA-I. The electron transport step algorithm was PRESTA-II.

2.2.2.2 Dose Calculations

The accelerator model generated with BEAMnrc was compiled as a shared library and run by the DOSXYZnrc (Walters et al. 2006) user code. This approach eliminated the need to store intermediate phase-space data, which requires large amounts of disk space. In the shared-library method, the entire treatment head transport and water phantom dose calculation is performed in a single simulation step by DOSXYZnrc (Kawrakow and Walters 2006).

DOSXYZnrc was used for dose calculations in water phantom models. The accelerator head model configured in BEAMnrc was validated by comparing measured

and DOSXYZnrc calculated percentage depth dose curves and R_{max} in-plane dose profiles. Model fine-tuning was necessary to improve the agreement between measurements and calculations. This fine-tuning involved adjustments to the electron source energy (E), full width at half maximum (FWHM, r_s) and the addition of a mean angular spread ($\phi'(\Theta)$) to the incident electron beam. The mean angular spread ($\phi'(\Theta)$) was adjusted to match the average dose at ±7 cm from the central axis for the largest field size (20 x 20 cm^2). The source model producing the best agreement (2% / 0.1 cm)

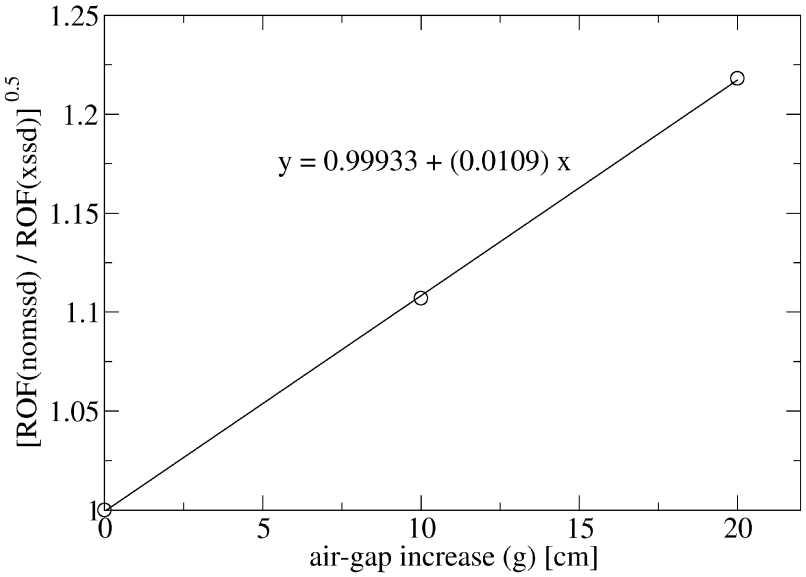

Figure 2.2 Plot of the square root of the ratio of output at nominal SSD (100 cm) to output at extended SSD as a function of increase in air-gap (g) for 9 MeV electron beams and 5 cm diameter field size.

with measured percentage depth dose (R_{50}) and dose profiles was chosen to be the fine-tuned model.

The number of histories in the DOSXYZnrc input were specified to produce a statistical uncertainty in calculated dose approaching 1%. The number of histories simulated depended on nominal beam energy, field size, and SSD. For example, for the largest field (20×20 cm^2), simulation of 1×10^7 primary electrons resulted in 2.9×10^6, 3.3×10^6 and 3.5×10^6 particles (electrons and bremsstrahlung x-rays) reaching the plane of isocenter for the 6 MeV , 9 MeV and 12 MeV electron beams, respectively.

DOSXYZnrc was also used to configure a water phantom model for extended SSD factor calculations. A $0.5 \times 0.5 \times 0.5$ cm^3 voxel was centered at R_{max} to represent the detector used for measurements. Extended SSD factors were calculated using equation 1.18 and the calculated dose per incident particle in the voxel. Dose components were extracted using the LATCH filter (Walters et al. 2006).

In addition to the comparison with measured output factors, Monte Carlo calculated extended SSD factors were also compared with the output calculated by the Effective SSD method (Khan 1984). Correcting the output variation with airgap using the Effective SSD method involves: (1) plotting the square root of the ratio of output at nominal SSD (100 cm) to that at extended SSD versus increase in air-gap (g) (figure 2.2), (2) performing a linear regression and (3) obtaining the slope (m). The effective

SSD (SSD_{eff}) is then given by:

$$SSD_{eff} = \frac{1}{m} - R_{max} \tag{2.1}$$

where R_{max} is the depth of maximum dose for a given beam energy and field size. The corrected output at extended SSD can then be calculated using:

$$ROF_{cor} = \frac{SSD_{eff} + R_{max}}{SSD_{eff} + R_{max} + g} \tag{2.2}$$

2.3 RESULTS

2.3.1 Percentage Depth Dose Curves, Dose Profiles and Extended SSD Factors

The treatment head model fine-tuning process resulted in source energies incident on the primary scattering foils (E) of 6.33 MeV, 9.20 MeV, and 12.25 MeV and mean angular spreads ($\phi'(\Theta)$) of 5.1°, 4.3° and 0.9° for 6 MeV, 9 MeV, and 12 MeV electron beams, respectively. The FWHM (r_s) was set to 0.1 cm. The model was validated by comparison of measured and calculated percentage depth dose curves and dose profiles in water. Calculated depth dose curves and dose profiles were extracted using STATDOSE (McGowan et al. 2006). Data was normalised to R_{max} on the central axis. Figure 2.3 and 2.4 show comparisons of the in-plane R_{max} profiles and central axis percentage depth dose curves for the 10×10 cm^2 field. Differences between measured

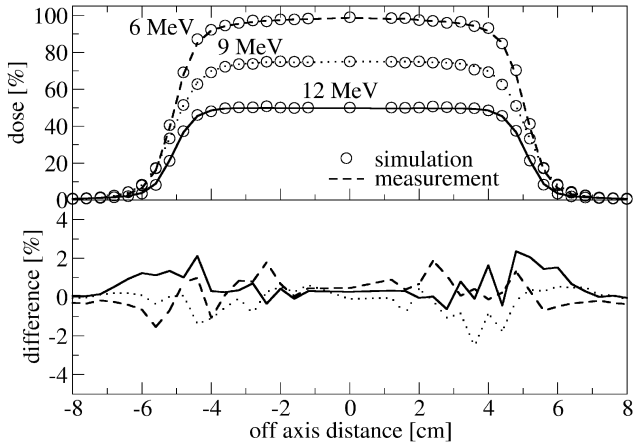

Figure 2.3 Comparison of measured and calculated dose profiles for the 10 × 10 cm² field size at 100 cm source-to-surface distance.

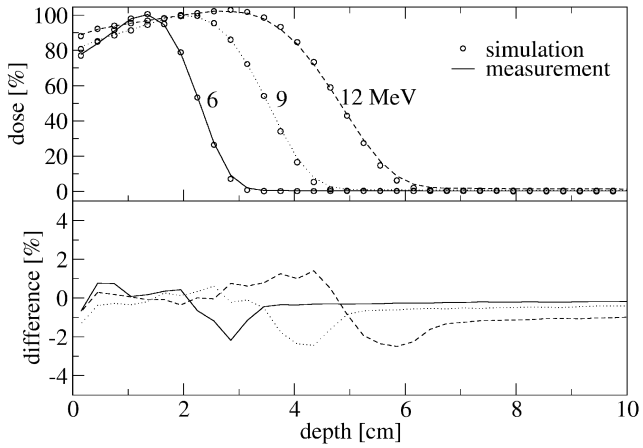

Figure 2.4 Comparison of measured and calculated percentage depth dose curves for the 10 × 10 cm² field size at 100 cm source-to-surface distance.

and calculated dose distributions were within 2% or 0.1 cm (at R_{50}) for the range of beam energies and field sizes investigated.

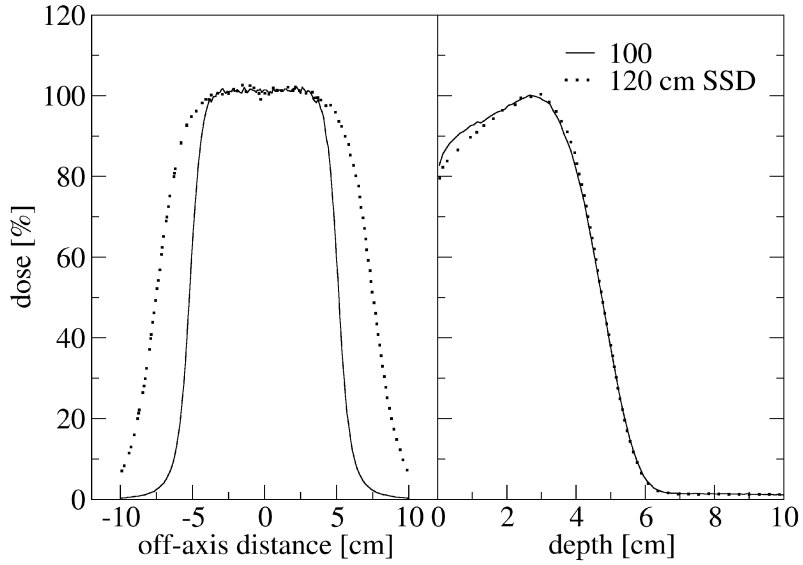

Figure 2.5 Effects of extended source-to-surface distance (SSD) on Monte Carlo calculated percentage depth dose curves and dose profiles, in this case for a 12 MeV electron beam and 10 × 10 cm² field size (solid line = 100 SSD; dotted line = 120 SSD).

BEAMnrc simulated electron beams showed results similar to measured and published results (Cygler et al. 1997, Das et al. 1995, Rajasekar et al. 2002). Minimal effects of extended SSD on the characteristic parameters of the depth dose curves were observed, represented by a dose reduction in the buildup region. The dose fall-off

region remained relatively independent of SSD (figure 2.5). Relative output declined with increase in SSD (figure 2.6). For the smallest field, defined by the applicator 5 cm in diameter, relative output declined more rapidly than it did for the larger fields. For the larger fields (10×10 cm^2, 15×15 cm^2, 20×20 cm^2), the relative output reductions with increase in SSD were comparable. Relative outputs showed obvious deviations from the ISL with extended SSD for some configurations. For 12 MeV, the larger fields followed the ISL quite well. However, for the field 5 cm in diameter, significant deviations occured. For 6 MeV, all fields showed large deviations from the ISL. Monte Carlo calculations were found to be in good agreement with the effective SSD method, which is often used to correct for non-standard SSD electron beams in clinical calculations (figure 2.6 and 2.7), within 2% over the entire range of the study.

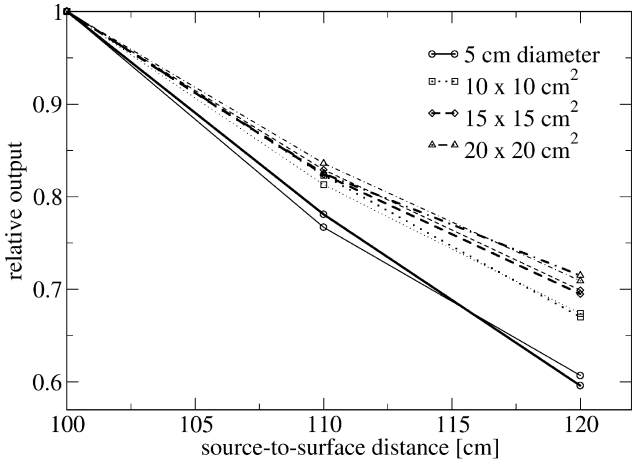

Figure 2.6 Monte Carlo (thick lines) and effective SSD (thin lines) calculated output at 9 MeV.

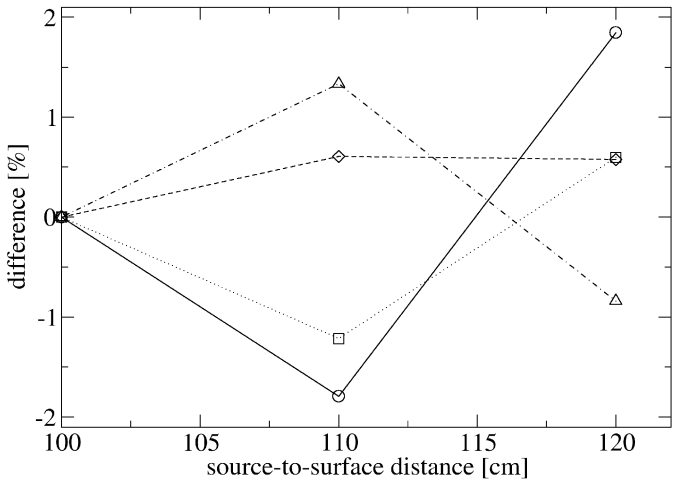

Figure 2.7 Percentage differences between Monte Carlo and effective source-to-surface distance (SSD_{eff}) calculated relative outputs for 9 MeV electron beam as shown in figure 2.6.

2.3.2 Calculations at R_{max}

Table 2.1 compares measured and calculated extended SSD factors for the three electron beam energies and four applicator defined fields included in the study. A difference of less than 2% was observed between measurements and calculations, with a single exception.

Monte Carlo calculated extended SSD factors were decomposed into contributions from the various treatment head components: the direct factor (ROF_{direct}) attributable to dose scored by direct particles (that is, electrons emanating directly from

Table 2.1 Comparison of calculated and measured extended source-to-surface distance (SSD) factors.

Energy (MeV)	Field size (cm²)	SSD (cm)	Measured	Calculated	Calc. uncert. (%)	Difference (%)
6	5 cm dia	100	1.000	1.000	1.1	~
		110	0.734	0.721	1.3	1.8
		120	0.516	0.526	1.5	1.8
	10 × 10	100	1.000	1.000	0.6	~
		110	0.800	0.786	0.6	1.7
		120	0.651	0.639	0.7	1.9
	15 × 15	100	1.000	1.000	0.8	~
		110	0.827	0.840	0.8	1.5
		120	0.690	0.704	0.9	2.0
	20 × 20	100	1.000	1.000	0.9	~
		110	0.837	0.822	1.6	1.8
		120	0.701	0.688	1.1	1.9
9	5 cm dia	100	1.000	1.000	0.8	~
		110	0.783	0.781	0.9	0.3
		120	0.602	0.596	1.0	1.0
	10 × 10	100	1.000	1.000	0.9	~
		110	0.816	0.823	1.0	0.9
		120	0.674	0.670	1.1	0.6
	15 × 15	100	1.000	1.000	1.3	~
		110	0.833	0.824	1.1	1.0
		120	0.698	0.695	1.2	0.4
	20 × 20	100	1.000	1.000	1.0	~
		110	0.836	0.825	1.1	1.4
		120	0.707	0.715	1.2	1.2
12	5 cm dia	100	1.000	1.000	0.9	~
		110	0.796	0.797	1.0	0.2
		120	0.641	0.647	1.1	0.9
	10 × 10	100	1.000	1.000	0.9	~
		110	0.826	0.828	0.9	0.3
		120	0.690	0.698	1.0	1.2
	15 × 15	100	1.000	1.000	0.9	~
		110	0.838	0.833	1.0	0.6
		120	0.706	0.703	1.0	0.5
	20 × 20	100	1.000	1.000	1.0	~
		110	0.840	0.818	1.1	2.7
		120	0.711	0.705	1.2	0.8

the source, scattering only in the scattering foils, dose chamber and intervening air) and the indirect factor attributable to dose from collimator-scattered particles. The indirect factor was decomposed into the separate contributions from the jaws and MLC ($ROF_{seccoll}$) and each applicator scraper (ROF_{scrap1}, ROF_{scrap2}, $ROF_{scrap3+4}$ and ROF_{scrap5}). Output components were analysed as a percentage of total dose at R_{max} on the central axis at a given SSD.

Table 2.2 Decompostion of 12 MeV electron beam extended SSD factors into direct and indirect (collimator-scattered) components. Each component is given as a percentage of the total dose at R_{max} on the central axis at a given SSD.

Field size (cm^2)	SSD (cm)	ROF_{direct} (%)	$ROF_{seccoll}$ (%)	ROF_{scrap1} (%)	ROF_{scrap2} (%)	$ROF_{scrap3+4}$ (%)	ROF_{scrap5} (%)
5 cm dia	100	88.5	5.4	0.6	0.5	3.0	2.0
	110	90.4	5.6	0.4	0.1	1.9	1.6
	120	91.9	5.6	0.3	0.1	0.7	1.4
10 × 10	100	89.8	4.3	1.1	1.0	2.5	1.3
	110	90.0	4.0	1.0	0.1	3.4	1.5
	120	89.7	3.8	0.9	0.1	3.9	1.6
15 × 15	100	91.1	3.6	2.6	0.3	1.8	0.6
	110	90.1	3.4	2.5	0.1	2.7	1.2
	120	89.5	3.5	2.3	0.1	3.4	1.2
20 × 20	100	94.6	2.9	0.7	0.6	1.1	0.1
	110	93.6	2.5	0.6	0.4	2.1	0.8
	120	92.8	2.7	0.7	0.2	2.5	1.1

The results of the decomposition of extended SSD factors into direct and

indirect components are shown for the 12 MeV electron beam in table 2.2. The direct component was found to be the major contributor to output in all cases, as expected. This contribution increased with increase in field size, while the indirect component decreased. The direct component appeared to follow the ISL quite well, especially for for the higher (9 – 12 MeV), lower scattered beam energies. Contributions from the applicator scrapers varied with field size. Scrapers 3 and 4 (the middle trimmer bar) and 5 (the distal field defining scraper) were in most cases the principal contributors to the applicator dose component. The jaws and MLC scattered dose component showed that the contribution from these secondary collimators decreased with increase in field size.

With increasing airgap (SSD) it was found that for the smaller fields (particularly the field 5 cm in diameter) and higher beam energies, direct and indirect dose components showed trends opposite to those of the larger fields (especially as the SSD was increased from 100 cm to 110 cm). For the field 5 cm in diameter, the direct component tended to increase with increase in SSD, and the indirect components decreased. For the larger fields, the direct component tended to decrease, and the indirect component tended to increase. For all energies, the jaws and MLC output component remained relatively constant (to within 0.5%) with increase in SSD.

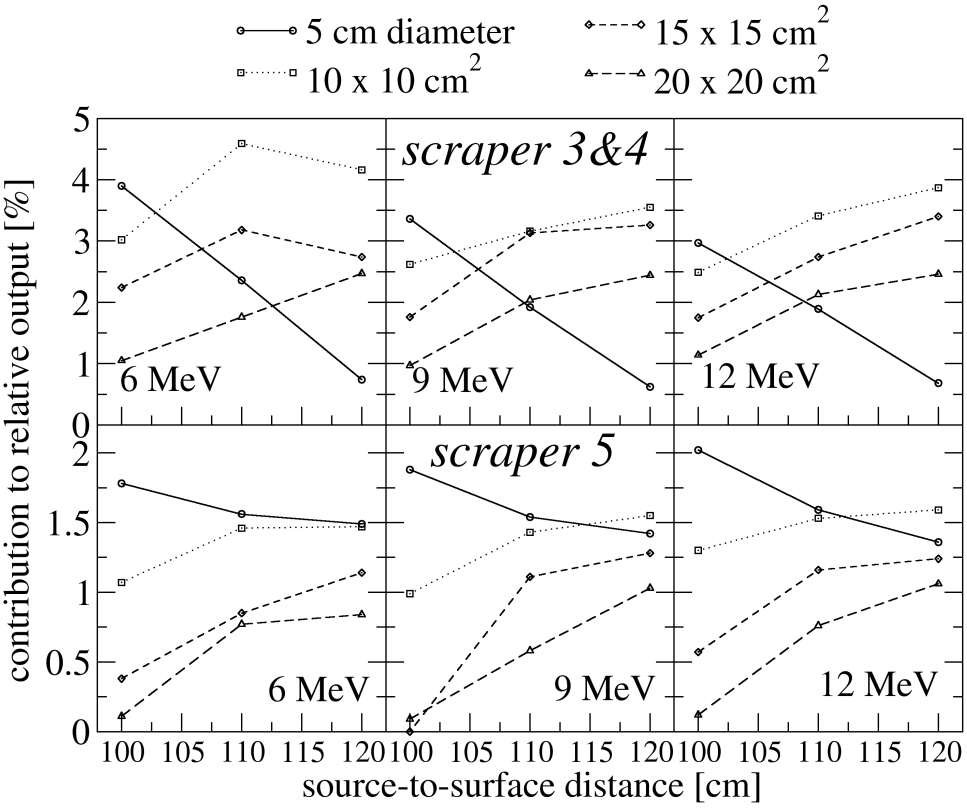

Figure 2.8 Variation in Monte Carlo calculated dose contribution from applicator scrapers 3 and 4 (top row) and 5 (lower row) to relative output at R_{max} with extended source-to-surface distance (SSD) for 6 MeV, 9 MeV and 12 MeV electron beams.

Investigating the applicator scattered dose showed that for all energies and SSDs, the 15 × 15 cm^2 applicator demonstrated the largest scraper 1 contribution to total output. This is likely due to the applicator design, with the square opening of the aluminium trimmer relatively closer to the beam axis, compared to the other applicators. For scraper 2, the contribution to total dose increased with increasing

energy. It was also found that the lowest energy beam (6 MeV) showed the largest output contribution from scrapers 3 and 4, while the higher energy beam (12 MeV) showed the largest output contribution from scraper 5 (figure 2.8). As the SSD was increased, the output contributions from scrapers 3, 4, and 5 clearly showed an opposite trend between the field 5 cm in diameter and the larger fields. For the field 5 cm in diameter, the dose contributions decreased with increase in SSD. For the larger fields, dose contributions increased with increase in SSD.

2.3.3 Electron Angular Distributions

Figure 2.9 shows the angular distributions of electrons scattered from the applicators 5 cm in diameter and 20 × 20 cm^2 for 6 MeV and 12 MeV at 100 cm and 120 cm SSD. This analysis was performed in BEAMDP (Ma and Rogers 2006) using phase-space data below the applicator. The scoring field was configured to represent the transverse cross-section of the 0.5 × 0.5 × 0.5 cm^3 R_{max} dose calculation voxel. Angular distributions were plotted as the relative number of electrons per angular bin versus the scattering angle in degrees.

At 100 cm SSD, the large peak at approximately 12° for the applicator 5 cm in diameter represents electron tracks from the lower scrapers (figure 2.9). At 120 cm SSD, many of these tracks no longer contribute to the output. The distribution shifts

toward smaller angles, and the number of electron tracks declines significantly. The 20 × 20 cm^2 applicator distributions clearly show tracks from the final scrapers, that is, the peak around 30 degrees (attributable to scatter from scrapers 3 and 4) and the peak around 60 degrees (attributable to scatter from scraper 5). At 120 cm SSD, the distributions lose the large-angle tracks and shift toward more acute angles. The absolute number of electron tracks does not decline, however, resulting in a large number of acute-angle electron tracks influencing the output at 120 cm SSD.

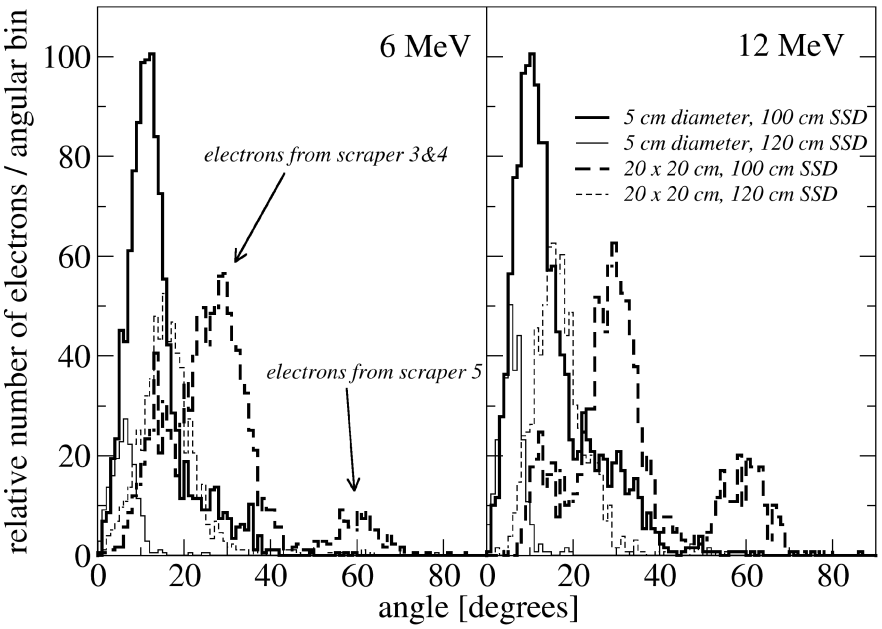

Figure 2.9 Angular distributions of applicator-scattered electrons crossing a plane representing the transverse cross-section of the R_{max} voxel.

2.4 DISCUSSION

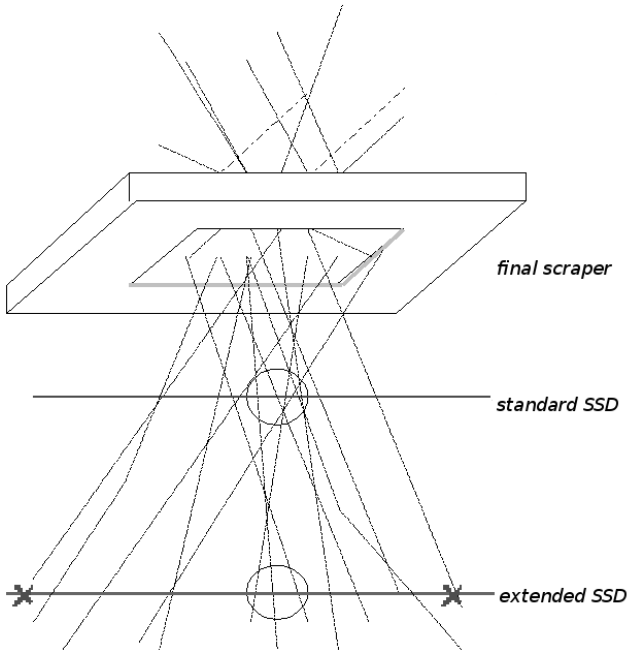

Figure 2.10 Diagram of electron tracks through the final scraper of the electron applicator.

Monte Carlo calculated depth dose curves and dose profiles are in agreement with the measured and published results of increasing the SSD from the nominal value (Cygler et al. 1997, Das et al. 1995, Rajasekar et al. 2002). The relative output at extended SSD for the smallest field was also found to decrease more rapidly than that for the larger fields (Rajasekar et al. 2002). For the field 5 cm in diameter, the jaws, MLC and applicator scrapers are closer to the beam central axis, and scattered radiation therefore affects the dose at R_{max} to a greater extent. Some of these electrons are scattered at

angles such that they cannot reach the detector at extended SSD (figure 2.10). For the larger fields, the treatment head collimators are further from the beam central axis, resulting in fewer scattered electrons influencing dose at R_{max}. However, as SSD increases, electrons scattered at relatively acute angles can reach the R_{max} point (Rajasekar et al. 2002). For the applicator 5 cm in diameter, relative output is affected by increased distance (ISL) and loss of scattered radiation. For larger fields, on the other hand, output is affected by ISL, but more scattered electrons reach the detector at R_{max}.

The analysis of the direct and indirect components of the Monte Carlo calculated extended SSD factors has shown results similar to those in previous studies. (Kapur et al. 1998, Zhang et al. 1999). The direct component has been found to be approximately 90% of the dose at R_{max} for large fields on a Siemens MD2 accelerator (Zhang et al. 1999). In the present work, the direct component ranged from approximately 90% for the smallest field to approximately 95% for the largest field. As with the study by Zhang et al. (1999), for a given field, the percentage dose component from the jaws and MLC remained relatively constant with change in SSD. In the present study, the applicator contributed more to R_{max} dose than the jaws did under most configurations. In the investigation by Zhang et al., it was found that about 50% of the scattered dose component came from the jaws; the other 50% came from the applicator scrapers. Scrapers 3 and 4 (the middle trimmer) were found to contribute the most to

the applicator scatter dose component because it has the largest vertical face (excluding scraper 2). This finding is consistent with a previous study of the Siemens electron applicator (Ebert and Hoban 1995).

Analysis of the variation in output contributed by applicator scrapers 3, 4, and 5 with increasing SSD showed different trends between the field 5 cm in diameter and the larger fields (figure 2.8). This observation assists the explanation of the more rapid output reduction for the field 5 cm in diameter compared with the larger fields. It is caused by a reduction in scattered dose contributions from scrapers 3, 4, and 5 with increase in SSD. The angular distributions of applicator-scattered electrons (figure 2.9) support these contentions. The relative number of electron tracks from the applicator contributing to the output at extended SSD is seen to be reduced significantly for the field 5 cm in diameter. However, for the larger fields, this reduction in electron tracks is not seen, as the acute-angle scattered electrons which do not reach the detector at standard SSD contribute to the output at extended SSD.

2.5 CONCLUSIONS

The Monte Carlo simulation code BEAMnrc was used to model the treatment head of a Siemens Oncor accelerator for electron fields at standard and non-standard SSD. There was good agreement (difference < 2%) between measured and calculated extended SSD

factors. Decomposing Monte Carlo calculated outputs and analysis of scattered electron angular distributions helped in understanding the variation in output with field size and SSD. The dose contributed by electrons scattering off the lower applicator scrapers decreased with increase in SSD for the applicator 5 cm in diameter, and the angular distribution showed only a small number of acute-angle electron tracks reaching the detector at extended SSD. However, for the larger fields, the dose component from the lower scrapers increased with increase in SSD, and angular distributions showed that a larger number of acute-angle electron reached the detector at extended SSD.

This study has investigated some of the uncertainty, namely, variation in output and dose distributions, surrounding extended SSD electron beams on a Siemens Oncor accelerator. Monte Carlo simulation allows the extraction of data which would be very difficult or impossible to measure. Accurate data is highly dependent on the accuracy of the treatment head model. In addition, since electron-beam characteristics are a complex function of accelerator head geometry, these results may not apply to other accelerator of the same model. Nevertheless, trends in Monte Carlo calculated quantities have helped to explain some of the physical effects seen when using extended SSD.

3. Monte Carlo Treatment Head Model Commissioning based on Large Field Measurements

3.1 INTRODUCTION

Accurate dose calculation is important for the clinical use of electron beams and the development of new electron therapy techniques, such as modulated electron therapy (Ma et al. 2003). Monte Carlo simulation can potentially be used to accurately calculate the electron fluence at the patient surface and resultant dose deposition if source and geometry parameters are well characterized (Chetty et al. 2007). The viability of using Monte Carlo methods to commission electron beams has also been studied (Antolak et al. 2002). In that work, calculated small field (3×3 cm^2 and 6×6 cm^2 cerrobend insert) electron dose distributions were generally within 2% / 0.1 cm of measurements. However, many of the large (10×10 cm^2 and 25×25 cm^2) open applicator fields failed the 2% / 0.1 cm criteria. The authors noted that failure to meet the criteria may have been due to (1) problems in the Monte Carlo code (e.g. approximations in the multiple scattering or energy loss), (2) inaccuracies in the simulation geometry, (3) inaccurate approximation of the initial electron source or (4) uncertainties in the measured data. More accurate simulations will benefit Monte Carlo-based treatment planning and

related applications such as the final aperture superposition technique, used for fast, accurate patient-specific relative output factor (ROF) and depth dose curve calculations (Chen et al. 2009).

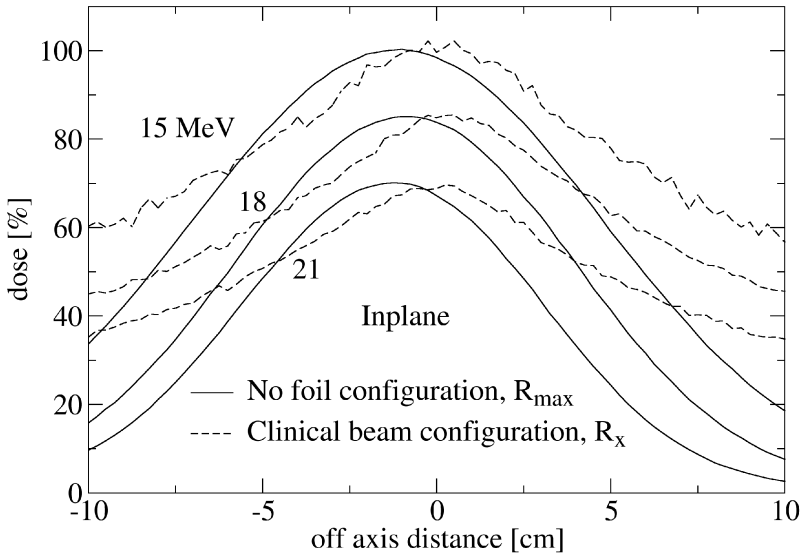

Figure 3.1 Profiles measured at R_{max} in the no foil configuration (solid lines) compared to profiles measured in the bremsstrahlung tail at R_x for the clinical beams (dashed lines). The relative shift in the peaks was due to the presence of a fringe magnetic field from the bending magnet extending into the treatment head (reproduced from Faddegon et al. 2009).

One approach to obtaining data for modelling electron beams has been the measurement and Monte Carlo simulation of dose distributions using the maximum

field size available on the linear accelerator (linac) (Huang et al. 2005, Faddegon et al. 2005, Weinberg et al. 2009). This approach takes advantage of the absence of lower energy, widely scattered electrons from the applicator (van Battum 2003). Janssen et al. (2001) published a methodology that used a limited set of 'uncollimated' electron beam measurements to generate a model for clinical electron beams. Central axis depth dose curves and dose profile measurements made with maximum jaw setting and no electron applicator have been used to determine the source and geometry parameters for Monte Carlo simulations (Faddegon et al. 2005). Treatment head disassembly was used to improve the accuracy of these simulations (Faddegon et al. 2009). In that work, a fringe magnetic field in the region between the exit window and monitor chamber was found to deflect electrons approximately 1 cm off the beam axis at the machine isocentre (figure 3.1). Dose distributions were measured at various stages of treatment head reassembly, which reduced the number of simulation variables, and resulted in improved agreement between simulated and measured dose distributions (within 1.5%/0.9 mm for depth dose curves and 2.6%/1.6 mm for profiles at the depth of maximum dose, R_{max}) without simulating the magnetic field. In addition, Faddegon et al. (2009) used EGSnrc (Kawrakow and Rogers 2006) which simulates multiple scattering more accurately than the earlier version used in previous studies, EGS4 (Nelson et al. 1985).

Initial work in this thesis (chapter 2) and a number of published studies (Kapur

et al. 1998, Zhang et al. 1999, Verhaegen et al. 2001) have tuned source parameters using smaller applicator collimated fields and took geometry parameters directly from manufacturer specifications. The electron sources were typically simulated using mono-energetic pencil beams (radius ≈ 1–2 mm) with energies tuned to match R_{50} (the depth at which the dose on the central axis falls to 50% of its maximum). Although these models resulted in accurate calculations for certain conditions, unexplained discrepancies between measurement and simulation for larger fields were evident in some cases. In particular, the dose profiles of larger applicator-defined electron fields exhibited up to 4% differences (Verhaegan et al. 2001).

Although 40 × 40 cm^2 electron fields have clinical uses (e.g. total body irradiation, Pavon et al. 2003), most treatments with electron beams involve use of electron applicators and lead alloy inserts. It is important to validate the use of source and geometry parameters—extracted from large electron field simulations—for these smaller fields and to verify that the dose distributions with the applicators and inserts are accurate. In principle, discrepancies not seen for the largest field may become evident with applicators, inserts and reduced jaw settings.

Small electron fields also present more complex dosimetry, especially when the field size is smaller than the practical range (R_p) of the electron beam and lateral scatter non-equilibrium conditions are present (Das et al. 2008). In this case, Monte Carlo simulation may be a beneficial tool as it can accommodate high spatial resolution and

will not be affected by perturbation problems encountered in measurements, as it can be used to calculate dose-to-water directly, in regions of arbitrary sizes.

In the current investigation, source and geometry parameters derived from the simulation of a Siemens Oncor linac at the maximum field size (40 × 40 cm^2) (Faddegon et al. 2009) were used to simulate smaller square and circular electron fields ranging from the largest open applicator (25 × 25 cm^2) to a 1 cm diameter insert. Dose distributions and ROF calculated by Monte Carlo simulations were compared with those measured in water with ionisation chambers and diode dosimeters to perform a comprehensive validation.

3.2 MATERIALS AND METHODS

3.2.1 Measurements

Measurements were performed on a Siemens Oncor accelerator (Siemens Healthcare, Erlangen, Germany) for nominal electron energies of 6 – 21 MeV and standard electron applicators of 5 cm diameter, 10 × 10 cm^2, 15 × 15 cm^2, 20 × 20 cm^2 and 25 × 25 cm^2. Measurements were also taken for fields collimated with circular cerrobend (Cerro Metal Products Corporation, Bellefonte, PA) inserts of thickness 1.3 cm and nominal opening diameters 1, 1.5, 2, 3 and 5 cm placed in the final scraper bar of each square applicator. The insert openings were measured with callipers to be 1.00, 1.38, 2.21, 2.93

and 5.22 cm, respectively.

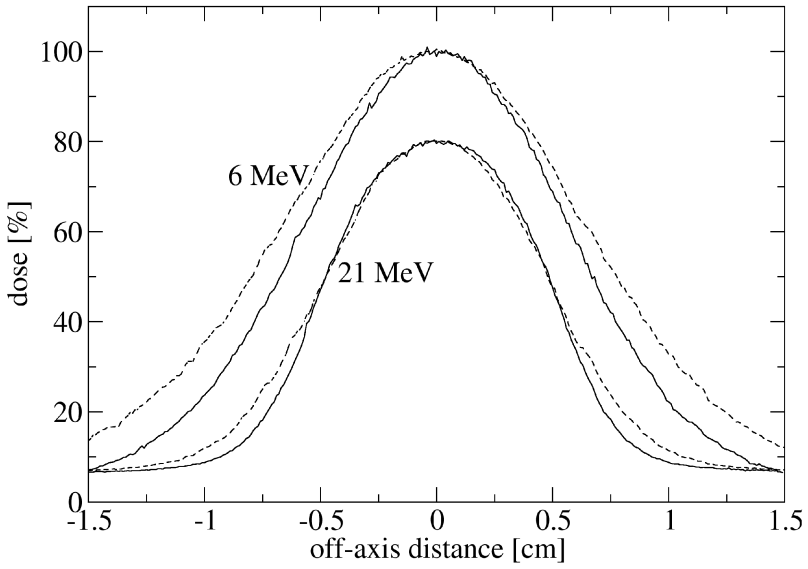

Figure 3.2 Dose profiles for 1 cm diameter cerrobend insert measured in water with a electron diode (solid lines) and a larger CC13 thimble ionisation chamber (dashed lines) which leads to visible volume averaging errors.

Measurements were made with ionisation and diode detectors. A CC13 (Scanditronix–Wellhofer, Uppsala, Sweden) thimble chamber with an effective volume of 0.13 cm^3 was used for off-axis ratio (dose profile) measurements in open applicator collimated fields. Depth dose curves and dose profiles were measured with an electron field detector (EFD^{3G}) p-type diode (Scanditronix–Wellhofer) for the full set of field

sizes. The diode was used to ensure high spatial resolution when measuring fields collimated with cerrobend inserts. Its smaller size (0.02 cm diameter active area) is clearly advantageous over the larger CC13 ionisation chamber (0.06 cm diameter) for small field measurements (figure 3.2). The diode is also advantageous as it acquires dose readings directly (Das et al. 2008).

Wang and Rogers (2007) used the EGSnrc Monte Carlo code to model and study the response of the Scanditronix–Wellhofer diode used in this work. They found that the diode response is (1) almost flat with respect to depth in water, (2) independent of energy to within 2% at the reference depth (i.e. $0.6R_{50}$ - 0.1 cm, Almond et al. 1999) and (3) almost independent of field size. However, electron diodes are known to over-respond to bremsstrahlung photons (Turian et al. 2004, Das et al. 2008). This over-response is up to 5% for the highest energy electron beam (21 MeV) on a Siemens accelerator (Faddegon et al. 2005). It leads to a 1% under-measurement of the off-axis ratio for large electron fields when using a Scanditronix–Wellhofer electron field detector (EFD) diode (Faddegon et al. 2009). The thimble chamber was used for the open applicator dose profile measurements, as it does not exhibit this over-response. For smaller fields (collimated by cerrobend inserts), however, the bremsstrahlung is effectively constant across the field and therefore the over-response has a negligible effect on normalized dose profiles.

Song et al. (2006) and Das et al. (2008) advised the comparison of diode and

ionisation chamber measurements to confirm correct operation and accuracy in data. For open applicator fields, percentage depth ionization (PDI) curves and percentage depth dose (PDD) curves were measured with a (0.35 cm^3 effective volume) Roos (PTW, Freiberg, Germany) parallel plate chamber and the Scanditronix–Wellhofer EFD diode, respectively. Depth penetration measurements extended 3 cm beyond the practical range (R_p) and 1 cm above the water surface. The uncertainty in depth penetration for the Roos chamber was 0.08 cm, including an uncertainty of 0.06 cm for a possible change in the electron perturbation factors (p_{wall} and p_{cav}) with depth (Faddegon et al. 2009). The uncertainty for the diode depth penetration was estimated as 0.05 cm. PDI was converted to dose-to-water using TG51 protocol (Almond et al. 1999). The diode was up to 2% lower than the Roos chamber from the surface to 0.1 cm depth. At larger depths, the diode and Roos chamber PDD matched to within 0.05 cm. Therefore, the diode could be used for accurate PDD measurements. The epoxy resin above the active region of the diode resulted in inaccurate PDD from the surface to 0.05 cm depth, so this region was excluded from quantitative comparisons with Monte Carlo simulations.

Off-axis ratios (dose profiles) were measured in the cross-plane (x) and in-plane (y) directions at four depths: 0.5 cm, at the maximum of the PDD curve (R_{max}), the depth at which dose fell to 50% of its maximum (R_{50}) and in the bremsstrahlung tail (R_x). The measurement depths were the same for all field sizes for a given energy and

were determined for each energy using the 10 × 10 cm^2 applicator with no inserts. This field size was chosen because it is a broad beam reference field with a limited effect of lateral scatter dis-equilibrium on dosimetry. Profile measurements were also performed along the diagonal axes of the 25 × 25 cm^2 applicator.

Table 3.1 R_{max} and R_{50} values for 6–21 MeV electron beams and 1–5 cm diameter inserts measured with the diode. The 10 × 10 cm^2 applicator nominal values are included for comparison.

Energy (MeV)	Field size (cm)	R_{max} (cm)	R_{50} (cm)	Field size (cm)	R_{max} (cm)	R_{50} (cm)
6	1	0.3	1.36	1.5	0.5	1.95
9		0.3	1.99		0.6	2.43
12		0.4	2.38		0.7	2.88
15		0.6	2.85		0.8	3.42
18		0.6	3.30		0.7	3.98
21		0.6	3.55		0.8	4.28
6	2	1.0	2.25	3	1.3	2.34
9		1.1	3.13		1.6	3.47
12		1.2	3.76		1.8	4.32
15		1.4	4.44		1.8	5.17
18		1.2	5.16		1.3	6.02
21		1.2	5.55		1.4	6.50
6	5	1.3	2.24	10 × 10	1.3	2.34
9		2.0	3.57		2.0	3.56
12		2.6	4.79		2.7	4.79
15		2.0	5.96		3.0	6.05
18		1.5	7.19		2.1	7.48
21		1.6	7.88		1.9	8.33

Data were measured using a 60 × 60 × 58 cm^3 scanning water phantom (Wellhofer Dosimetrie, Schwarzenbruck, Germany) with source-to-surface distances (SSD) of 100 and 120 cm. The water tank was levelled to ± 0.1 cm. Detectors were

centred to within 0.05 cm, either on the collimator rotation axis using the 12 MeV electron beam as described by Faddegon et al. (2009) or, for cerrobend insert collimated fields, on the 50% dose points of cross-plane and in-plane scans. The detector position at the water surface was defined using the reflection method. The scanning software was used to set the effective point of measurement for each detector (EFD diode: 0.09 cm, Roos chamber: 0.13 cm and CC13 thimble chamber: 0.15 cm). Data were obtained in continuous scanning mode, at under 0.05 cm s^{-1} for the smallest fields. This was to ensure minimal water displacement and increased data points to improve the signal-to-noise ratio. The reference detector was positioned at the edge of the field to minimize scatter from this detector reaching the field detector. Field and reference detector charges were measured using a CU500E electrometer (Wellhofer Dosimetrie). The water level was checked regularly and water added to account for evaporation and to maintain the detector depth.

ROF were measured with a parallel plate chamber (Roos) and EFD diode for open applicators and an EFD diode for fields collimated by cerrobend inserts. The charge was measured with a digital electrometer (Model 35614: Keithley Instruments, Cleveland, OH). The detector was positioned at the depth of maximum dose (R_{max}) for the field size (table 3.1) and placed at the point of maximum dose cross-plane and in-plane. The charge was collected three times for 20 monitor units (MU), for each of the diodes and ±300 V bias on the Roos chamber. The leakage current was verified to be

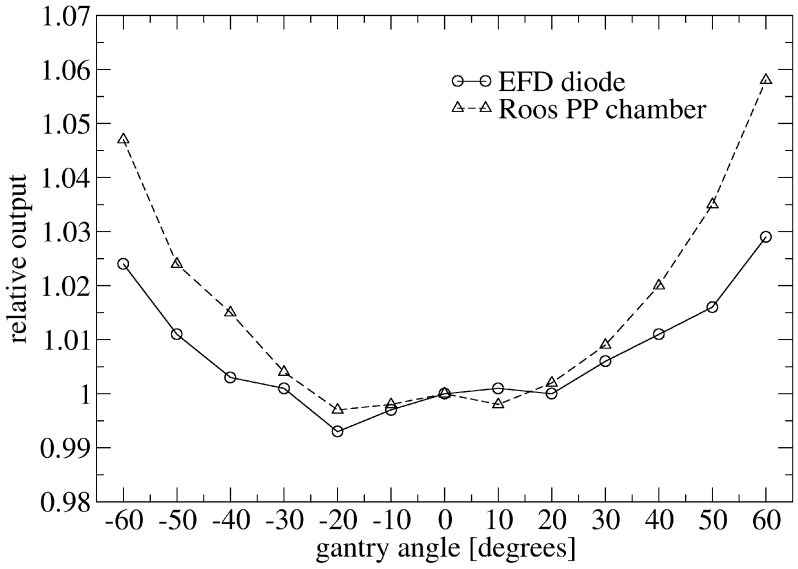

Figure 3.3 Variation in relative output with gantry rotation (detector angle) for EFD diode and Roos parallel plate chamber fixed in air at isocenter.

negligible. Since the angle of the detector relative to the incident beam can affect the measured output (Song et al. 2006), the directional (angular) dependence of the detector was also investigated. Measurements were performed in air at the isocentre with the 21 MeV electron beam and a 5 × 5 cm^2 field collimated by the jaws and a multi-leaf collimator (MLC). The output changed by less than 0.7% and 0.6% for the diode and Roos chamber, respectively, with the detector angled up to 20◦ relative to the beam axis (figure 3.3). Misalignments for the ROF measurements were much less than

these; therefore the effect of misalignment was negligible. The over-all uncertainty in electron diode measured ROF was 1%, as estimated previously by Zhang et al. (1999). Bass et al. (2009) have reported a total uncertainty of 0.6% for PTW Roos type 34001 chamber relative dose measurements which was used as the uncertainty in ROF measurements in the current work.

3.2.2 Monte Carlo Simulations

Monte Carlo simulations were performed using EGSnrc (Kawrakow and Rogers 2006) (version 1.4). BEAMnrc (Rogers et al. 1995) (version 1.104) was used to model the accelerator treatment head. Phase space data were scored at 90 cm SSD. Simulations of the final field defining aperture and water phantom dose calculations were performed in MCRTP (Faddegon et al. 1998).

Figure 3.4 shows the accelerator treatment head as modelled in BEAMnrc and MCRTP. The source and geometry details of the treatment head components from the exit window up to and including the monitor chamber were the same as used in the simulations of the treatment head for large electron fields (Faddegon et al. 2009: tables IV and II, respectively). The jaws and MLC for each applicator were set to the positions specified by the manufacturer. The source was simulated with a Gaussian energy distribution using ISOURC = 19 in BEAMnrc: a parallel circular beam with a Gaussian

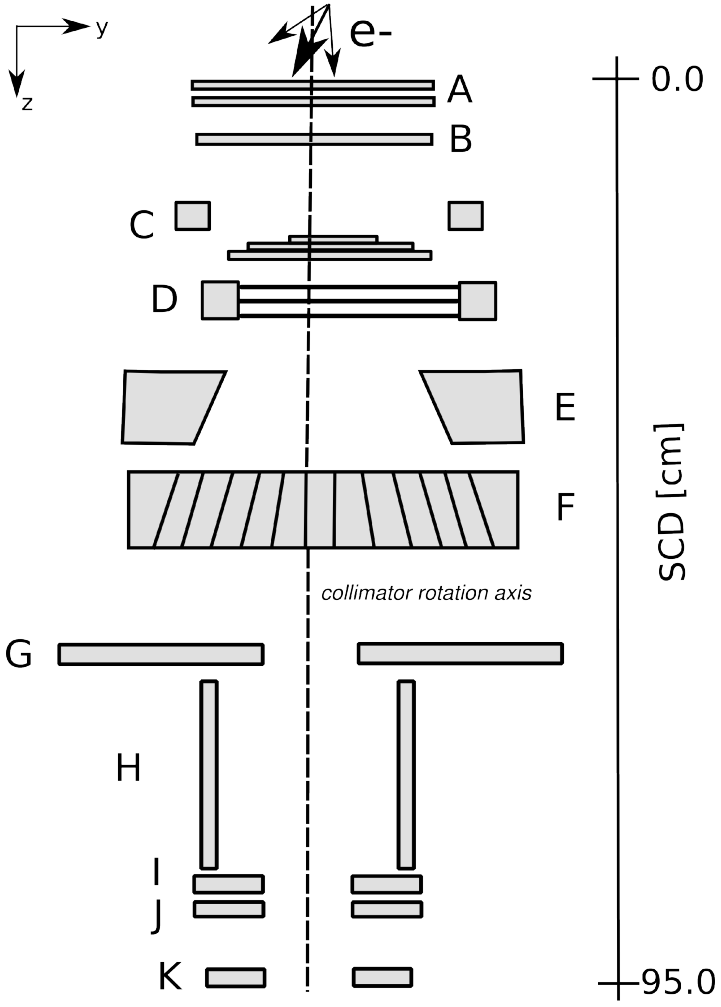

Figure 3.4 Diagram of the Siemens Oncor electron treatment head as simulated in BEAMnrc and MCRTP. A: exit window, B: primary scattering foil, C: secondary scattering foil, D: electron monitor chamber, E: jaws, F: multi-leaf collimator and applicator scrapers 1 - 5, labelled G - K, respectively. Source and geometry details (to the level of the monitor chamber (D)) were taken from previous large field simulation, without adjustment. The secondary scattering foil (C) and monitor chamber (D) were shifted off the collimator rotation axis to account for the fringe magnetic field from the bending magnet.

radial distribution (Rogers et al. 2006), modified to allow a non-zero beam angle with a Gaussian spatial distribution (Faddegon et al. 2009). Asymmetries included in the model were an incident beam angle and spot position and treatment head components offset from the collimator rotation axis.

The effect of the fringe magnetic field from the bending magnet downstream of the exit window was approximated by offsetting the secondary foil and monitor chamber from the collimator rotation axis. This offset, to compensate for the deflection of the electron beam, was different for each beam energy and was the same as used previously (Faddegon et al. 2009). Measurement of the magnetic field involved removal of the secondary scattering foil and monitor chamber. Because this procedure is impractical for clinical linacs, the simulations presented here use the method of shifting the secondary scattering foil and monitor chamber to mimic the magnetic field (Faddegon et al. 2009).

The electron applicators were modelled using manufacturer specifications, confirmed by direct calliper measurements (to be within 0.015 cm). The measurement was larger in all cases likely due to the paint on the applicator components. Cerrobend inserts were simulated incorporating the measured smaller source-to-collimator distance (SCD) of 0.56 cm and 1.14 cm relative to the applicator distal scraper, for the inserts placed in the 10×10 cm^2 applicator and the larger applicators, respectively. The

inserts were simulated with a thickness of 1.3 cm. Cerrobend (50% bismuth, 26.7% lead, 13.3% tin and 10% cadmium) was simulated using a density of 9.38 g cm^{-3}. The circular apertures were modelled in MCRTP using a piecewise linear curve of 48 equal-size line segments.

The distal scraper bar of the applicator is made of brass and has rounded corners. To calculate diagonal profiles for the 25 × 25 cm^2 applicator, the corners were fully modelled in MCRTP. The brass scraper was simulated with a density of 8.50 g cm^{-3} and a total of 36 points were used to define the aperture.

EGSnrc transport parameters used included electron lower energy cut-off (ECUT/AE) and photon lower energy cut-off (PCUT/AP) values of 0.7 MeV and 0.01 MeV, respectively. The EXACT boundary-crossing algorithm was used in BEAMnrc. PRESTA-I was used in MCRTP. The electron step algorithm was PRESTA-II. The default maximum step size (SMAX) of 5 cm was used. The maximum fractional energy loss per step (ESTEPE) was set to 0.25. Preprocessor for EGS (PEGS) data were consistent with ICRU 37 (ICRU Report No 37 1984).

800 million incident source electrons were tracked achieving close to 1% uncertainty in subsequent dose calculations in most cases. Dose-to-water was scored in a phantom containing 1.0 × 1.0 × 1.0 mm^3 voxels for fields 10 × 10 cm^2 or smaller. A phantom with 2.0 × 2.0 × 1.0 mm^3 voxels was used for larger fields. Calculated dose

distributions were compared to the measurement with arbitrary normalization as the beam current was not measured.

The output of a linac is affected by backscatter from the jaws towards the monitor chamber since the set number of MU, on certain linac models, is reached in a shorter time interval as the field size decreases (Popescu et al. 2005). Simulations showed that the contribution of backscatter in the current study was negligible; therefore the calculated ROF did not include a correction for backscatter. The Siemens electron monitor chamber comprises thin gold conductive electrodes affixed to insulating polyimide with an outer steel casing. It is positioned approximately 11 cm downstream of the exit window and 8 cm above the secondary collimators (jaws). The largest amounts of backscatter in the simulations were with the 10×10 cm^2 applicator, and were 0.5% at 6 MeV and 0.3% at 21 MeV. With the largest applicator (25×25 cm^2), the contributions of backscatter fell to 0.2% at 6 MeV and 0.1% at 21 MeV. These calculated changes in backscatter of 0.2–0.3% were within the total estimated uncertainty of electron diode measured ROF (1%) and were therefore disregarded when comparing the calculated and measured ROF.

3.3 RESULTS

3.3.1 Percentage Depth Dose Curves

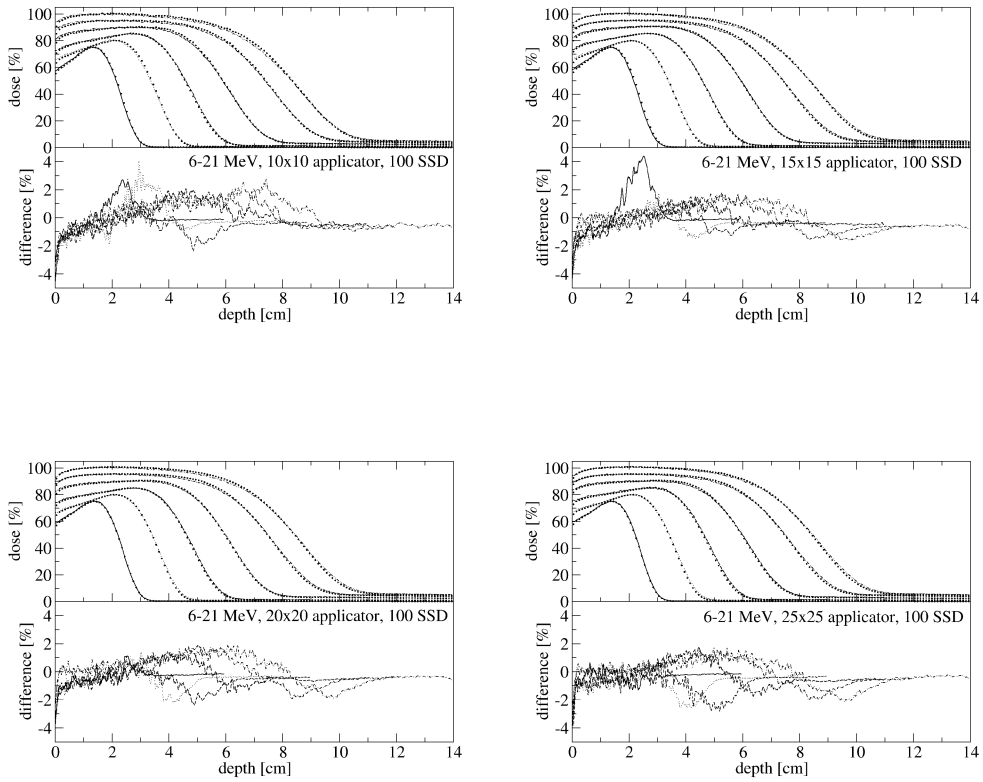

Figure 3.5 Percentage depth dose curves for 6 MeV – 21 MeV electron beams (left to right) and open 10x10 cm², 15x15 cm², 20x20 cm² and 25x25 cm² applicators. Monte Carlo calculations (points) compared with diode measurements (lines). Percentage depth dose curves have arbitrary normalisation.

PDD curves are shown in figure 3.5 for the 6–21 MeV electron beams and open applicators at a 100 cm SSD. For lower energy (6 – 15 MeV) beams, Monte Carlo calculations and measurements agreed within 1%. For higher energy beams, differences of up to 2% were seen in the depth range R_{max}–R_{50}, similar to those observed previously for open fields (Faddegon et al. 2009). The distance to agreement (DTA) between the Monte Carlo calculated and measured PDD was within 0.7 mm in all cases. The diode over-response to bremsstrahlung x-rays was seen in the tail of the PDD curves, particularly apparent for the higher energy (15–21 MeV) beams, resulting in a measured dose up to 10% higher than Monte Carlo calculations.

Measured and simulated PDD curves for the 5 cm applicator and 1–5 cm inserts in the 10 × 10 cm^2 applicator at a 100 cm SSD are shown in figure 3.6. Dose differences were within 1.5%, with the Monte Carlo calculated and diode measured DTA within 1.2 mm. The level of agreement between the Monte Carlo calculated and measured PDD was representative of that of the inserts placed in each of the three larger square applicators. For the lower energy (6–12 MeV) beams, the calculated PDD fell off less rapidly than measurements, whereas for higher energies the opposite trend was seen. For the 120 cm SSD, measurements and simulation agreed to 2%/0.9 mm. Therefore, Monte Carlo calculations accurately simulated the variable electron scattering effects of the extended SSD on the PDD curves, consistent with the results reported by Das et al. (1995).

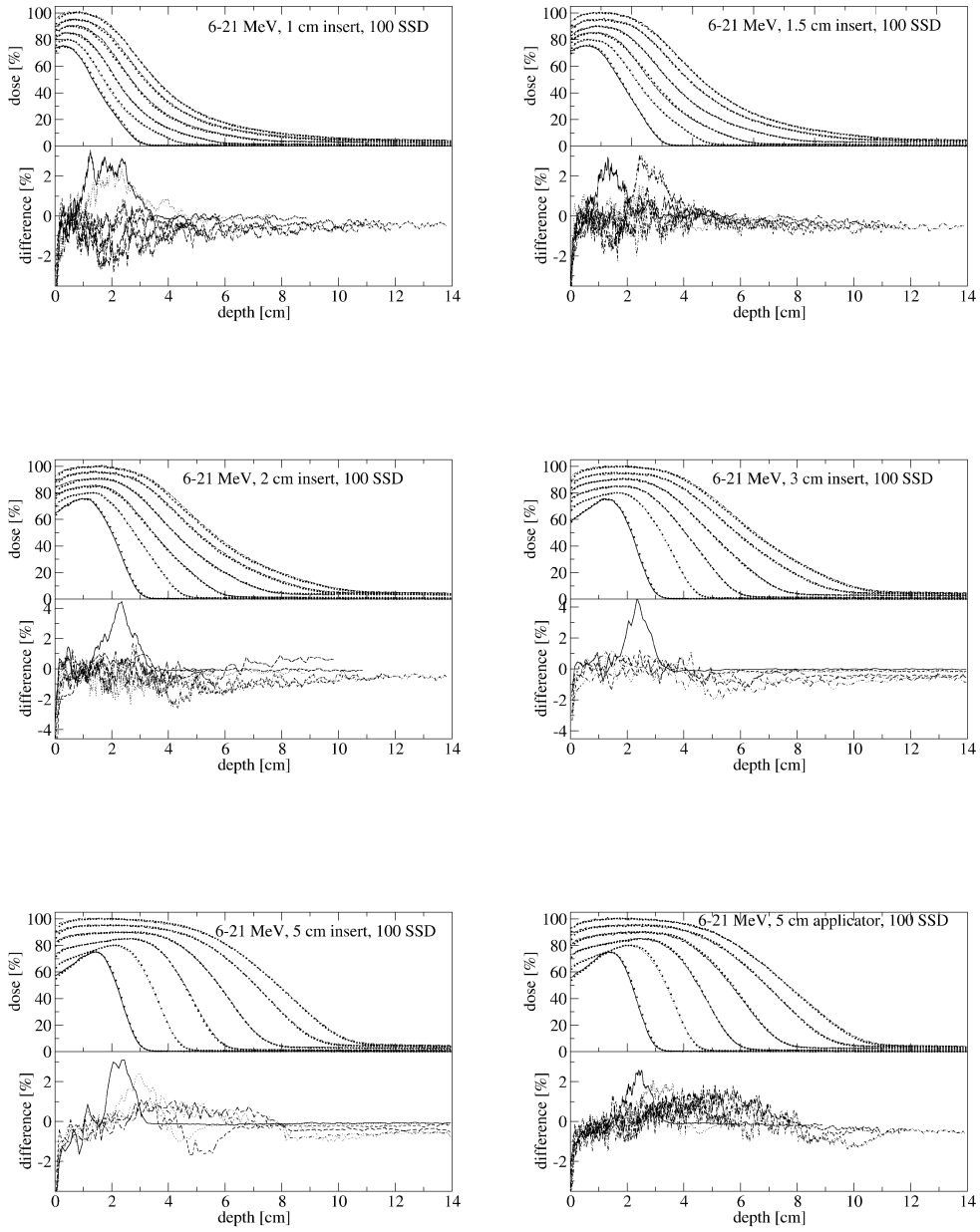

Figure 3.6 Comparison of diode (lines) measured and Monte Carlo (points) calculated percentage depth dose curves for insert collimated fields. Data have arbitrary normalisation.

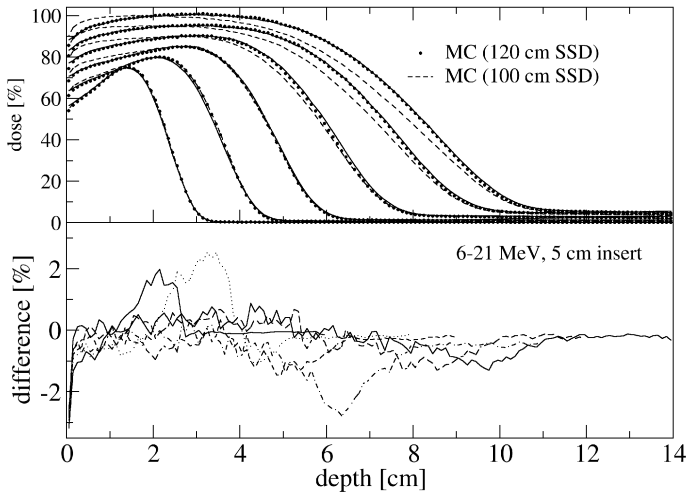

Figure 3.7 Comparison of diode measured and Monte Carlo calculated percentage depth dose (PDD) curves for 6 MeV – 21 MeV (left to right) electron beams and 5 cm diameter insert placed in the 10x10 cm^2 applicator and 120 cm SSD. The Monte Carlo calculated PDD curve at 100 cm SSD has been included for comparison. Monte Carlo calculations accurately simulate the changes to the PDD curve at extended treatment distance. Percentage depth dose curves have arbitrary normalisation.

The PDD curves for the 5 cm insert placed in the 10 × 10 cm^2 applicator and 120 cm SSD are presented in figure 3.7. The figure also includes the Monte Carlo calculated PDD curves at 100 cm SSD, for comparison. For the 6–12 MeV beams, minimal effects were observed when the SSD was changed from 100 to 120 cm. The dose in the build-up region was reduced by 3% or less. For the higher energy beams,

the extended SSD resulted in more dramatic effects on the PDD. The dose in the build-up region was reduced by up to 5% while R_{80} (the depth at which the dose falls to 80% of its maximum) and R_{50} were increased by up to 4.3 mm and 3.0 mm, respectively. For inserts 2 cm in diameter and smaller (not shown) all PDD curves were significantly altered by the increase in the SSD. For the 6 MeV beam and 1 cm diameter insert, for example, R_{80} and R_{50} increased by 7.6 mm and 6.4 mm, respectively (at the 120 cm SSD). R_{80} and R_{50} increased by 6.0 mm and 10.1 mm, respectively, for the 21 MeV beam and same circular insert. Monte Carlo calculations and measurements were in good agreement to within 1.5%/0.6 mm in all cases.

3.3.2 Dose Profiles

Dose profiles for electron beams collimated by cerrobend inserts placed in the 10 × 10 cm^2 applicator at a 100 cm SSD are shown in figure 3.8. Monte Carlo simulations and diode measurements agreed to within 1.0 mm in the high dose gradient region or 1% in the low dose gradient. The noticeable asymmetry (1.4%) in the dose profile for the 21 MeV electron beam and the 5 cm diameter insert was matched by Monte Carlo simulation to within 1%. The distances from the 20 to 80% dose lines for the 1 cm diameter insert were 7.0 mm and 4.4 mm for the 6 MeV and 21 MeV electron beams, respectively. The match between measurement and simulation in the penumbra

(generally 0.5 mm) shows that the diode had the required spatial resolution to perform accurate profile measurements in these small fields.

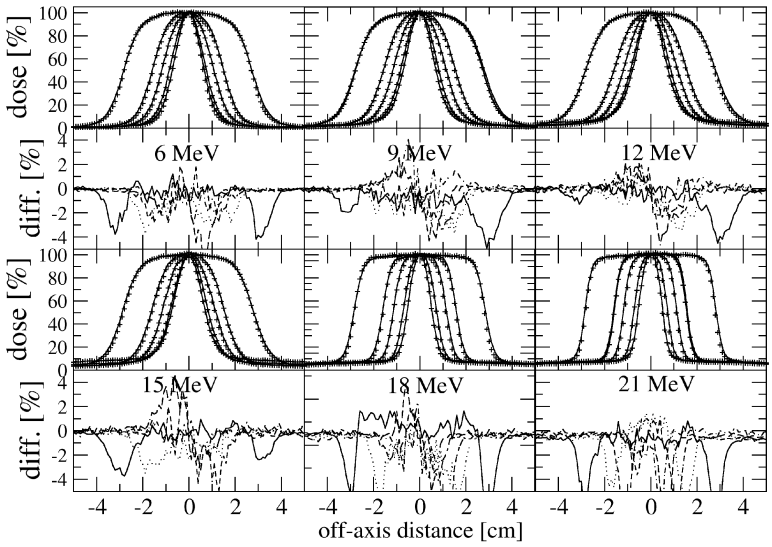

Figure 3.8 Cross-plane profiles for 1 cm, 1.5 cm, 2 cm, 3 cm and 5 cm diameters inserts. 6 MeV, 9 MeV and 12 MeV (top row left to right). 15 MeV, 18 MeV and 21 MeV (lower row left to right). Monte Carlo calculations (points) are compared with diode measurements (lines).

Figure 3.9 displays the measured and calculated cross-plane dose profiles for 6–21 MeV beams and 1 cm insert in the 10 × 10 cm^2 applicator at a 120 cm SSD, normalised to 100% on the central axis. The profiles are compared in terms of the difference in dose (%) and distance to agreement (DTA, mm) in the lower row of figure

3.9. The measured and calculated profiles agreed to 1% or 1.0 mm for 9–21 MeV beams and 1.4 mm for 6 MeV. Differences in the relative dose of up to 3% were seen in much of the profile due to high dose gradients; however the DTA was within the stated values. In the low dose gradient region of the profiles, noise resulted in divergence of the DTA.

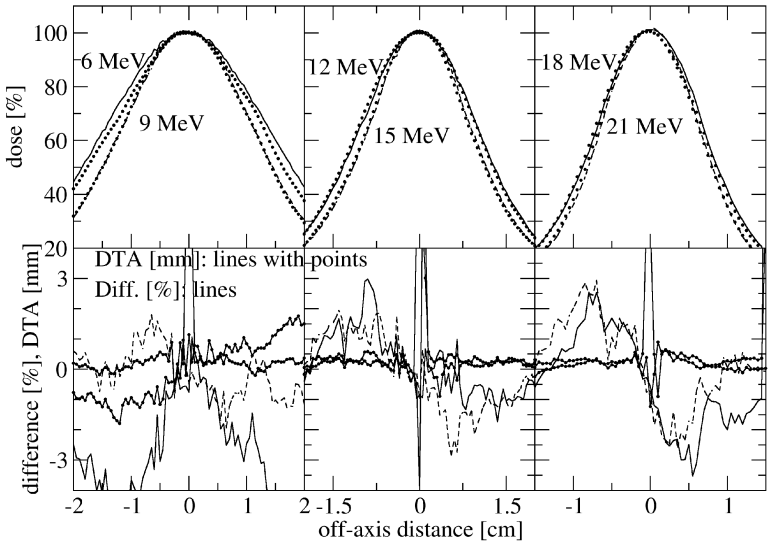

Figure 3.9 Cross-plane profiles for 1 cm diameter insert, 6-21 MeV electron beams and 120 cm SSD (upper row): Monte Carlo simulations (points) and diode measurements (lines). The lower row displays the percentage difference and distance to agreement (mm) between simulation and measurement (note the different vertical scales).

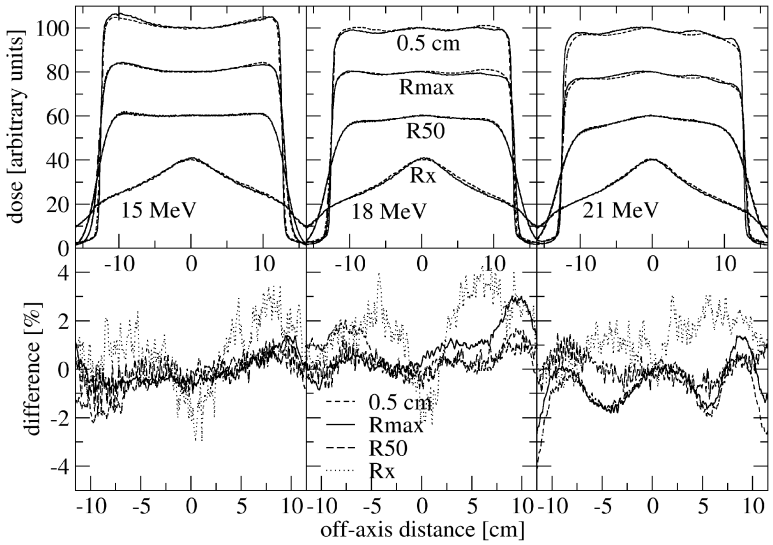

Figure 3.10 CC13 thimble chamber (measured) and Monte Carlo (calculated) in-plane profiles at depths of 0.5 cm, Rmax, in the fall-off and Rx for the 15 MeV, 18 MeV and 21 MeV (from left to right) beams and 25x25 cm^2 applicator. Dose profiles have arbitrary normalistion. Differences approaching 3% are seen in Rmax dose profiles.

The measured and Monte Carlo calculated dose profiles for open applicator defined fields generally agreed to 2.2%/1.0 mm at the 100 cm SSD with some exceptions reported below. At the extended SSD (120 cm), dose profiles showed agreement of 2.3%/1.4 mm. In-plane profiles (at depths: 0.5 cm, R_{max}, R_{50} and R_x) for the 25 × 25 cm^2 applicator and three highest energies (15–21 MeV) are presented in figure 3.10. Monte Carlo calculations are compared with thimble chamber (CC13)

measurements. The percentage difference in dose in the central region of the profiles is highlighted. The calculated profiles at 0.5 cm and R_{50} were within 2% of thimble chamber measurements. The measured and calculated R_{max} profiles for 15 and 21 MeV also agreed to 2%. For 18 MeV, however, differences of up to 2.8% were seen in the low dose gradient region. There is a mismatch in the 'undulations' in the flat region of the profile. In the bremsstrahlung tail (R_x), Monte Carlo calculations were within 4% of measurements.

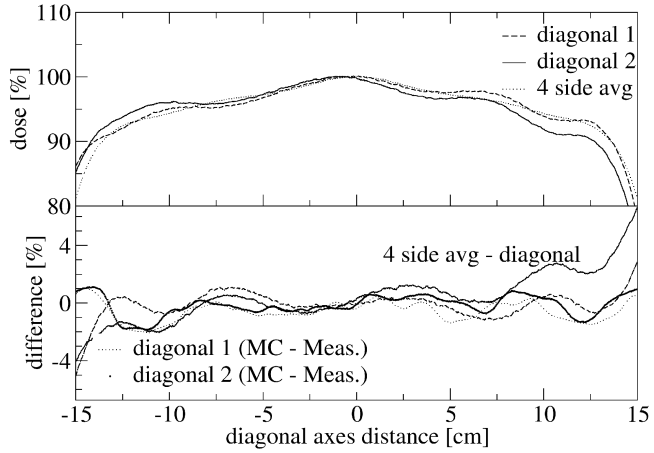

Figure 3.11 Comparison of CC13 measured diagonal profiles and CC13 measured profile averaged over the 4 quadrants. The percentage difference between the 4 quadrant averaged profile and each diagonal profile is shown in the lower row demonstrating the magnitude of asymmetry. The difference between simulation and measurement is less than the asymmetry in the profiles.

Profiles measured along the diagonal axes of the 25 × 25 cm cm^2 applicator for the 21 MeV beam are shown in figure 3.11. The figure also includes a comparison between the measured diagonal profiles and the measured diagonals averaged over the four quadrants. The profiles were asymmetric by up to 5%. Monte Carlo simulations and measurement were within 3% along both diagonals, which is less than the asymmetry in the profiles. The match at the field edge was 1.5 mm or better.

3.3.3 Relative Output Factors

ROF were measured and calculated at the R_{max} depths listed in table 3.1. Results for open applicators are presented in table 3.2. The output for the large electron field (40 × 40 cm^2) with no applicator has been included. Calculated ROFs for the open applicators were within 1% of those measured with the Roos parallel plate chamber. Table 3.2 also includes a comparison of the Monte Carlo calculated and EFD diode measured ROF. In this case calculations were within 2% of measurements. For the 6 MeV electron beam, Monte Carlo calculations follow the same trend as in the measured ROF of initially increasing up to the intermediate applicator size and decreasing for larger applicators.

The Monte Carlo calculated and measured (EFD diode) ROF for 1–5 cm diameter inserts placed in the 10 × 10 cm^2 applicator are presented in figure 3.12. The Monte Carlo calculated ROF and percentage differences to the measurement for the full

Table 3.2 Monte Carlo calculated and measured ROF for the open applicators and the 40 × 40 cm^2 field without applicator, relative to the 10 × 10 cm^2 applicator.

Field size (cm^2)	Energy (MeV)	MC ROF	% Difference MC - Diode	% Difference MC - Roos
5 cm dia	6	0.798	-0.4	-
	9	0.902	0.7	-
	12	0.927	-0.3	-
	15	0.956	0.7	-
	18	0.983	1.5	-
	21	0.993	1.2	-
15x15	6	1.023	1.4	0.9
	9	1.001	1.2	0.9
	12	0.991	0.7	0.6
	15	0.996	0.8	0.2
	18	0.990	0.2	0.2
	21	0.991	1.2	0.8
20x20	6	1.032	1.8	0.7
	9	0.976	0.7	0.0
	12	0.956	0.5	0.3
	15	0.956	0.2	-0.6
	18	0.957	0.6	-0.1
	21	0.954	1.4	0.7
25x25	6	1.005	1.3	-0.4
	9	0.959	0.3	-0.6
	12	0.947	1.3	-0.2
	15	0.954	0.7	-0.6
	18	0.950	0.7	-0.5
	21	0.946	1.4	0.5
40x40	6	0.952	0.6	-1.6
	9	0.911	0.4	-1.2
	12	0.912	1.5	-0.2
	15	0.917	1.2	-0.7
	18	0.899	0.6	-1.2
	21	0.901	1.9	0.3

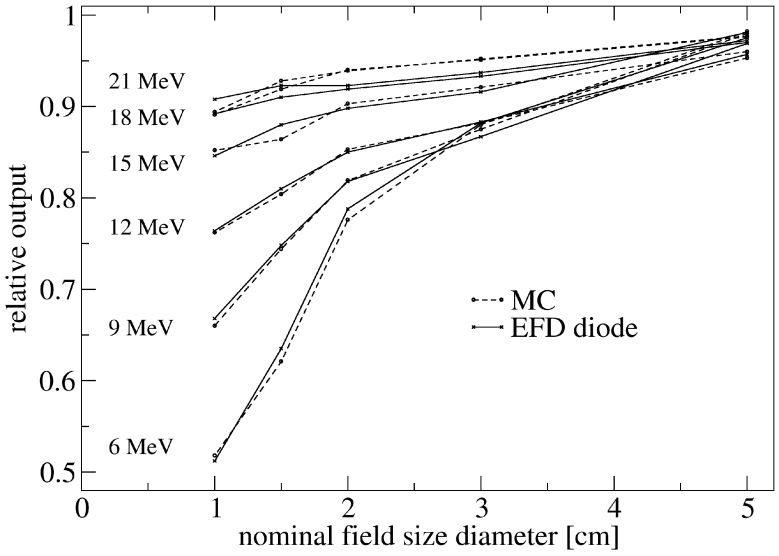

Figure 3.12 Comparison of electron diode measured (solid lines) and Monte Carlo calculated (dashed lines) relative output factors (ROF) for circular cerrobend fields 1 cm, 1.5 cm, 2 cm, 3 cm and 5 cm in diameter placed in the 10×10 cm^2 applicator and 6-21 MeV electron beams. ROF are calculated relative to the open 10×10 cm^2 applicator. (Monte Carlo calculated ROF and difference to measurement for full set of applicators are presented in table 3.3).

set of applicators are tabulated in table 3.3. ROF were calculated relative to each open applicator. Differences between the measurement and calculations were within 2.2% for field sizes over 1 cm diameter. Agreement was within 3% for the 1 cm diameter fields with several exceptions. The largest difference of 4.9% was for the 9 MeV beam with 1

Table 3.3 Comparison of Monte Carlo calculated and electron diode measured ROF for 1–5 cm diameter cerrobend inserts in the square applicator (relative to each open applicator) and the extended SSD of 120 cm for inserts in the 10 × 10 cm² applicator (relative to the 100 cm SSD). Monte Carlo calculated ROF with a percentage difference (Monte Carlo – EFD diode) in italics.

Insert size (cm)	Energy (MeV)	10x10 (cm^2)		15x15 (cm^2)		20x20 (cm^2)		25x25 (cm^2)		120 SSD	
5 cm	6	0.982	*0.8*	0.990	*1.1*	0.986	*0.9*	1.001	*0.4*	0.535	*1.0*
	9	0.980	*1.1*	0.980	*0.3*	0.985	*0.1*	0.996	*0.5*	0.588	*1.2*
	12	0.953	*-0.5*	0.970	*0.4*	0.980	*-0.2*	1.004	*1.7*	0.599	*0.6*
	15	0.960	*-2.2*	0.965	*-0.8*	0.967	*-1.6*	0.981	*1.3*	0.604	*0.1*
	18	0.977	*0.8*	0.967	*-0.5*	0.993	*-0.1*	0.996	*0.6*	0.613	*1.9*
	21	0.976	*0.4*	0.984	*0.7*	1.002	*0.6*	1.020	*0.3*	0.610	*2.0*
3 cm	6	0.880	*-0.2*	0.887	*-1.1*	0.891	*-0.1*	0.897	*0.9*	0.325	*1.4*
	9	0.875	*0.9*	0.882	*-0.3*	0.884	*-2.0*	0.885	*1.4*	0.422	*-0.1*
	12	0.882	*-0.1*	0.908	*0.8*	0.908	*-1.3*	0.925	*0.1*	0.490	*-0.1*
	15	0.921	*0.5*	0.932	*-0.4*	0.970	*0.9*	0.954	*1.0*	0.558	*1.2*
	18	0.952	*2.0*	0.960	*-0.2*	0.999	*0.9*	0.988	*0.1*	0.580	*1.0*
	21	0.951	*1.5*	0.972	*0.2*	0.998	*0.2*	1.006	*0.4*	0.581	*-0.3*
2 cm	6	0.776	*-1.5*	0.776	*-1.8*	0.767	*-1.9*	0.782	*1.7*	0.202	*0.7*
	9	0.819	*0.1*	0.820	*-1.1*	0.836	*-0.9*	0.829	*1.2*	0.304	*1.5*
	12	0.853	*0.4*	0.863	*0.1*	0.880	*-1.5*	0.898	*0.8*	0.389	*-0.5*
	15	0.903	*0.6*	0.908	*-0.3*	0.926	*-1.5*	0.949	*0.3*	0.469	*-0.7*
	18	0.939	*2.2*	0.945	*0.2*	0.980	*0.2*	0.983	*0.3*	0.534	*1.8*
	21	0.940	*1.8*	0.964	*0.7*	0.993	*0.5*	1.000	*0.2*	0.554	*1.9*
1.5 cm	6	0.621	*-2.1*	0.608	*-1.2*	0.599	*-0.3*	0.614	*0.1*	0.087	*0.8*
	9	0.744	*-0.5*	0.737	*-1.3*	0.743	*-1.6*	0.749	*1.0*	0.159	*0.9*
	12	0.804	*-0.8*	0.810	*-0.9*	0.826	*-1.9*	0.831	*1.5*	0.238	*1.9*
	15	0.864	*-1.8*	0.877	*-1.4*	0.914	*-0.2*	0.905	*1.4*	0.322	*0.4*
	18	0.928	*1.9*	0.919	*-1.5*	0.966	*0.4*	0.962	*0.1*	0.404	*1.9*
	21	0.919	*-0.4*	0.943	*-0.9*	0.974	*-0.7*	0.978	*1.1*	0.434	*0.4*
1 cm	6	0.518	*1.2*	0.469	*-2.1*	0.462	*-0.8*	0.472	*1.0*	0.052	*0.9*
	9	0.660	*-1.2*	0.619	*-4.9*	0.641	*-2.4*	0.637	*3.8*	0.094	*-3.3*
	12	0.762	*-0.2*	0.735	*-2.7*	0.765	*-2.0*	0.766	*2.0*	0.148	*-2.1*
	15	0.852	*0.7*	0.835	*-0.6*	0.849	*-2.2*	0.855	*2.1*	0.218	*-2.0*
	18	0.894	*0.2*	0.886	*-1.7*	0.927	*-1.0*	0.931	*0.6*	0.296	*0.1*
	21	0.891	*-1.9*	0.900	*-2.9*	0.928	*-3.0*	0.949	*2.6*	0.332	*-0.1*

cm insert in the 15 × 15 cm^2 applicator. Possible causes of this disagreement are discussed in the next section. However, a field of this size is of little clinical significance as it is severely affected by lack of lateral scatter equilibrium. A recent AAPM task group report (TG-70, Gerbi et al. 2009) did not consider electron fields smaller than 2 cm diameter. Also, the penumbra of the electron field is about 1 cm (20–80%). Therefore, a minimum field size of 3 cm diameter will cover a 1 cm lesion with a 1 cm margin for penumbra.

The effect of extended SSD on output factors was also investigated. Table 2.2 includes the Monte Carlo calculated and diode measured output factors for the cerrobend insert placed in the 10 × 10 cm^2 applicator and a SSD of 120 cm. The output was calculated relative to the open 10 × 10 cm^2 applicator at a 100 cm SSD. Monte Carlo calculations agreed with the diode measured output to within 2% for inserts of 1.5 cm diameter and larger. The 9 MeV, 1 cm diameter field ROF exhibited the largest discrepancy, with a 3.3% difference between measurement and simulations.

3.4 DISCUSSION

3.4.1 Percentage Depth Dose Curves

In this investigation, the source electron beam and treatment head geometry parameters obtained from large electron field simulations (Faddegon et al. 2009) have successfully

been used for the simulation of fields collimated by electron applicators and cerrobend inserts. The Monte Carlo calculated PDD curves are in excellent agreement with measurements (2%/1.2 mm). The agreement is comparable with that achieved for the large field-simulated and measured PDD (Faddegon et al. 2009). The applicator leads to an increased surface dose due to an increase in lower energy scattered electrons (as seen for BEAMDP (Ma and Rogers 2009) calculated spectral and angular distributions in figure 3.13). For example, the 12 MeV beam 10 × 10 cm^2 applicator PDD shows a greater than 3% increase in dose in the build-up region compared to the open field (40 × 40 cm^2) PDD. The Monte Carlo treatment head model accurately accounts for the variation in scatter with the applicators in place (figures 3.5 – 3.7).

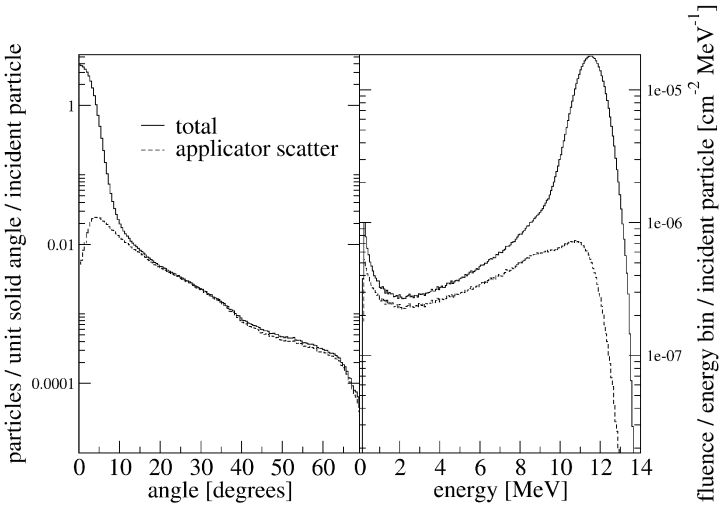

Figure 3.13 Angular and spectral distributions on a plane at 100 cm SSD for the 12 MeV electron beam and 10×10 cm^2 applicator.

Notable differences between the Monte Carlo and diode measured PDD are seen in two regions. In the depth range R_{max} to R_{50}, the difference is up to 2% for higher energy beams and lateral scatter equilibrium conditions. A similar discrepancy has been reported previously (Kapur et al. 1998, Faddegon et al. 2009). The discrepancy might be due to the depth dependence of the silicon diode (Wang and Rogers 2007) or the absence of a spectral component in the beam. In the bremsstrahlung tail, differences of up to 10% were observed (figure 3.5). The electron diode over-responds to contaminant low energy x-rays in the electron beam (Das et al. 2008). The over-response increases with energy because more contaminant x-rays are generated in the (thicker) scattering foils and water phantom.

The PDD of insert collimated fields (figure 3.6 and table 3.1) show distinct deviations from those of open applicator fields (figure 3.5) in most cases. This is likely caused by a lack of lateral scatter equilibrium encountered when the distance to any field edge (radius) is less than one-half the electron beam range (ICRU 1972). For the 5 cm diameter insert and extended SSD (120 cm), the higher energy beams (15–21 MeV) in figure 3.7 show reduced scatter from the insert, resulting in greater depth penetration (increasing by up to 3 mm), but still not as penetrating as the open applicators. The lower energy beams (6–12 MeV), with lateral scatter equilibrium and a comparable contribution of scatter at both SSDs, are less affected. Monte Carlo calculations show that scatter on the central axis decreases by 4.5% between the 100 and 120 cm SSD for

the 21 MeV beam and 1.5% for the 6 MeV beam.

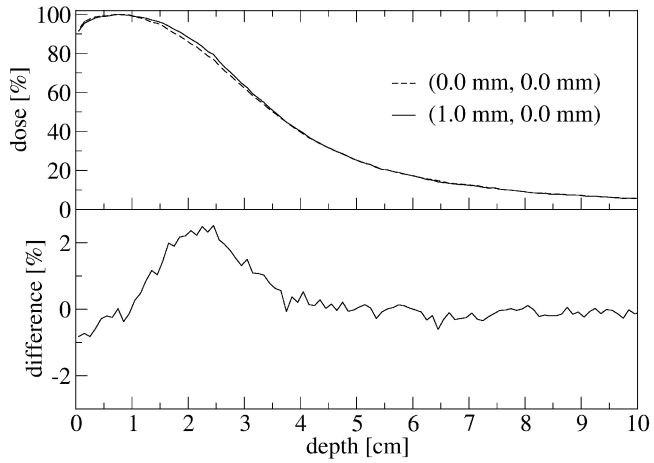

Figure 3.14 Percentage depth dose curve for 21 MeV electron beam and 1 cm diameter insert calculated with MCRTP. A 1.0 mm shift off the central axis leads to a 2% change in the (normalised) dose at R_{80}. The effect is less than 1% at R_{50}. The dose at R_{max} drops by 3.7%, of significance for relative output factor measurements.

The Monte Carlo calculated and measured PDD are in good agreement down to a field size of 1 cm diameter suggesting that any field size dependence of the diode (Wang and Rogers 2007) has little effect on the PDD for the wide range of fields in this study. Accurate positioning of the detector was important, especially for the smallest fields (collimated with cerrobend inserts) and the higher energy beams (18 MeV and 21 MeV). In this case the off-axis ratio was lower and the lateral spread of the beam was

narrower, which meant that a small shift off-axis had a greater effect on PDD measurements. Figure 3.14 shows the calculated PDD curves for the 21 MeV electron beam and 1 cm insert at a 100 cm SSD. It can be seen that a 1.0 mm shift off-axis leads to a 2% difference in the depth at which the dose falls to 80% its maximum, R_{80}. The effect at R_{50} is less than 1%. The dose at R_{max} (i.e. the normalization point) drops by 3.7%.

3.4.2 Dose Profiles

The secondary scattering foil and monitor chamber were offset from the collimator rotation axis to compensate for the fringe magnetic field from the bending magnet (Faddegon et al. 2009). However, Monte Carlo calculated dose profiles are generally in excellent agreement (1%/1 mm) with EFD diode measurements for cerrobend insert collimated fields (figures 33 and 34). These smaller fields appear to be less sensitive to details on treatment head geometry as the cerrobend inserts reduce the scatter from treatment head components upstream (Zhang et al. 1999). The EFD diode was required for accurate measurement in insert-collimated fields as field widths measured with the CC13 thimble chamber for the 1 cm diameter insert were 2.4 mm too large (figure 3.2). Detector mispositioning of ±1 mm depth led to acceptable errors of up to 0.3 mm in the penumbra (20–80%) of dose profiles, however, this may have contributed to the 1.5 mm

discrepancy for the 6 MeV beam (see figure 3.9). As the field size was increased (open applicators) details on the source and treatment head geometry became important (figure 3.10). This is consistent with previous studies (Verhaegen et al. 2001, Faddegon et al. 2005). Good agreement between Monte Carlo calculation and measurement is achieved in the 'shoulders' of large applicator profiles in the current study due to appropriate and realistic selection of the angular distribution of the source electron beams (0–0.8°) and an accurately modelled exit window (0.05 cm thicker than manufacturer specification) and foil geometries, based on previous work (cf Faddegon et al. 2009: tables II and IV).

Differences of up to 3% are seen in the flat region of in-plane dose profiles for the higher energies and largest applicator (figure 3.10). This can be explained by the fringe magnetic field from the bending magnet. The field has a magnitude large enough (up to 0.02 T for 21 MeV) to deflect each electron beam off-axis by almost 1 cm at the isocentre (Faddegon et al. 2009). The variable secondary scattering foil thickness causes the undulations seen in the dose profiles for the higher energy (18 and 21 MeV) beams (figure 3.10). This foil was shifted off-axis to match the asymmetry of the measured large field profiles (Faddegon et al. 2009). However, there is a mismatch in the undulations without the simulation of the magnetic field. Figure 3.15 shows the in-plane R_{max} profile for the 21 MeV electron beam and 25 × 25 cm^2 applicator. In this figure the Monte Carlo calculated profile has been shifted negative in-plane so that

undulations caused by the secondary foil align better; however, the field edges (which are affected by the monitor chamber lateral offset) no longer match. With the magnetic field included in EGSnrc simulations (cf. Bielajew 1993) and the secondary foil and monitor chamber fixed in position, the undulations in the dose profiles are expected to align better with measurements.

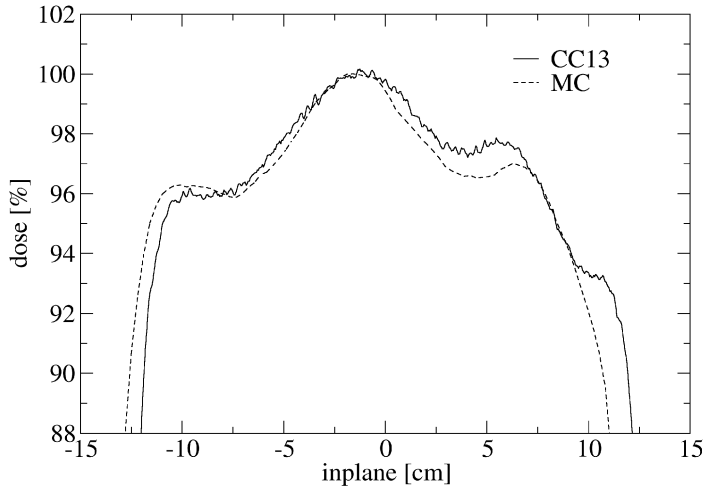

Figure 3.15 Inplane R_{max} profile for the 21 MeV electron beam and 25×25 cm^2 applicator. The Monte Carlo calculated profile has been shifted negative in-plane so that the undulations in the profile (due to the 3 stepped layers of the secondary scattering foil) better align. The secondary foil and monitor chamber were offset from the collimator rotation axis in simulations to compensate for a magnetic field downstream of the exit window.

3.4.3 Relative Output Factors

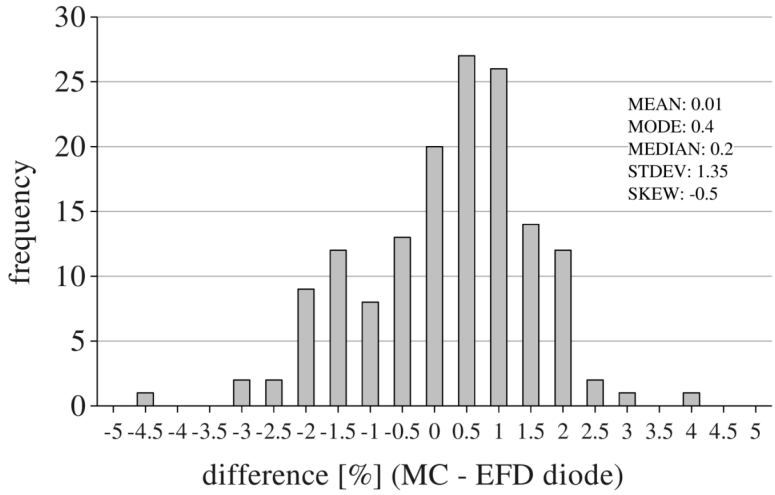

Figure 3.16 Histogram of percentage differences between Monte Carlo calculated and EFD diode measured relative output factors for cerrobend insert collimated fields (table 3.3).

Monte Carlo calculated and measured ROF are in good agreement for large (40 × 40 cm^2), open applicator and cerrobend insert collimated fields. Limiting the comparison to fields of clinical relevance (3 cm diameter and larger), the data show 2% agreement (tables 3.2 and 3.3). Roos chamber measurements agree better with Monte Carlo calculations than EFD diode measurements for larger fields (table 3.2). The Roos chamber is a precision detector used for absolute dosimetry and has a lower uncertainty than the diode for relative dose measurements (Bass et al. 2009). The inadequate spatial resolution of the larger ionization chambers (figure 3.2) meant that the EFD diode was required for ROF measurements in cerrobend insert collimated fields. However, the

diode exhibits a number of disadvantages for electron beam dosimetry (Song et al. 2006).

The uncertainty in the EFD diode ROF was a factor of 1.7 higher than that of the Roos chamber. Figure 3.16 shows the histogram of percentage differences between the Monte Carlo calculated and measured ROF for the insert collimated fields in table 3.3. The mean difference is 0.01% with a standard deviation of 1.35%. The data have negative skew. The outliers are for the 9 MeV beam and the 1 cm insert placed in the 15 × 15 cm^2 and 25 × 25 cm^2 applicators, respectively. Detector centring error was investigated as a possible reason for these differences. The dose at R_{max} dropped by 3% with a 1 mm shift off-axis. This would reduce the difference (Monte Carlo – EFD diode) to about 1% for the 1 cm insert/25 × 25 cm^2 applicator case; however, it is unlikely the detector was off-centre by this amount. The 1 cm diameter insert also generates a sharp R_{max} point. A detector depth mispositioning error of 1 mm would lead to up to 1% reduction in dose for the 9 MeV electron beam, 1 cm insert/15 × 15 cm^2 applicator case. Since the water surface is defined by the reflection method, detector positioning errors in the depth direction are more likely than errors in the cross-plane/in-plane positioning. Other possible reasons related to measurement error include the angular dependence of the diode (Song et al. 2006) or the field size dependence of the diode response (Wang and Rogers 2007), which have not been ruled out for such a small field size. Adequate histories were simulated in the Monte Carlo model, with a

statistical uncertainty of 1% in the dose scored in a 2 mm^3 region at R_{max}, so this does not appear to be the cause in this case.

For the lowest energy beam (6 MeV), the same trend of ROF initially increasing up to the intermediate applicator size and then decreasing for larger applicators is seen in both measurements and calculations. Larger applicators use larger secondary collimator settings. The trend is attributed to a trade-off with increasing field size, in increased scatter from the fixed components and decreasing scatter from the secondary collimators and applicator (Kapur et al. 1998). Figure 1.15 shows the BEAMDP-calculated spectral distributions of electrons last scattered from fixed components (labelled direct electrons) and scattered from the jaws, MLC and applicator scrapers (labelled scatter electrons) for the 6 MeV beam and open applicators. Spectral distributions have been normalised to the peak of the total spectral distribution, which included both direct and scattered electrons. A decrease in scatter contribution from the jaws, MLC and applicator and an increase in direct contribution from fixed components with increasing field size are observed. As the field size is first increased from small values, the dose from the direct components of the beam increases while the dose from the scatter decreases. As the applicator size is further increased, the dose from the direct component reaches a plateau and the scattered component continues to decrease. Therefore the ROF is the maximum at intermediate field sizes.

While previous studies have used EGS4 Monte Carlo calculations to accurately

predict output factors (Kapur et al. 1998, Zhang et al. 1999, Verhaegen et al. 2001), they did not utilise the current methodology which incorporated simulation parameters obtained from the treatment head disassembly and direct geometry measurement (Faddegon et al. 2009). Zhang et al. (1999) performed simulations of a Siemens MD2 accelerator and calculated ROF for 6–13 MeV electron beams and square inserts down to 2×2 cm^2. While 1% agreement between the Monte Carlo calculated and measured ROF was reported, it was concluded that cut-out (insert) factors were not as sensitive to the accelerator model as (open) applicator factors. The current study has shown that all ROF are relatively insensitive to details of the treatment head model, considering the excellent match between measurements and simulations achieved while using unrealistic secondary scattering foil and monitor chamber lateral offsets. Verhaegen et al. (2001) reported 2% agreement in ROF for a Varian Clinac 2100C linac model. However, discrepancies were found in the 20 MeV beam and 10×10 cm^2 field dose profile ('shoulders') of up to 4% (attributed to a possible incorrectly specified scattering foil) and ROF of up to 5%. Verhaegen et al. (2001) noted the fact that details on the linac treatment head geometry had to be obtained from the manufacturer was a potential drawback. The current work achieved 1% agreement between the Monte Carlo calculated and measured ROF for the full set of open applicators and the 40×40 cm^2 field (table 3.2), validating the source and geometry simulation parameters used. Foil geometries were taken from previous simulations (Faddegon et al. 2009). Tighter

constraints on source and geometry details, without relying on manufacturer specifications, have resulted in good agreement between the measured and Monte Carlo calculated dose distributions in this study.

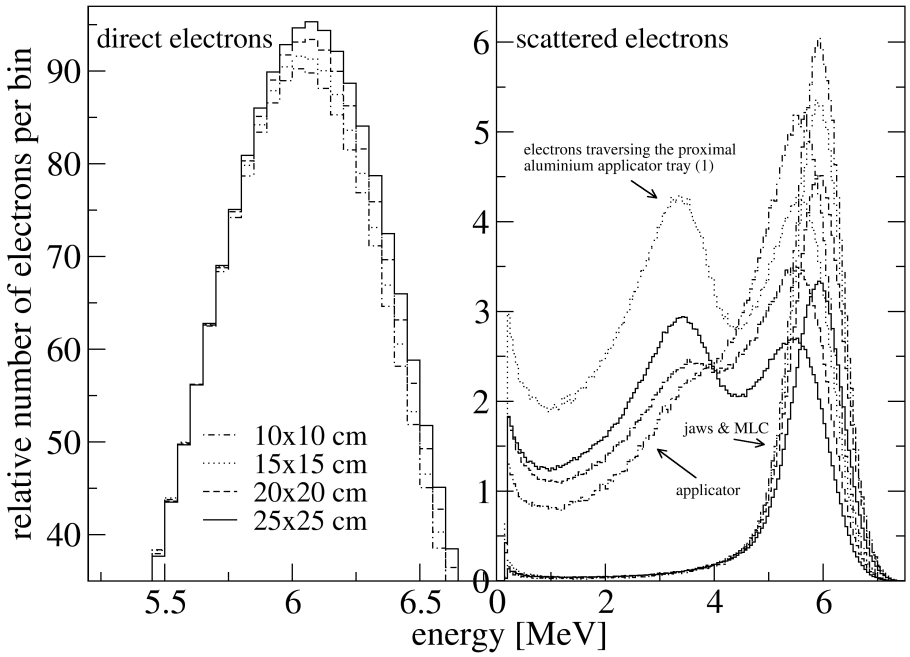

Figure 3.17 Spectral distributions of direct electrons (from fixed components) and scattered electrons (from jaw, MLC and applicator) calculated on a plane at 100 cm SSD for 6 MeV and 10×10 cm^2 (dash-dot line), 15×15 cm^2 (dot line), 20×20 cm^2 (dashed line) and 25×25 cm^2 (solid line) applicators. The distributions are normalised to the peak of the total (direct + scatter) spectral distribution. A decrease in scatter component from jaws, MLC and applicator and increase in direct component with increasing field size is seen.

3.5 CONCLUSIONS

Measurements were performed on a Siemens Oncor accelerator for applicator and insert collimated fields and compared with simulations done using improved details on the source electron beam and geometry of the treatment head. The model used source and treatment head geometry parameters determined independently from a previous study of large electron fields which resulted in the most accurate large electron field simulations achieved (Faddegon et al. 2009).

Measured and calculated PDD curves agreed to 2%/1 mm or better. Calculated and diode measured dose profiles generally agreed to 1%/1 mm for insert collimated fields. For open applicator collimated fields, the measured and calculated profiles agreed to 2%/1 mm in most cases. For the largest open applicator and higher energy (18–21 MeV) beams, differences of up to 3% were observed between the thimble chamber-measured and Monte Carlo calculated profiles at the depth of dose maximum.

Monte Carlo calculated ROF were within 1% of parallel plate chamber measurements for open applicator fields. For insert collimated fields, the diode measured and Monte Carlo calculated output agreed to 2 ± 1% for fields of 1.5 cm diameter or larger.

A magnetic field downstream of the exit window was not modelled in this study. The secondary scattering foil and monitor chamber were offset from the collimator

rotation axis to account for the electron beam deflection. This led to a mismatch in the undulations of the dose profiles of the largest applicator and higher energy (18–21 MeV) beams, resulting in the larger discrepancies between measurements and calculations. Explicit simulation of the magnetic field with a single position of the secondary scattering foil and monitor chamber is likely to improve the result.

The use of large electron fields to derive the source electron beam and treatment head geometry simulation parameters has been shown to lead to accurate simulations for the smaller applicator and insert collimated fields. The source and fixed component geometry parameters were used for smaller electron field simulations without any adjustment. The use of large electron field data to commission a set of electron beams for the full clinical range of field size and SSD is also shown to be feasible in this case.

4. Accounting for the Fringe Magnetic Field from the Bending Magnet in Treatment Head Simulation

4.1 INTRODUCTION

Large electron field, with the applicator removed and secondary collimators wide open, have been employed, in varying degrees of detail, for Monte Carlo simulation of the treatment head of linear accelerators from various manufacturers including Varian (Huang et al. 2005, Weinberg et al. 2009), Elekta (Bjork et al. 2002) and Siemens (Faddegon et al. 2005, 2008). Disassembly of a Siemens Oncor treatment head and large electron field measurements have been used further constrain source and treatment head geometry simulation parameters (Faddegon et al. 2009) and these parameters were used to commission a treatment head model for clinically relevant fields (chapter 3). In the work of Faddegon et al. (2009), a fringe magnetic field from the bending magnet downstream of the exit window (with magnitude up to 0.02 T) was found to result in the displacement the electron beams by up to 0.9 cm at the machine isocentre. The secondary scattering foil and monitor chamber in the simulation were unrealistically laterally offset from the collimator rotation axis, to match the measurement asymmetry, without simulation of the fringe field. This study focusses on

characterising the fringe magnetic field and including the field in Monte Carlo treatment head simulations with the goal of improving the accuracy of the calculated fluence and dose distributions.

4.2 MATERIALS AND METHODS

4.2.1 Siemens Oncor Accelerator

The Siemens Oncor is a S band (2856 MHz) standing wave electron accelerator providing six clinical electron beams in the energy range 6 – 21 MeV. Megavoltage beams are produced in a horizontally mounted (copper) waveguide and a 270° bending and focusing magnet system (Oline et al. 1990) (Stangenes Industries Inc, Palo Alto, CA) is employed to transport the electron beam into the treatment head. This magnet consists of two low carbon steel pole pieces fitted with two "D" shaped electromagnets. The vacuum envelope occupies a 1.78 cm gap between the poles and acts as a ± 7% width energy filter. The envelope mean radius is approximately 6 cm, requiring a field of over 1 T to bend the highest energy beam onto the exit window. Each pole face can be divided into 5 regions (figure 4.1): (1) the entrance pole face edge, (2) constant field region, (3) focusing gradient region, (4) constant field region and (5) exit pole face edge. The entrance and exit pole faces are angled and have extended fringe fields which are important in beam focusing.

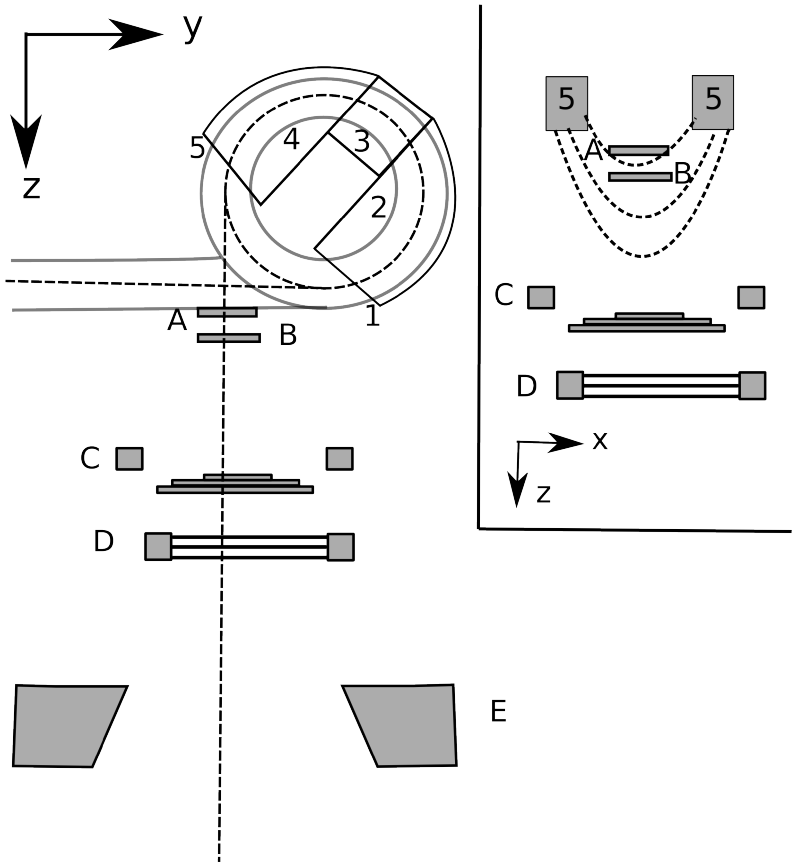

Figure 4.1 Diagram of Siemens Oncor 270° bending magnet and electron treatment head. The bending magnet is composed of 5 distinct regions: (1) entrance pole face edge, (2) constant field region, (3) focusing gradient region. (4) constant field region and (5) exit pole face edge. The exit pole face is angled and has an extended fringe field to focus the beam. The key components of the treatment head modelled in BEAMnrc are also shown in this diagram: the exit window (A), primary scattering foil (B), secondary scattering foil (C), electron monitor chamber (D) and secondary collimators (E). The inset figure demonstrates how the fringe field extends below the exit window modifying the electron beam characteristics after it has exited the envelope.

After transport through the magnet, the electron beam enters the treatment head through a water-cooled titanium exit window. The inplane position of the electron spot on the exit window (spot offset, $x_{S,Y}$) is controlled via two orthogonal dipoles surrounding the waveguide. The current in these steering coils is preset for each beam energy to centralize the electron beam on the exit window and to optimize beam uniformity (which is monitored downstream by the electron monitor chamber). The internal machine parameter defining the current flowing through these coils is called STCI and is given in milliamperes (STCI $\approx$ 900 mA for the nominal 21 MeV beam). Faddegon et al. (2009) showed the steering coils on the waveguide move the beam ($x_{S,Y}$) inplane 0.1 – 0.2 cm per ampere. In addition, adjusting the beam energy shifts the spot position at the exit window in the inplane direction.

After entering the treatment head, the beam is scattered by primary and secondary scattering foils before traversing a monitor ionisation chamber. The primary foil is enclosed in a brass holder with a stainless steel retainer. The wall of the monitor chamber collimates the beam to a 36 cm diameter field size at isocenter. For the largest field (40×40 cm^2) with no applicator, the positions of the field edges are determined by the lateral position of the monitor chamber. The lateral position of the aluminium secondary scattering foil is a critical component in determining the flatness and symmetry of the electron beam. The fringe magnetic field extends into the space between the exit window and monitor chamber, also modifying the spatial and angular

characteristics of the beam.

4.2.2 Measurements

4.2.2.1 Water Tank Scans

Measured dose profiles and percentage depth dose curves used in this study have been reported previously (Faddegon et al. 2009). Measurements were taken on a Siemens Oncor linac for 6 – 21 MeV electron beams and 3 different treatment head configurations: (1) exit window only in the beam, (2) primary foil added and finally (3) full clinical head with the secondary foil and monitor chamber in the beam line (figure 4.1). The applicator was removed and jaws and MLC set to maximum (40×40 cm^2) field size for all configurations with a source-to-surface distance (SSD) of 100 cm. Dose profiles were measured with a CC13 (Scanditronix–Wellhöfer, Uppsala, Sweden) thimble ionization chamber centered on the collimator rotation axis. Profiles were measured at the depth of dose maximum, R_{max}, and in the bremsstrahlung tail, R_x. Percentage depth ionization was measured with a Roos parallel plate chamber (N34401, PTW, Freiberg, Germany) with an effective point of measurement (EPOM) of 0.115 cm, and percentage depth dose with an EFD diode (Scanditronix–Wellhöfer, Uppsala, Sweden) with 0.045 cm EPOM correction. The lateral offset of the secondary scattering foil and electron monitor chamber, from the collimator rotation axis, was estimated from digital photographs. The uncertainty in the offsets was estimated as ±

0.03 cm. These positions were used for quality control and to guide selection of simulation offsets.

4.2.2.2 Magnetic Field Measurements

With the linac in electron mode, the monitor chamber and secondary scattering foil were removed to allow access to the region below the exit window. The bending magnet was energized with currents of 13.1 – 42.2 A which covered the nominal energy acceptance range of 6 – 21 MeV. The magnetic field below the exit window was measured with a Tesla meter (F.W. Bell model 4048, Milwaukie, OR). The meter had a resolution of 0.01×10^{-3} T and an accuracy specification of ± 2%. The Hall probe had dimensions: 0.419 cm × 0.145 cm × 6.35 cm. With the bending magnet energized, the probe flat was aligned with the north magnetic field which entered from the positive crossplane (perpendicular to the electron gun) direction. Measurements were taken 12 cm along the central axis and up to 3 cm off-axis at 1 cm intervals. There is restricted space in the treatment head such that measurements further off-axis than those reported were not possible in most cases. The estimated uncertainty in the measured magnetic field measurements was 17%. This included the accuracy specification (±2%) and estimates of positioning uncertainty (±3 mm), orientation (±5°) and reproducibility of three measurements (±8%), added in quadrature.

4.2.3 Monte Carlo Simulations

4.2.3.1 Simulation Codes

Monte Carlo treatment head simulation was performed with EGSnrc (version 1.4) (Kawrakow et al. 2006) / BEAMnrc (version 1.104) (Rogers et al. 1995) for the three different treatment head configurations outlined in section II.B.1: (1) exit window only, (2) primary foil and (3) clinical beam. Phase space data was scored at 100 cm SSD. Dose-to-water was calculated using MCRTP (Faddegon et al. 1998) with a $40 \times 40 \times 20$ cm^3 phantom containing $0.2 \times 0.2 \times 0.1$ cm^3 voxels. 800 million incident source electrons were tracked to achieve uncertainty in subsequent dose calculations of 1.0%. EGSnrc transport parameters were the same as used in the Siemens Oncor electron head simulations of detailed in chapter 3.

4.2.3.2 Incident Electron Source

The electron beam incident on the exit window was modelled using a modified BEAMnrc source developed by Faddegon et al. (2009) and was characterised by six parameters: (1) mean energy, E, (2) Gaussian energy spread, $\phi'(E)$, (3) Gaussian (spot) spatial distribution, r_S, (4) spot offset from collimator rotation axis, x_S, (5) beam angle, Θ and (6) angular divergence, $\phi'(\Theta)$. The mean energy (E) and Gaussian energy spread ($\phi'(E)$) were previously selected to match the measured depth of 50% ionization, I_{50} and

the slope of the fall-off portion of the PDI curve, respectively, with the primary foil only in the beam (Faddegon et al. 2009). The fringe magnetic field below the exit window has a negligible effect on these parameters, as demonstrated in section 4.4.3. Mean energies (E) of 6.69 MeV, 9.69 MeV, 12.38 MeV, 15.85 MeV, 19.57 MeV and 21.75 MeV were used for the nominal 6 – 21 MeV electron beam with $\phi'(E)$ of ± 7.1%, ± 4.9%, ± 6.2%, ± 6.0%, ± 4.8% and ± 3.3%, respectively, consistent with the approximate ± 7% transmission bandwidth of the vacuum envelope (Oline et al. 1990).

A Gaussian spatial distribution, r_s, of 0.2 cm was used (Huang et al. 2005, Sawkey and Faddegon 2009). Increasing the electron beam radius from 0.1 cm to 0.2 cm was previously found to have very little effect, typically below 1% (Schreiber and Faddegon 2005). Electron dose distributions are insensitive to r_s values in the realistic range of 0.1 – 0.3 cm. The spot offset (x_s) and beam angle (Θ) were previously measured (Faddegon et al. 2009). An analysis of the experimental uncertainty associated with both of these parameters was performed and each parameter was then allowed to vary within these tolerances. The experimental uncertainty in x_s was estimated to be no more than ±0.05 cm. The beam angle, which was based on the position of the peak of the profile in the bremsstrahlung tail, had larger experimental uncertainty for lower energies which generate less bremsstrahlung x-rays and therefore a less detectable peak (figure 4.2). The experimental uncertainties in the beam angles (directional cosines) were estimated as ±0.52° (0.009), ±0.34° (0.006), ±0.17° (0.003),

±0.11° (0.002), ±0.09° (0.0015) and ±0.09° (0.0015) for the nominal 6 - 21 MeV beams, respectively.

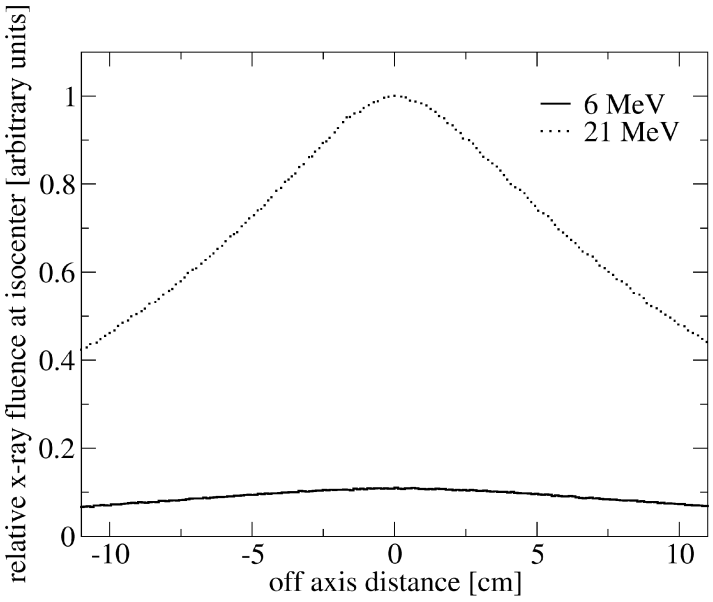

Figure 4.2 Bremsstrahlung fluence for 6 and 21 MeV electron beams normalized to the peak of the 21 MeV profile to hightlight the relatively flat 6 MeV profile which leads to a larger uncertainty in the beam angle at the exit window.

4.2.3.3 Treatment Head Simulation including Fringe Magnetic Field

An electron in a vacuum with applied magnetic field travels in a curved path dictated by the Lorentz force. The radius of curvature of the electrons path is given in equation 1.8. From this equation, the maximum fringe field magnitude measured below the exit window (0.006 - 0.020 T) would result in radius of 3.6 m for electrons with nominal

energies of 6 – 21 MeV.

Monte Carlo treatment head simulation was performed with a modified version of BEAMnrc (version 1.104), which accounted for the effect of the lateral shift of components (Faddegon et al. 2005). Electron beam transport in the presence of a magnetic field made use of the generalised *emf_macros.mortran* macro package originally developed for EGS4 (Bielajew 1993). This EMF macro has been used for various applications with magnetic fields in the range of 0.1 – 20.0 T by a number of other investigators (Bielajew 1993, Lee and Ma 2000, Li et al. 2001, Kirkby et al. 2008). Kirkby et al. (2008) showed that PENELOPE and EGSnrc dose distributions generally agreed to within statistical uncertainty (~1%) for slab phantoms with applied magnetic fields of 0.2 and 1.5 T. Simulations were performed to ensure that the code could adequately simulate electron trajectories in simple geometries with reasonable accuracy. EGSnrc was found to accurately simulate the deflection of mono-energetic pencil beams, with initial kinetic energies of 6 – 21 MeV, over 10 cm with 0.1 T applied magnetic field. EGSnrc matched the 2.45 – 0.70 cm deflection predicted using equation 1 to within 0.1 – 0.05 cm for 6 – 21 MeV, respectively.

The fringe magnetic field was simulated in BEAMnrc using a component module (CM) called RECT. This component, consisting of a rectilinear array of voxels, allowed simulation of a region dependent magnetic field in the treatment head (a different field may be specified for each voxel, with the field constant within the voxel).

The magnet field measured below the exit window (4.2.2.2) was used in the treatment head simulations. The RECT CM was positioned between the exit window and secondary scattering foil. The CM contained 1.0 cm^3 air regions, each with a corresponding magnetic field.

The offset of the (y) jaws and (x) multi-leaf collimator, from the collimator rotation axis, were estimated from the field edge of the 18 MeV beam in primary foil only configuration. Peripheral material (tungsten MLC tracks and steel support structure) below the MLC bank was previously found to significantly collimate the edge of the 6 MeV field resulting in an over-estimation of the inplane field edge by up to 1.4 cm (Faddegon et al. 2009). This material was included in the current study along with the fringe magnetic field simulation.

4.2.3.3 Sensitivity of Clinical Dose Profiles to Sources of Asymmetry

The effect of various sources of electron beam asymmetry on idealised symmetric R_{max} dose profiles was investigated by Monte Carlo simulation. The incident electron beam (spot) offset, x_S, and angle (at the exit window), Θ, were varied by the experimental uncertainties reported in section 4.2.3.2. The effect of secondary scattering foil and monitor chamber lateral offsets of 0.1 cm were also separately quantified, as well as, the effect of the (measured) fringe magnetic field. Sensitivity was quantified in terms of change in flatness ($\Delta_{Flatness}$), symmetry (Symmetry), field offset (of 50% dose points)

and slope (($D_{12cm} - D_{-12cm}$) / 24, % / cm) of line through points at +12 cm and -12 cm from the central axis. Flatness was defined as $100 \times (D_{max} - D_{min}) / (D_{max} + D_{min})$ and symmetry as the difference in dose at points +12 cm and -12 cm from the central axis ($D_{12cm} - D_{-12cm}$). The flatness of the idealized symmetric profiles ($Flat_{baseline}$) was 2.4%, 3.0% 0.35%, 1.7%, 2.8% and 6.65% for 6 – 21 MeV, respectively. The change in flatness (from baseline; $\Delta_{Flatness} = Flat_{new} - Flat_{baseline}$) was calculated and reported in the results section 4.3.4.1.

4.3 RESULTS AND DISCUSSION

4.3.1 Magnetic Field Measurements

The magnetic field at the exit window was found to increase from 0.006 T to 0.020 T with bending magnet current (beam energy), as expected, with a slope of 0.48 mT / A and intercept of -0.4 mT. The field was a maximum with the probe flat aligned with the crossplane (x) axis, perpendicular to the electron gun and along the axis of the magnet poles. It dropped to ~0 T when the probe flat was aligned with the inplane (y) axis (in the plane of the gun). This was demonstrated by fixing the Hall probe to the treatment head at isocentre, and then rotating the collimator angle through 90° (figure 4.3).

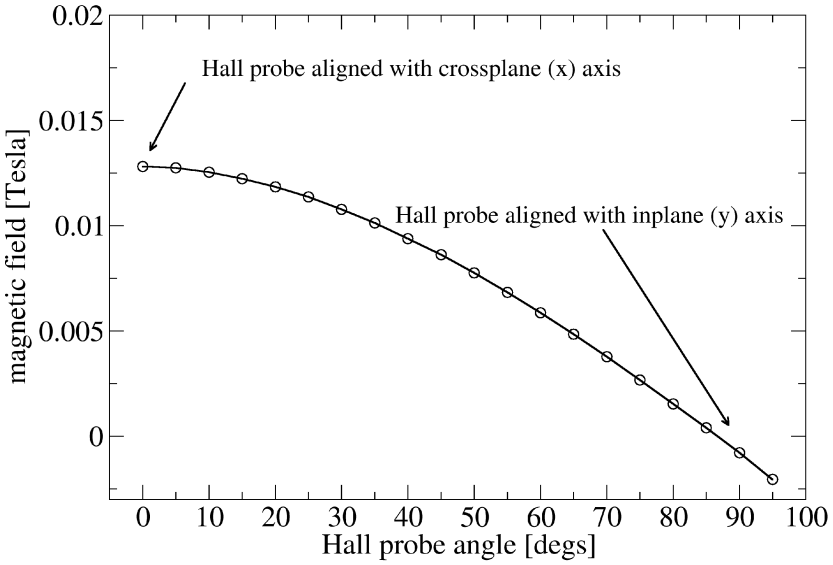

Figure 4.3 Fringe magnetic field measured for 21 MeV at 2 cm from the exit window with the hall probe flat fixed to the collimator which was then rotated through 90°. The probe is orientated perpendicular to the gun (crossplane) at an angle of 0° (max. magnetic field). Earth's magnetic field is 50 × 10^{-6} T and has a negligible effect on the electron beam deflection between the exit window and isocenter.

The magnetic field along the central axis was maximum at the exit window, dropping to approximately 5% of this value at a distance of 12 cm (figure 4.4). There was a sharp drop in the magnetic field in the vicinity of the primary foil holder, approximately 1 cm from the exit window. With the Hall probe fixed at the exit window, the holder was removed. The magnetic field was found to increase by up to

20%. The primary foil holder steel is likely high permeability which acts as a field shunt (Karzmark et al. 2004). Monte Carlo simulations were performed with and without (by fitting a cubic function to the data excluding the point at 1 cm from the exit

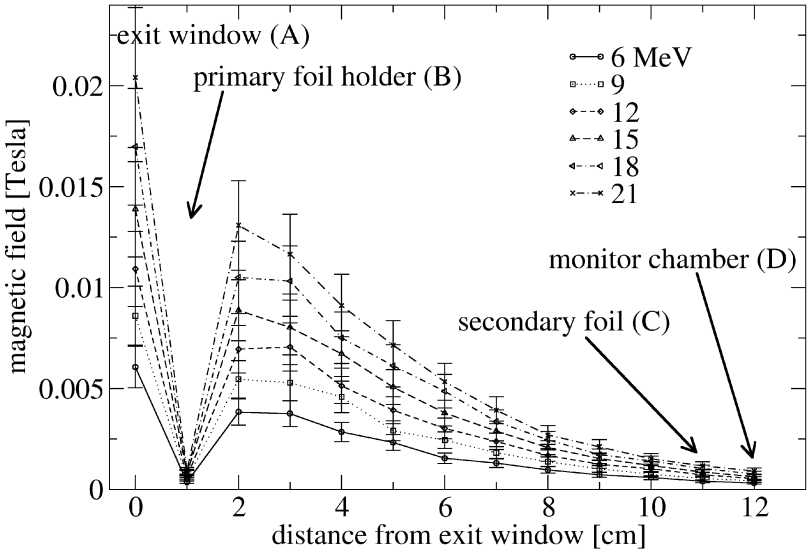

Figure 4.4 Variation in fringe magnetic field with distance from the exit window for nominal 6 – 21 MeV electron beams (bending magnet current: 13.1 – 42.2 A). The field is a maximum at the exit window dropping to ~5% at the secondary foil. The approximate positions of the exit window, primary foil holder, secondary foil and monitor chamber are indicated.

window) the drop in the fringe field. A comparison of exit window only R_{max} profiles showed negligible differences, however, it is likely that (a) the magnetic field measurements (performed every centimetre) did not have the required resolution to

fully model the field in this area and (b) the field above and below the holder is also affected. Independently measured clinical beam profiles demonstrated the holder did affect the inplane symmetry, resulting in a 2-3% change in the off axis ratio. All subsequent measurements were performed with the holder in place – consistent with all three beam configurations.

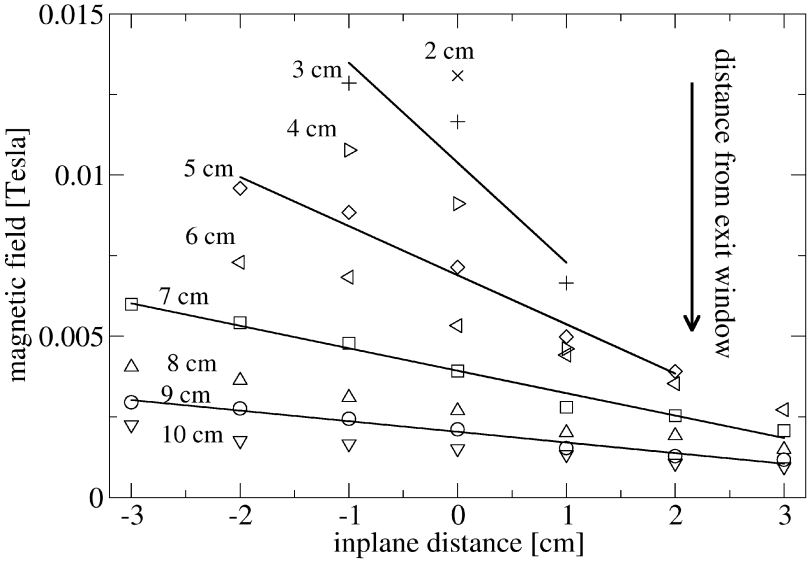

Figure 4.5 Fringe magnetic field measured across the inplane (y) axis (with distance from the collimator rotation axis) for the 21 MeV beam (42.2 A) and at 2 – 10 cm from the exit window. The magnetic field is up to 3 times higher on the negative inplane side. Linear regression was performed on the data at 3, 5, 7 and 9 cm from the exit window to highlight the field gradient.

Figure 4.5 shows the fringe magnetic field measured across the inplane (y) axis for the 21 MeV beam (42.2 A) and at 2 – 10 cm from the exit window. The magnetic field has a clear gradient; up to 3 times higher on the negative inplane (-y) side, with the same shape for 6 – 18 MeV beams. Linear regression was performed on the measured profiles at 3, 5, 7 and 9 cm distances (from the exit window) to highlight the gradient, which had slopes of 3.1, 1.5, 0.7 and 0.3 mT / cm, respectively. This gradient is due to the angled exit pole faces of the bending magnet discussed in section 4.2.1. The magnetic field variation in the crossplane (x) direction was symmetric within the 17% uncertainty of the magnetic field measurements.

4.3.2 Exit Window Only Configuration

Figure 4.6 compares measured and simulated R_{max} inplane dose profiles with the exit window only in the beam line for 6 – 21 MeV and 100 SSD. The measured inplane profiles were offset negative inplane (-y) from the collimator rotation axis by -1.16 cm, -1.14 cm, -1.00 cm, -0.99 cm, -0.87 and -1.16 cm, for 6 – 21 MeV, respectively. The (measured) fringe magnetic field was found to account for the majority of the offset, based on simulation results: -0.83 cm, -0.87 cm, -0.83 cm, -0.84 cm, -0.82 cm and -0.73 cm for 6 – 21 MeV. The spot offset (x_S) and beam angle (Θ) at the exit window accounted for the remainder of the offset.

The exit window water channel was thickened by 0.06 cm (19.3%) over

manufacturer specification to match the 6 MeV R_{max} crossplane (x) FWHM. The exit window water channel is under pressure with a vacuum on one side, making it thicker than specified and angular divergence at the exit window is limited by the width of the profile in the bremsstrahlung tail (Sawkey and Faddegon 2009). A thinner water channel could be used with an increased angular divergence at the exit window, but this has negligible impact on the simulation through the remainder of the treatment head.

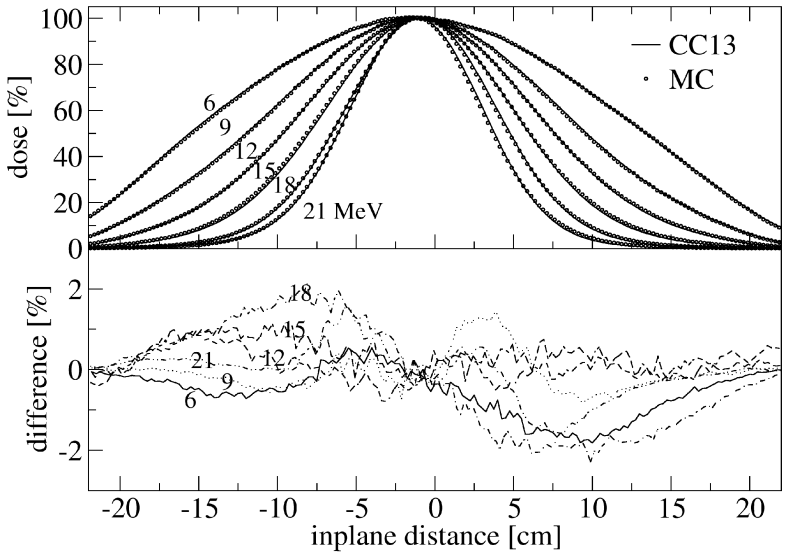

Figure 4.6 Comparison of CC13 and Monte Carlo simulated inplane dose profiles with exit window only in the beam. The exit window water channel was thickened to match the 6 MeV crossplane FWHM with RMS angular divergence added to match the broader inplane profiles and for higher energies (table 4.1).

Table 4.1 Energy – dependent source parameters at the exit window used for clinical treatment head simulations. Spot position is relative to the collimator rotation axis. Root mean square angular divergence.

Energy [MeV]		6	9	12	15	18	21
Spot Offset (x_s) [cm]	Crossplane	0.06	0.02	0.01	-0.02	-0.01	-0.02
	Inplane	0.05	0.02	0.07	0.02	0.04	0.18
Direction cosine (Θ)	Crossplane	-0.006	-0.0035	0.0	0.002	0.003	0.005
	Inplane	-0.001	0.0	-0.003	0.0	0.002	-0.004
Angular Div. $\phi'(\Theta)$ [°]	Crossplane	-	0.4	0.6	0.85	0.6	0.2
	Inplane	0.7	0.8	0.85	1.1	0.8	0.5

Angular divergence, $\phi'(\Theta)$, was added for each of the higher energy beams (9 - 21 MeV) to match the measured crossplane profile widths with the thicker water channel (table 4.1). The required divergence increased with energy up to 15 MeV, where it was a maximum of 0.85° (crossplane) and 1.1° (inplane) and then decreases for higher energies. Measured inplane R_{max} profiles were 0.09 – 0.29 cm wider than corresponding crossplane profiles. Spatial dispersion is usually more significant along the plane of bending of the magnet (inplane in this case) rather than in the transverse plane (Karzmark et al. 2004). Angular divergence ranging from 0.5 – 1.1° was added to match the inplane FWHM for all energies (table 4.1). Simulations showed, however, that using an angular divergence to match the average of the inplane and crossplane R_{max} profile FWHM (i.e. using the same angular divergence inplane and crossplane)

results in errors of less than 1% in clinical beam dose profiles.

4.3.3 Primary Foil Configuration

Measured and calculated R_{max} inplane profiles for the primary foil configuration are shown together in figure 4.7. The profiles for 9, 12, 15, 18 and 21 MeV electron beams have been normalized to 70, 60, 100, 90 and 80%, respectively. The 6 MeV electron beam does not utilize a primary scattering foil and is not included. Monte Carlo simulations and measurements agreed to within 2.5% inplane and better than 2% for crossplane profiles, with dose normalized to 100% on the beam central axis. There was an apparent trend of increasing difference (between Monte Carlo and measurement) with increasing energy. A 0.2 – 0.3 (± 0.03) cm mismatch in the position of the inplane profile peaks was also evident. The peaks were defined by fitting Gaussian functions, restricted to the region of dose greater than 60% of maximum, and calculating the difference in the mean (μ). The beam angle was steered towards the position of the bremsstrahlung profile (R_x) peak (determined by fitting a Gaussian function to the profile restricted to region of profile out to ±10 cm from the collimator rotation axis for 6 – 9 MeV and ±5 cm for 12 – 21 MeV) as measured previously (Faddegon et al. 2009). The R_x profile is dominated by bremsstrahlung x-rays from the exit window and primary scattering foil. Monte Carlo simulation showed that the fringe magnetic field had marginal effect on the offset of the x-ray fluence peak at isocenter, ranging from

0.15 cm at 6 MeV to 0.2 cm at 21 MeV. The beam angle would require adjustment outside the experimental uncertainties reported in section 4.2.3.2 to improve the match to measurements. The fringe magnetic field was increased within the measurement uncertainty (17%) reducing the mismatch in the calculated and measured profile offsets by approximately 0.1 cm in the region of the profiles with greater than 50% of the maximum dose.

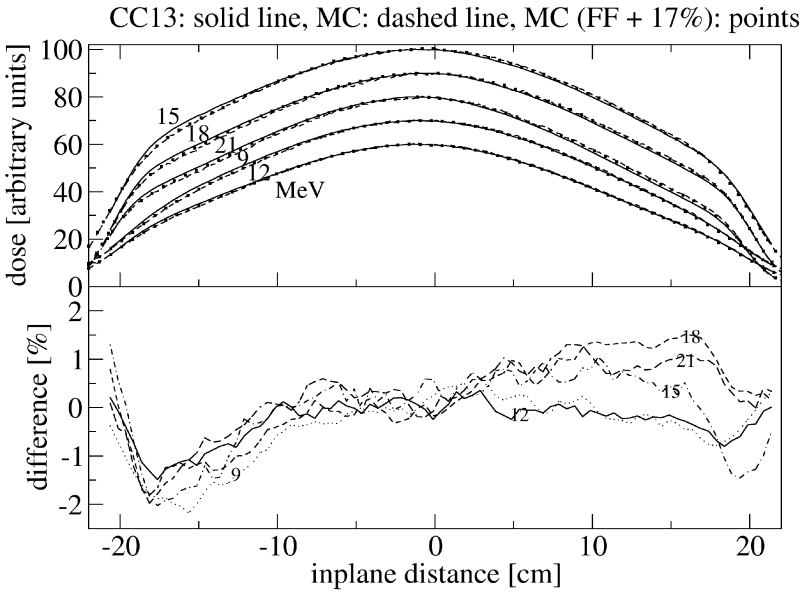

Figure 4.7 Comparison of CC13 and Monte Carlo simulated inplane dose profiles with the primary foil in the beam. Monte Carlo calculations are shown with the measured fringe magnetic field (dashed lines) and measured magnetic field increased by 17% (the total experimental uncertainty in the measurement, points) included in simulations. Primary foil simulations used the same source details as the exit window only configuration.

The offset of the jaws and multi-leaf collimator (MLC) from the collimator rotation axis was set in simulation based on the position of the field edge for the 18 MeV electron beam in primary foil configuration. This field is broad enough to be substantially collimated by the jaws and MLC and has a sharp field edge.The positive and negative jaws were found to be offset by 0.01 cm and -0.01 cm, respectively, while the positive and negative MLC banks were offset by 0.03 cm and -0.02 cm, respectively.

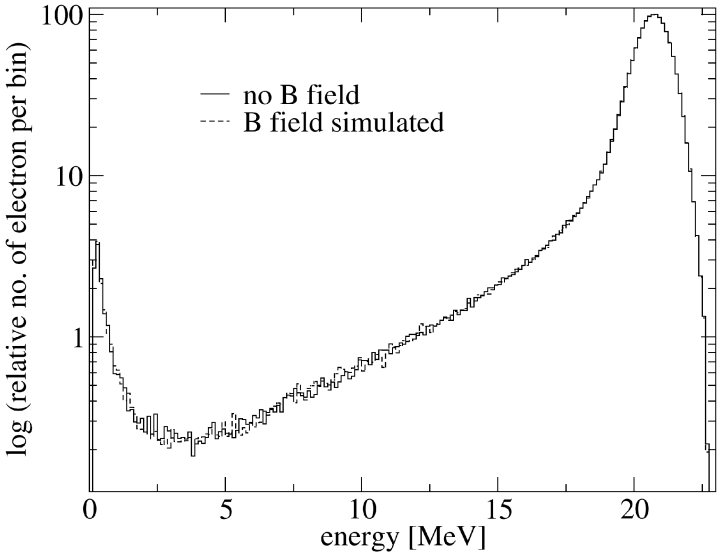

Figure 4.8 Energy spectral distribution on a 12×12 cm^2 plane at 100 cm SSD for 21 MeV electron beam. The simulated fringe magnetic field has negligible effect on the distribution and spectral peak. Note the vertical axis is logarithmic.

Primary foil configuration was previously used to set the mean energy (E) and Gaussian energy spread ($\phi'(E)$) of the incident electron beams based on the measured percentage depth dose (PDD) curves (Faddegon et al. 2009). As expected, the simulated fringe magnetic field was found to have negligible effect on the nominal 6-21 MeV beam energy spectra at the phantom surface (as shown in figure 4.8 for the 21 MeV beam) and the central axis depth dose curves (not shown).

4.3.4 Clinical Beam Configuration

4.3.4.1 Sensitivity Analysis

The results of the sensitivity analysis of idealised symmetric beam R_{max} dose profiles to various sources of asymmetry are listed in table 4.2. Physical parameters varied were the lateral position of the secondary scattering foil and monitor chamber. These components were independently offset by 0.1 cm which represents a plausible physical offset.

The secondary foil offset has a significant effect on the flatness and symmetry of the beam. The effect is largest for the lowest energy beam (6 MeV) with effects on flatness and symmetry of 5.0% and 13.0%, respectively. The effects reduce with increasing energy and are 2-3 times lower at 21 MeV. The effect on the offset of the +50% and -50% dose points is minimal.

Table 4.2 Effect of various sources of asymmetry on initial idealised 6 – 21 MeV symmetric electron beam. The slope (of the line through the points at 12 cm and -12 cm from the central axis) is quoted to the nearest 0.05 % / cm and field offset to the nearest 0.05 cm.

Assymetry	Energy [MeV]	$\Delta_{Flatness}$ [%]	Symmetry [%]	Slope [% / cm]	Field offset [cm]
Sec. Foil offset	6	5.0	13.0	0.5	0.1
[0.1 cm]	9	3.6	14.2	0.6	0.05
	12	5.7	12.5	0.5	0.0
	15	3.4	10.5	0.4	0.0
	18	2.0	8.1	0.3	0.0
	21	1.8	7.2	0.3	0.15
Mon. offset	6	1.0	6.0	0.25	0.35
[0.1 cm]	9	0.3	4.7	0.2	0.45
	12	1.0	3.2	0.1	0.45
	15	0.1	0.4	0.0	0.55
	18	0.6	1.5	0.1	0.50
	21	0.0	0.4	0.0	0.55
Spot offset	6	0.1	3.6	0.15	0.1
[exp. uncert.]	9	0.75	3.4	0.1	0.25
	12	1.9	4.0	0.2	0.25
	15	0.9	4.9	0.2	0.3
	18	1.1	3.8	0.2	0.2
	21	1.0	3.6	0.15	0.3
Beam angle	6	3.1	9.2	0.4	0.3
[exp. uncert.]	9	1.75	7.8	0.3	0.15
	12	1.6	4.4	0.1	0.05
	15	0.5	2.0	0.1	0.05
	18	0.6	1.0	0.05	0.0
	21	0.5	0.9	0.05	0.0

Table 4.2 Continued from previous page.

Assymetry	Energy [MeV]	$\Delta_{Flatness}$ [%]	Symmetry [%]	Slope [% / cm]	Field offset [cm]
Fringe B field	6	1.7	7.5	0.3	0.3
[measured]	9	1.7	7.3	0.3	0.35
	12	3.2	7.6	0.3	0.35
	15	1.0	3.5	0.15	0.3
	18	1.2	5.8	0.2	0.25
	21	2.0	5.8	0.2	0.3

The most significant effect of a lateral shift of the monitor chamber is field offset (table 4.2). As stated in section 4.2.1, with the jaws and MLC set to 40 × 40 cm^2, the monitor chamber collimates the beam and projects a 36 cm diameter field size at isocenter. The field offset is 0.35 cm at 6 MeV, increasing to 0.55 cm at 21 MeV. The effect is largest for the higher energy beams as electron scattering between the chamber and the measurement point is much less. Therefore it seems prudent to set the monitor chamber offset in simulations based on the position of the measured field edge for the higher energy beams (15 - 21 MeV).

The electron spot at the exit window (x_s) was laterally offset by the estimated experimental uncertainty in the measured spot position (0.05 cm). The spot position, similar to the monitor chamber, largely affects the field offset. The effect on flatness and symmetry is minimal and shows no trend with energy (table 4.2). The uncertainty in the measured spot position could lead to 0.1 – 0.3 cm field offset for the 6 – 21 MeV

beams, respectively. The lateral spot position is therefore a significant contributor to the field offset, along with the monitor chamber position.

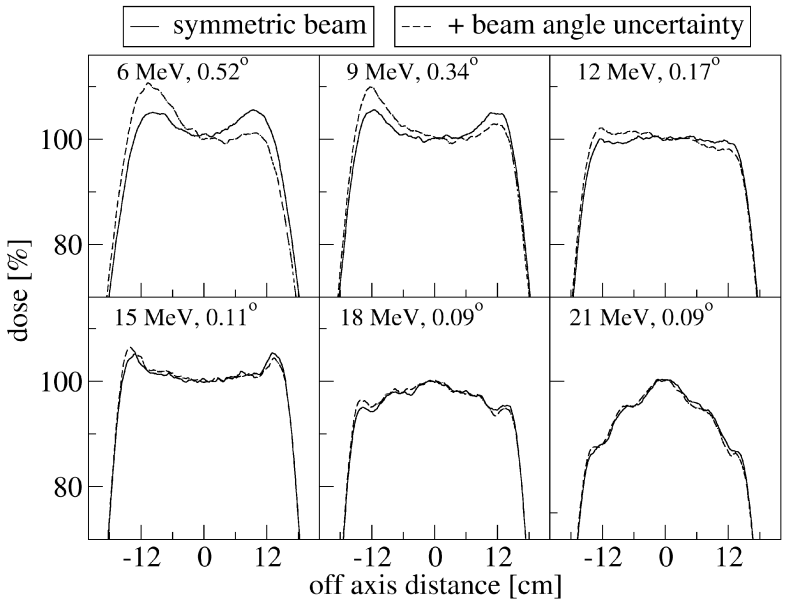

Figure 4.9 The effect of beam angle - varied by experimental uncertainty – on symmetric dose profiles (which contain no sources of asymmetry) for 6 – 21 MeV beams and 40×40 cm² field size. Effects are quantified in table 4.2.

The uncertainty in the beam angle increases with decreasing energy as outlined in section 4.2.3.2, ranging from 0.52 – 0.09° for 6 – 21 MeV. This is carried through to the sensitivity analysis with the 6 MeV dose profile affected most by beam angle uncertainty (figure 4.9 and table 4.2). The effect of the beam angle uncertainty on the higher energy (18 and 21 MeV) dose profiles is very small; less than 1% / 0.05 mm.

This confirms that it is advisable to set the lateral offset of the monitor chamber using the high energy beam measurements since the uncertainty in the source parameters at the exit window are initially lower. The steps or "undulations" seen in the higher energy dose profiles (figure 4.9) are due to the 3 stepped layers of the Al secondary scattering foil. These undulation positions are also effective to set the lateral offset of the foil with the fringe magnetic field included in simulations.

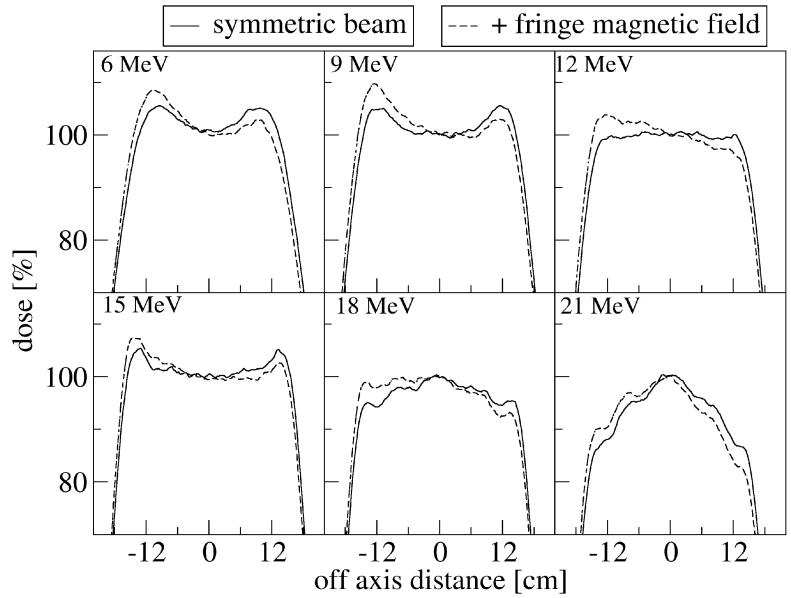

Figure 4.10 The effect of the simulated fringe magnetic field on symmetric dose profiles (which contain no sources of asymmetry) for 6 – 21 MeV beams and 40×40 cm^2 field size. Effects are quantified in table 4.2.

The effects of the fringe magnetic field on the idealised symmetric dose profiles

are shown graphically in figure 4.10 (and also quantified in table 4.2). The fringe field effects the flatness, symmetry, slope and (field) offset. The effect on flatness and symmetry is a maximum at 12 MeV. The effect on field offset is 0.3 cm (average). It is expected that the fringe field should have a similar effect for all energies since the measured fringe field was found to be a linear function of bending magnet current. The increase in magnitude of the fringe field with energy is counterbalanced by the increase in momentum of electrons at each increase in energy. However, there is some saturation of the bending magnet above 37 A (Faddegon et al. 2009) which could explain non-linear effects at higher energies (e.g. the lower offset of the 21 MeV beam exit window only R_{max} profile). The fringe field is responsible for a single component of the measured inplane (y) offset, which ranged from -0.71 to -1.99 cm. The remainder of the offset is the result of the spot offset and beam angle at the exit window, and the monitor chamber offset.

4.3.4.2 Comparison of Measurements and Simulations

Measured and Monte Carlo simulated dose profiles are compared in figure 4.11 for the 6 - 21 MeV clinical electron beams at 100 cm SSD. R_{max} crossplane (x) profiles have been normalised to 100% on the central axis. R_{max} inplane (y) profiles are normalised to 120% for clarity. Profiles in the bremsstrahlung (R_x) are also included, with the crossplane and inplane profiles normalised to 20% and 30%, respectively. The

maximum differences between measured and simulated R_{max} dose profiles were 3%, 2.4%, 2.5%, 2.6%, 2.5% and 2% for 6 – 21 MeV, respectively, with comparison limited to the low dose gradient region (greater than 80% of maximum dose) and each profile normalised to 100% on the central axis. The field edges matched to within 0.2 cm, 0.18

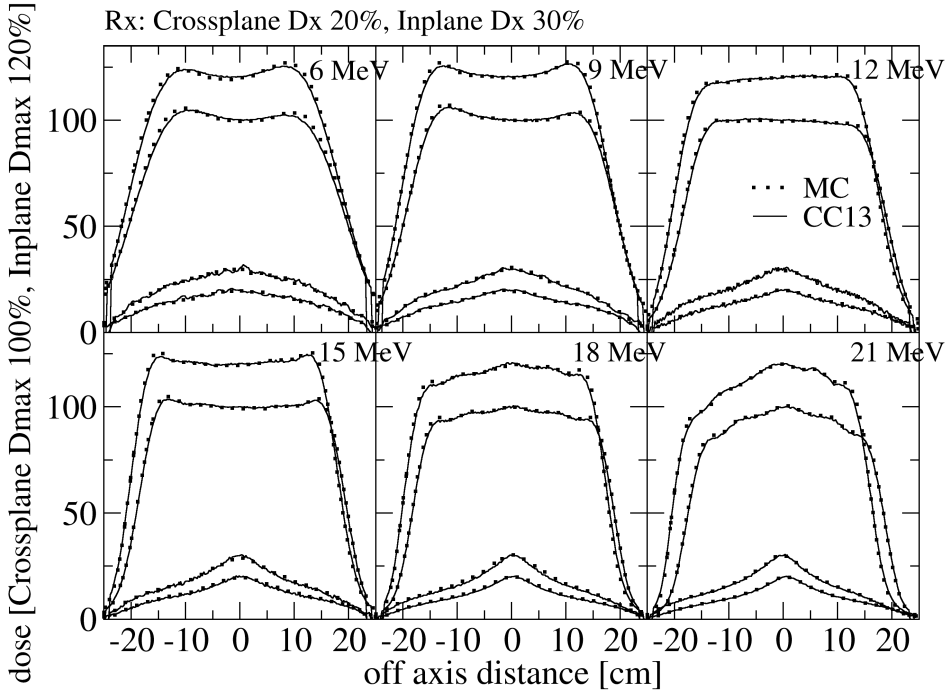

Figure 4.11 Comparison of Monte Carlo calculated and CC13 measured dose profiles for clinical beam 6 – 21 MeV and 40×40 cm² field size at 100 cm SSD. Percentage difference are shown in figure 4.12.

cm, 0.17 cm, 0.09 cm, 0.15 cm and 0.16 cm for 6 - 21 MeV. There was an improved

match (of up to 0.48 cm for 6 MeV) at the extreme edge of the field due to the simulation of the peripheral material below the MLC banks. Monte Carlo simulations show good agreement with the shape and offset of the measured R_x profiles in the bremsstrahlung tail.

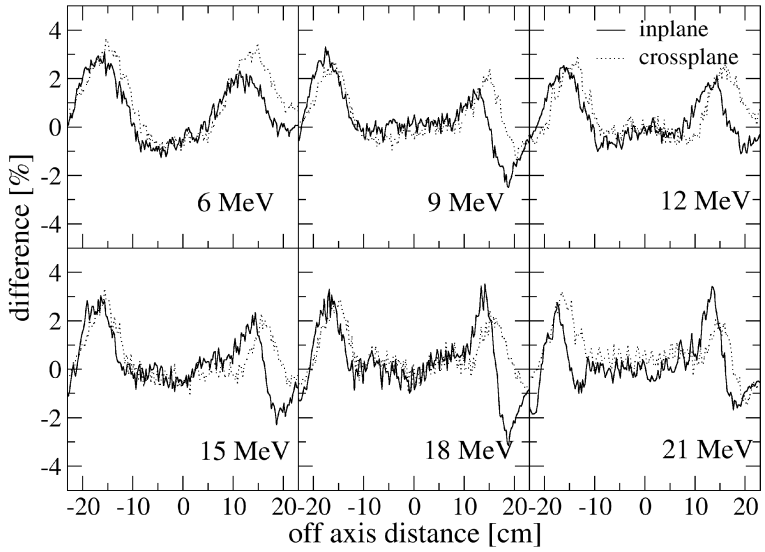

Figure 4.12 Percentage difference between Monte Carlo calculated and CC13 measured R_{max} dose profiles (figure 4.11) for clinical beam 6 – 21 MeV and 40×40 cm² field size at 100 cm SSD.

For clinical beam simulations, the source details, magnetic field and component offsets (now the same for all energies), were initially set as determined by experimental measurements. These parameters were then adjusted, iteratively and within respective

experimental uncertainties and guided by sensitivity analysis, until a good match to measured profiles was achieved. With the secondary scattering foil and monitor chamber fixed in a single position for all energies, the simulated dose distributions are

Table 4.3 Offset of secondary scattering foil and electron monitor chamber from collimator rotation axis.

	Secondary Scat. foil		Monitor chamber	
	Digital photo.	*Simulation*	*Digital photo.*	*Simulation*
Crossplane [cm]	-0.01 ± 0.03	0.02	0.07 ± 0.03	0.03
Inplane [cm]	-0.04 ± 0.03	-0.065	-0.05 ± 0.03	-0.10

in better agreement with measurements than previous work (Faddegon et al. 2005). The secondary scattering foil and monitor chamber lateral offsets from the collimator rotation axis were estimated from digital photographs and are listed in table 4.3. The offsets used in simulations are also given in table 4.3. The offsets were set to match the field edge and undulations of the measured dose profiles of the higher energy beams (18 and 21 MeV) with the fringe magnetic field included in simulations. Three out of four of the simulation offsets were within the uncertainty (0.03 cm) of those estimated by digital photographs. The simulation offsets were within 0.05 cm of those estimated from digital photographs or a maximum of 0.02 cm outside the 0.03 cm photograph estimated uncertainty for all case.

Table 4.1 lists the energy – dependent source parameters used in clinical beam

simulation. The asymmetric angular divergence was selected to match the FWHM of R_{max} dose profiles for exit window only configuration. The spot offsets and beam angles (direction cosines) were varied within experimental uncertainty with the secondary foil and monitor chamber lateral position fixed and the fringe magnetic field simulated. This method resulted in a good match between measurements and simulations except for 6 MeV crossplane. With the 6 MeV crossplane spot offset within experimental uncertainty (spot placed at 0.0 cm), the monitor chamber would need to be offset by over 0.1 cm, outside the uncertainty of the photograph estimate and in the opposite direction to the offset which resulted in a good match to the field edge for the higher energies. Alternatively, the beam angle (or fringe magnetic field strength in the case of inplane disagreement) could also be adjusted (within uncertainty) to improve the match at the field edge; however, this also has a significant effect on the flatness and symmetry of the beam. It was therefore necessary to set the 6 MeV crossplane spot offset 0.06 cm outside the uncertainty of the measured spot position (Faddegon et al. 2009) with the monitor chamber lateral offset fixed for all energies (at 0.03 cm). Never-the-less, inclusion of the fringe magnetic field (as measured) and adjusting the beam angle, spot offset and secondary foil and monitor chamber offsets, realistically and within experimetal tolerances, has helped further restrict simulation parameters and resulted in excellent agreement with measured dose distributions.

4.4 CONCLUSIONS

Large electron fields with the applicator removed and jaws and multi-leaf collimator set to maximum (40×40 cm^2) are most sensitive to electron source and treatment head simulation parameters. The fringe magnetic field from the bending magnet downstream of the exit window is a significant contributor to beam inplane asymmetry (up to 8%). Sensitivity analysis of profiles, with parameters varied within experimental uncertainty, is helpful in selecting simulation parameters. The magnetic field was measured and included in the simulation with the subsequent calculated dose demonstrating a superior match to measured electron beam dose distributions. There are many parameters which can be varied in order to obtain a good match between measured and simulated dose. With tightened tolerances on these parameters in this study, it is expected that the simulated fluence more accurately represents that of the actual linac.

5. Characterisation of an Extendable Multi-leaf Collimator for Clinical Electron Beams

5.1 INTRODUCTION

Electron beam therapy is typically administered under fixed source-to-surface distance (SSD) conditions using an electron applicator and a custom lead alloy insert. It is a common modality for treating superficial tumours of the chest wall. Clinical evidence shows the benefit of boosting the breast tumour excision site with electrons (Bartelink et al. 2001). The potential for electron breast boost geographic misses has been identified, highlighting the need for accurate tumour bed localisation on a daily basis (Fraser et al. 2010). The potential for dose calculation inaccuracies due to approximations made by commercial planning software has also been shown (Coleman et al. 2005). In addition to the accuracy improvements introduced by using Monte Carlo-based dose calculation, electron beam therapy would also benefit from more accurate and precise techniques of delivery.

Complex and precise electron dose delivery is an active area of research, particularly the use of modulated electron and mixed (x-ray and electron) beam therapy techniques (Li et al. 2000, Ma et al. 2003, Gauer et al. 2010). Modulated electron beam

therapy provides a method of conformal treatment and has been shown to provide a reduction in dose to distal organs-at-risk and critical structures (Ma et al. 2003, Jin et al. 2005). Conventional methods for electron beam collimation are labour and time intensive in their construction and are considered inadequate for use in the sequential delivery of multiple complex fields. A number of authors have investigated the use of either the x-ray multi-leaf collimator (pMLC) or a dedicated electron multi-leaf collimator (eMLC) for un-modulated or modulated electron beam delivery.

Lee et al. (2000) investigated two methods of electron beam collimation: (1) using the existing photon multi leaf collimators (pMLC) in a helium atmosphere to reduce in-air electron scatter, and (2) using a MLC specifically designed for electron beam collimation located at the level of the last scraper of the 25×25 cm^2 applicator on a Varian accelerator. Significant improvements, particularly in the dose profile penumbra, were reported when the treatment head air was replaced with the helium based system. Simulations were also performed on an electron specific MLC with unfocused tungsten leaves 1.5 cm thick and 0.5 cm wide which provided sufficient collimation for modulated electron fields.

Hogstrom et al. (2004) proposed a retractable eMLC used for un-modulated or intensity modulated therapy which could (a) retract to 63 cm source-to-collimator distance (SCD) for arc therapy, or deploy to (b) 80 cm or (c) 90 cm SCD for isocentric and SSD set-ups, respectively. The eMLC design was capable of treatment which was

equivalent to that delivered by a standard cerrobend insert, due to similar dosimetric properties (up to 3% difference in the build-up region the of percentage depth dose curve). The benefits of isocentric electron treatment were discussed, particularly in breast and head and neck (e.g. posterior neck region) cases when combined with isocentric x-ray beams. Advantages would include faster treatments due to no treatment room re-entry and no need to reposition the couch.

Gauer et al. designed, evaluated (2006) and characterised (2008) an add-on eMLC with interchangeable distance holders for variable SCD (72 cm or 84 cm) and isocentric delivery on a Siemens Primus accelerator. The final eMLC design consisted of two banks of 24 brass leaves. Attachment and gantry stability was evaluated and found to result in a maximum displacement of 0.6 mm. The dosimetric properties, including field size dependence, field abutment and leakage, of the eMLC were evaluated. Dose profiles and percentage depth dose curves were compared with that of the standard applicator demonstrating a 0.8 – 0.4 cm (6 – 14 MeV) larger penumbra and build-up effect, which the authors state was mainly the result of difference in air-gap.

Klein et al. (2008) used the 120 leaf pMLC on a Varian accelerator to develop and evaluate narrow (1 - 10 cm) beam segments for modulated electron treatments at 6 – 20 MeV using Monte Carlo methods. The study employed shorter source-to-surface distances (70 - 85 cm) in order to improve the beam penumbrae. Monte Carlo planning was then performed on idealised phantom and clinical cases for

segmented and dynamic leaf delivery (Klein et al. 2009). Sparing of distal organs at risk was reported, however, it was also noted that the use of shorter SSDs may be clinically impractical due to potential collisions and some treatment sites may need to be treated at larger SSD (>75 cm), degrading the penumbra and plan resolution.

Jin et al. (2008) investigated modulated electron therapy using the pMLC on Siemens Primus accelerator. A Monte Carlo method of inverse planning was developed. Again, a shortened SSD (60 cm) was employed to improve the penumbra of 6 – 15 MeV electron beams. A treatment consisting of 22 segments was planned and delivered on a breast phantom with measurements and simulations reported to agree to 2% / 1 mm.

It can be concluded that the current commercially available x-ray MLCs are generally unsuitable for electron beam collimation at nominal SSD (100 cm). Electron beams should ideally be collimated (in air) within 10 cm of the skin surface to reduce the size of the penumbra and maintain beam flatness, especially at lower (more widely scattered) beam energies. This would also aid matching and dose uniformity at beam junctions (Steel et al. 2009, Eldib et al. 2010) in modulated or abutted fields. Studies which utilised the pMLC for electron beam collimation utilised a shortened SSD in order to improve the penumbra. A dedicated retractable eMLC may be the optimal method for electron beam collimation. This could be placed in close proximity (5 – 10 cm) to the patient to provide an adequate penumbra and resolution and then remotely

retracted to allow concomitant x-ray treatment.

This study is concerned with characterisation of an extendable x-ray MLC for collimation of 6 - 21 MeV electron beams from a linear accelerator. The MLC was modelled in EGSnrc/MCRTP (Faddegon et al. 1998) and validated against water phantom dose measurements. The dose profile penumbrae and electron scattering were evaluated and dosimetric properties were compared with the standard applicator. Potential concerns, including bremsstrahlung x-ray dose and dose inhomogeneity in abutting fields of differing energy were investigated. The energy modulation possibilities and variation in therapeutic range achievable were examined for an wedge shaped dose distribution. A concomitant eMLC- collimated electron breast boost was planned using Monte Carlo calcualtions to demonstrate the isocentric treatment capabilities of the eMLC. The resulting plan was compared with the fixed SSD approach using a standard applicator.

5.2 MATERIALS AND METHODS

5.2.1 Extendable Multi-leaf Collimator

A TiGRT Dynamic Multi-leaf Collimator (DMLC H, LinaTech, Sunnyvale, CA, USA) was mounted on a Siemens Oncor linear accelerator (Siemens OCS, Erlangen, Germany) using 30 cm steel extenders at a SCD (side of the collimator closest to the

patient) of 81.6 ± 0.1 cm (figure 5.1). The eMLC was centred to within 0.03 cm of the central axis. It is composed of two banks of 51 tungsten leaves which have a height (thickness) of 7 cm along the beam axis. The central 19 leaves in each bank have a width of 0.2 cm (to the nearest millimeter) perpendicular to leave motion. The outer 32 leaves of each bank are 0.3 cm wide. The maximum physical field size is 15.0 × 17.0 cm^2. The leaves provide full overtravel and have a position uncertainty of 0.05 cm. The eMLC replaced the accessory rails and electron applicator, and in its full clinical implementation could be remotely retractable and deployed from approximately 59 – 95 cm SCD.

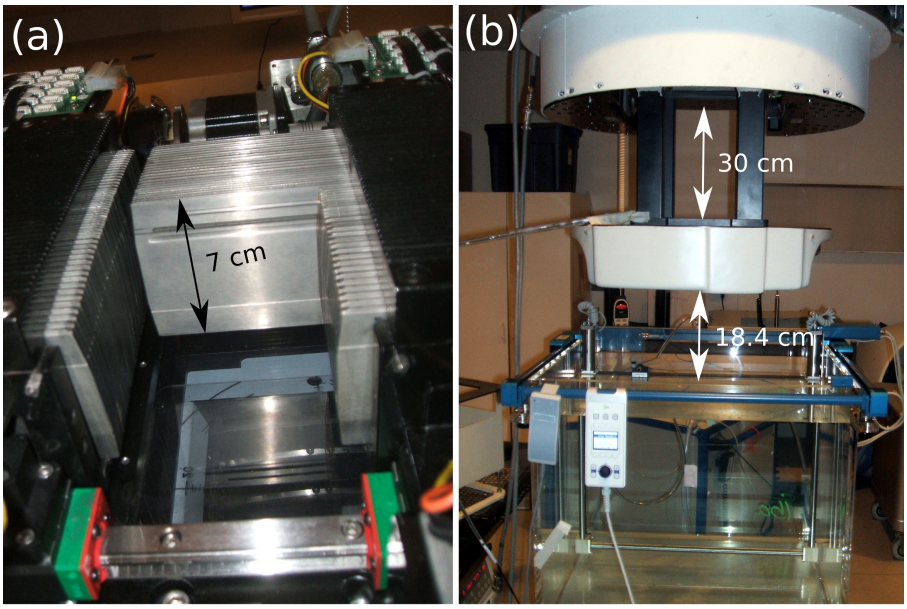

Figure 5.1 Extendable MLC: leaf banks (a) and mounted on Siemens Oncor accelerator at 81.6 cm SCD using 30 cm long steel extenders (b).

5.2.2 Dose Measurements

Dose profiles and percentage depth dose curves were measured in a water phantom (IBA Dosimetry, Bartlett, TN, USA) for 6, 9, 12, 15, 18 and 21 MeV electron beams, 71.6 cm and 81.6 cm SCD and 90 cm and 100 cm SSD. These SSDs represented airgaps of 8.4 cm and 18.4 cm from the lower surface of the eMLC to water surface, respectively. Dose profiles were measured with a CC13 thimble chamber and an EFD diode for nominal 3 × 3, 10 × 10 and 20 × 20 cm^2 field sizes at several depths including R_{max} and a few centimeters beyond the practical range (R_x). Percentage depth dose curves were measured with the EFD diode. To evaluate the effects of the eMLC on clinical beams, the dosimetric properties of the eMLC collimated fields were compared with those of the standard 10 × 10 cm^2 electron applicator (95 cm SCD) at 100 cm SSD.

A wedge shaped dose distribution was planned using Monte Carlo simulation to demonstrate the eMLC energy modulation possibilities, and variation in target depth coverage achievable. The plan used a single isocentre and the six available electron beam energies (6 - 21 MeV) matched across the maximum available eMLC field size. To ensure that scatter from the eMLC banks was adequately modelled, dose profiles were measured (at 1 cm depth) for the the six adjacent fields collimated with the eMLC (one for each beam energy) for comparison with the simulated wedge profile components.

In order to maintain the highest dose resolution, while potentially reducing the number of leaves and complexity of the eMLC, the optimal leaf width was also investigated. For this investigation, dose profiles were measured with 2, 4, 6 and 8 (0.2 cm) leaves alternating open or closed. The dose was normalised to the maximum in the open field segment and the subsequent reduction in dose under the closed leaf segment was evaluated.

Relative output factors were measured using an EFD diode and digital electrometer (Model 35614: Keithley Instruments, Cleveland, OH) at 90 cm and 100 cm SSD with the eMLC defining 2 × 2, 3 × 3, 10 × 10 and 20 × 20 cm^2 nominal field sizes and the detector at the depth of maximum dose for each field size.

5.2.3 Monte Carlo Simulation

Monte Carlo simulation was performed with the EGSnrc/BEAMnrc (Rogers et al. 1995) and MCRTP (Faddegon et al. 1998) codes. The treatment head above the eMLC was previously modelled to high accuracy for 6 – 21 MeV electron fields and included simulation of the fringe magnetic field from the bending magnet (chapter 4). The eMLC was modelled in the EGSnrc user code MCRTP for 71.6 cm and 81.6 cm source-to-collimator distances (SCD) and 90 cm and 100 cm SSD for characterisation and comparison with measured data. Tungsten with a density of 19.3 g cm^{-3} was used to

model the leaf material. The treatment head was also modelled with standard 10 × 10 cm^2 electron applicator for comparsion of applicator and eMLC dosimetric properties.

The Electron (ECUT/AE) and photon (PCUT/AP) cut-offs were 0.7 MeV and 0.01 MeV, respectively. The PRESTA-I boundary-crossing algorithm was used in MCRTP. The electron step algorithm was PRESTA-II (Kawrakow and Rogers 2000). The default maximum step size (SMAX) of 5 cm was used. The maximum fractional energy loss per step (ESTEPE) was set to 0.25 (default). Dose-to-water was calculated in a phantom containing 2.0 × 2.0 × 1.0 mm^3 voxels as part of the eMLC simulation. The EGSnrc particle tracking variable LATCH was used to extract scattered electron and contaminant bremsstrahlung x-ray dose components for water phantom dose calculations.

5.2.4 Patient Plan

An electron breast boost was retrospectively planned using Monte Carlo simulation. The planning procedure used the methodology previously described and experimentally validated (by RANDO phantom measurements) by Coleman et al. (2005). Plans were generated in parallel for a conventional (SSD) applicator boost and an isocentric boost using the extendable eMLC. The latter utilised the same isocentre as the tangential whole breast irradiated (WBI) x-ray fields. The applicator plan required a shift from the x-ray isocentre of 11.48 cm, 5.72 cm and 0.6 cm in the lateral (ΔLAT), anterior-

posterior (ΔAP) and superior-inferior (ΔSI) directions, respectively. The applicator plan isocentre was shifted towards the posterior, laterally and in the inferior direction.

Table 5.1 compares the two plan configurations. Both plans utilised a single 18 MeV electron beam to enclose the deepest extent of the tumour bed with the 80% isodose line and limit the dose to the underlying lung tissue. Each plan also used a 300º gantry angle so that the beam was normal to the patient skin. The collimator-to-skin distance (air-gap) was 10 cm in both cases. The applicator plan used the 15 × 15 cm^2 applicator with a custom designed cerrobend insert. The displacement of the eMLC leaves (field offset) in the direction of motion (Δx) and perpendicular to the the direction of motion (Δy) required to maintain the same treatment field position (on the patient skin) as the applicator plan was calculated using:

$$\Delta x = \cos(\theta)\ (\Delta LAT) + \sin(\theta)(\Delta AP) \tag{5.1}$$

$$\Delta y = -\Delta SI \tag{5.2}$$

Table 5.1 Comparison of conventional applicator SSD and eMLC isocentric electron breast boost plan configurations. The eMLC plan requires no patient repositioning and can be performed concurrently with tangential x-ray field irradiation using the same isocentre. The isocentre shift indicates the treatment couch repositioning required for the applicator plan. The field offset was the displacement of the eMLC leaves in the direction of motion (Δx) and perpendicular to the the direction of motion (Δy) required to maintain the same treatment field position (on the patient skin) as the applicator plan.

	Applicator	eMLC
Mode	SSD	Isocentric
Energy [MeV]	18	18
Iso. shift (ΔLAT, ΔAP, ΔSI) [cm]	11.48, 5.72, 0.60	~
Gantry angle (θ) [°]	300	300
SSD [cm]	105.0	92.2
SCD [cm]	95.0	82.2
Air-gap [cm]	10.0	10.0
Field offset (Δx, Δy) [cm]	~	0.78, -0.60

Monte Carlo dose calculations were performed on the patient 3D dataset in MCRTP. The resultant 3D dose data was imported into the PlanUNC planning software (Schreiber et al. 2006) which was used to compare isodose distributions and dose volume histograms (DVH) for the target (CTV), right lung and whole heart. DVHs were quantitatively compared by $D95_{CTV}$: the minimum dose covering 95% of the target volume, $V20_{lung}$ (cm^3): the lung volume containing at least 20% of the prescribed dose,

$V10_{heart}$ (cm^3): the heart volume containing at least 10% of the prescribed dose and also the mean dose to each of these structures. The plans were also delivered to a water phantom for comparison of simulated dose profiles and percentage depth dose curves.

5.3 RESULTS AND DISCUSSION

5.3.1 Dosimetric Characteristics and Model Validation

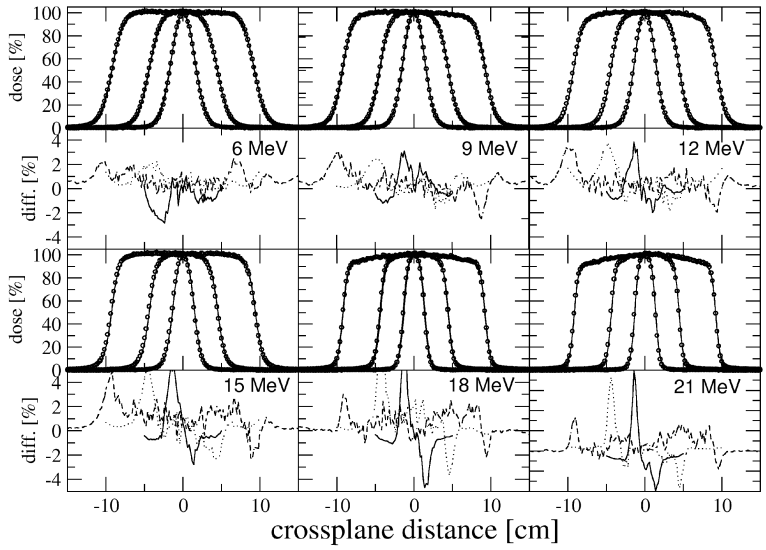

Figure 5.2 Cross-plane profiles for 2×2, 10×10 and 20×20 cm^2 nominal field sizes collimated with eMLC. 6, 9 and 12 MeV (top row left to right). 15, 18 and 21 MeV (lower row left to right). Monte Carlo calculations (points) are compared with diode measurements (lines).

Measured water phantom dose distributions for fields collimated with the eMLC were

compared to Monte Carlo simulations at 90 cm and 100 cm SSD. Figure 5.2 shows the comparison of measured and simulated dose profiles for nominal 3 × 3, 10 × 10 and 20 × 20 cm^2 square fields at 100 cm SSD. Measured and simulated dose profiles and percentage depth dose curves showed agreement of 2% / 2 mm, and generally better, at both SSDs.

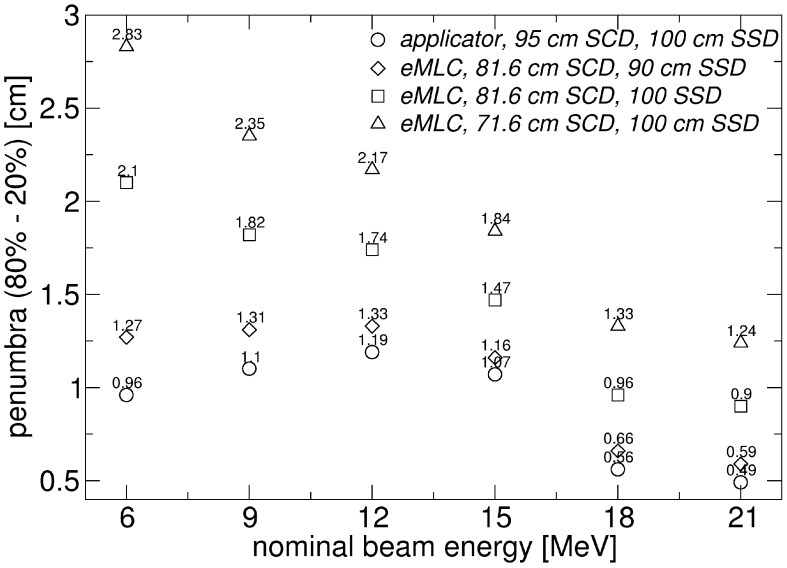

Figure 5.3 Comparison of applicator and eMLC dose profile penumbrae for various eMLC source-to-collimator and source-to-surface distances.

Figure 5.3 compares the penumbra widths (80% - 20% of relative dose) of the standard 10 × 10 cm^2 applicator and the 10 × 10 cm^2 eMLC field for 6 – 21 MeV electron beams. The penumbral widths for three different eMLC configurations: (i) 81.6

cm SCD, 90 cm SSD (8.4 cm airgap), (ii) 81.6 cm SCD, 100 cm SSD (18.4 cm airgap) and (iii) 71.6 cm SCD, 100 cm SSD (28.4 cm airgap) are included. The eMLC penumbra was wider in all cases, however, it was within 0.3 – 0.1 cm (6 – 21 MeV) of the applicator penumbra when the airgap was reduced to configuration (i) above. This demonstrated that the difference in applicator and eMLC penumbra was mainly the result of the difference in airgap between the collimator and phantom surface.

Table 5.2 Dose profile parameters for 10 × 10 cm² field and 100 cm SSD. Dosimetric and therapeutic field widths are the distances between the 50% and 80% off-axis doses relative to the central axis dose, respectively. The penumbra is the distance between 20% and 80% off-axis doses.

Dose profile parameters [cm]	Applicator						eMLC					
	energy [MeV]						*energy [MeV]*					
	6	*9*	*12*	*15*	*18*	*21*	*6*	*9*	*12*	*15*	*18*	*21*
Dosimetric field width	10.18	10.28	10.35	10.39	10.24	10.22	10.30	10.35	10.41	10.42	10.25	10.22
Therapeutic field width	9.10	9.19	9.22	9.39	9.67	9.71	8.25	8.49	8.65	8.97	9.30	9.32
Penumbra	0.97	1.11	1.19	1.08	0.57	0.51	2.13	1.84	1.76	1.47	0.96	0.91

The clinically applicable R_{max} dose profile parameters for the 10 × 10 cm² applicator and eMLC (SCD = 81.6 cm) fields at 100 cm SSD are compared in table 5.2. The dose profiles of the eMLC had lower off-axis dose fall-off as quantified by the penumbra and therapeutic field (distance between 80% relative dose points) widths.

The penumbra of the 6 - 21 MeV beams was 1.2 - 0.4 cm wider and the therapeutic field widths were 0.85 – 0.4 cm narrower than those of the 10 × 10 cm^2 applicator.

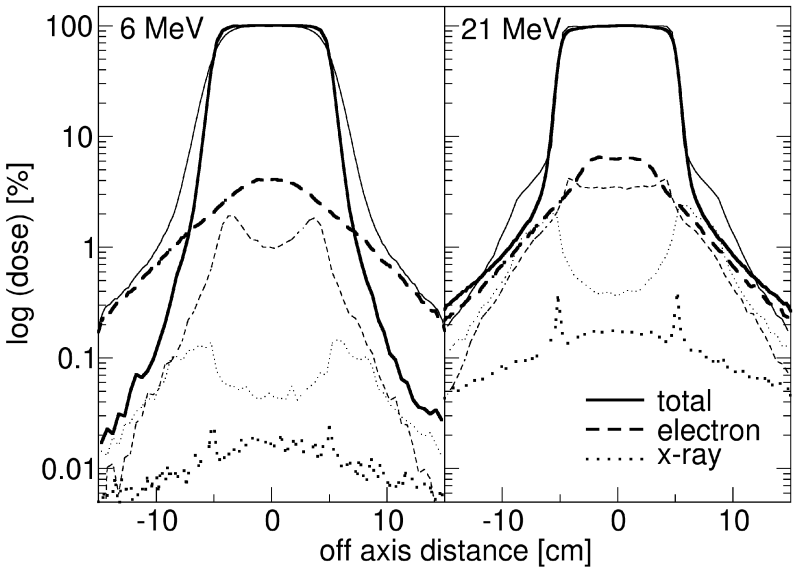

Figure 5.4 Dose profiles for 6 and 21 MeV electron beams showing dose contribution from total electron beam and scattered electrons and bremsstrahlung X-rays from eMLC (thick lines) at 81.6 cm SCD and applicator (thin lines) at 95 cm SCD for 100 cm SSD.

The eMLC should ideally generate a penumbra similar to the applicator. Electrons scattered from the eMLC had a marginal effect on the penumbra (figure 5.4); a maximum of 2.5% and 2.8% of the dose in the penumbra of the 10 × 10 cm^2 field size at 6 MeV and 21 MeV, respectively. For comparison, electrons scattered from the 10 × 10 cm^2 applicator contributed a maximum of 1.2% and 2.5% to the dose in the

penumbra for the same energies. Electrons from the eMLC contributed 4.1% and 6.4% to the dose at R_{max} on the central axis (i.e. to relative output) for 6 MeV and 21 MeV, respectively. The scattered electron contribution to the dose at R_{max} for the 10×10 cm^2 applicator was lower, 1.1% and 3.4 % at 6 MeV and 21 MeV, respectively.

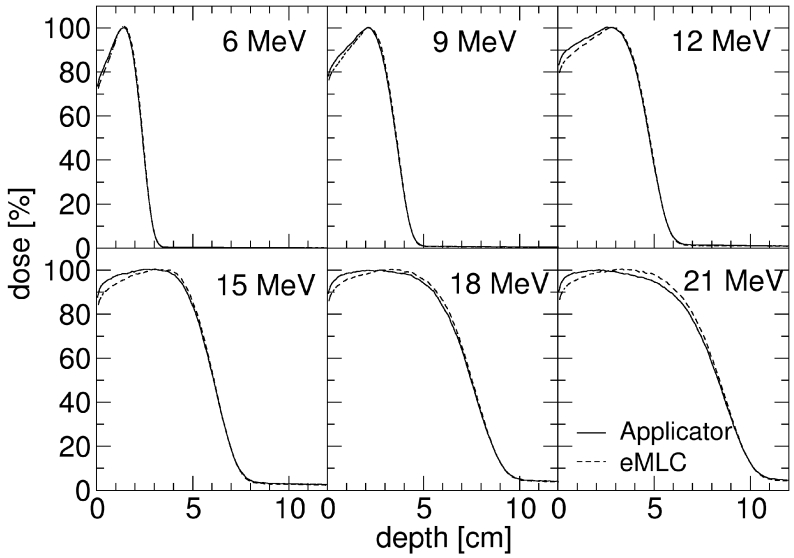

Figure 5.5 Comparison of central axis depth dose curves for applicator (95 cm SCD) and eMLC (81.6 cm SCD) nominal 10×10 cm^2 fields at 100 cm SSD.

The electron range in tungsten is short (only 0.5 cm for 20 MeV electrons) and the attenuation of the bremsstrahlung (x-rays) is high, therefore x-rays from the thick eMLC leaves had an insignificant contribution to the central axis dose at R_{max} (figure 5.4), 0.2% at 21 MeV and an order of magnitude lower at 6 MeV. This contribution is

negligible compared to the x-ray dose from the treatment head, which is a maximum of 5% at 21 MeV for a 40 × 40 cm^2 field (Hogstrom et al. 2004). For the applicator, the contribution of bremsstrahlung to the central axis dose at R_{max} was < 0.1% and 0.4% at 6 MeV and 21 MeV, respectively. The contribution was much higher at the edge of the applicator-defined field, however, a maximum of 0.1% and 2.3 % for the 6 MeV and 21 MeV electron beams, respectively. This increase is the result of bremsstrahlung creation and transmission in the 1.3 cm thick brass scraper.

Table 5.3 Percentage depth dose (PDD) parameters for 10 × 10 cm^2 field and 100 cm SSD. R_{100}, R_{80} and R_{50} are the depths of 100, 80 and 50% of maximum dose, respectively. $D_{0.5}$ and D_x is the dose (%) at 0.5 cm depth and in the bremstrahlung tail, at depths of 5, 7, 8, 10, 12 and 13 cm for 6 – 21 MeV, respectively.

PDD parameters	Applicator						eMLC					
	energy [MeV]						*energy [MeV]*					
	6	*9*	*12*	*15*	*18*	*21*	*6*	*9*	*12*	*15*	*18*	*21*
$D_{0.5}$ [%]	84.7	86.1	90.1	95.0	96.3	97.4	82.2	83.1	86.5	90.6	92.6	93.2
R_{100} [cm]	1.4	2.1	2.7	3.0	2.1	1.9	1.4	2.1	2.8	3.0	2.7	2.2
R_{80} [cm]	2.02	3.05	4.07	5.17	6.25	6.85	2.06	3.09	4.11	5.25	6.38	7.06
R_{50} [cm]	2.39	3.58	4.76	6.08	7.48	8.34	2.41	3.61	4.78	6.11	7.54	8.42
D_x [%]	0.4	0.8	1.4	3.0	4.0	4.5	0.3	0.7	1.1	2.7	3.8	4.1

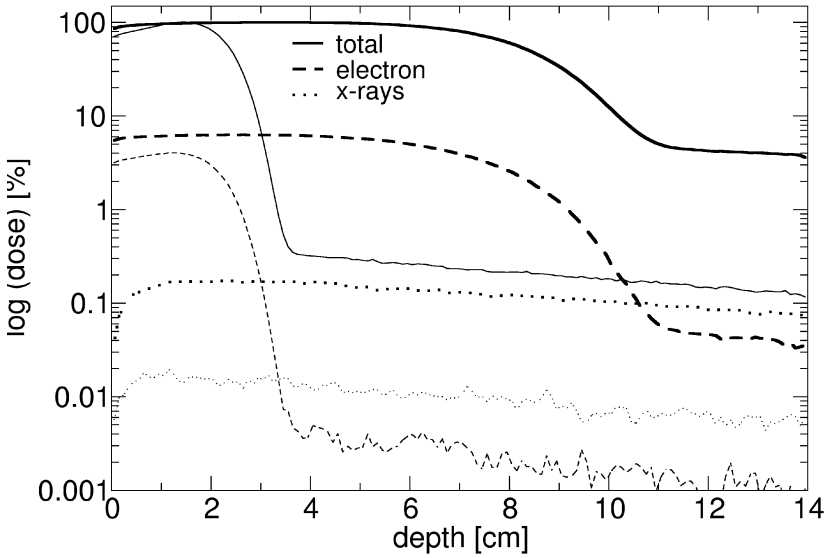

Figure 5.6 Percentage depth dose curves for 6 MeV (thin lines) and 21 MeV (thick lines) electron beams showing dose contribution from total electron beam (solid lines) and scattered electrons (dashed lines) and bremsstrahlung x-rays (dotted lines) from the eMLC. The bottom surface of the leaf banks were at 81.6 cm SCD, the water surface was at 100 cm SSD.

Percentage depth dose curves (normalised to nominal R_{max}) for the eMLC exhibited a lower surface dose (by 2.5 – 4.2% for 6 – 21 MeV), leading to a more deeply penetrating beam (R_{80}, 0.4 – 0.21 cm) than the applicator defined fields (figure 5.5 and table 5.3). The dose beyond the practical range (D_x) of the PDD was 0.1 – 0.4% lower for the eMLC, primarily the result of reduced bremsstrahlung. Figure 5.6 shows the scattered electron and bremsstrahlung dose contributed by the eMLC to the PDD at

6 MeV and 21 MeV for a 10 × 10 cm^2 field at 100 cm SSD. The bremsstrahlung component was 5.0% and 2.0% of the dose at R_x for the 6 MeV and 21 MeV beams, respectively. For the applicator collimated field, the contribution at R_x was 7.5% and 6.0%, respectively (not shown). Electrons scattered from the collimator contributed 3.6 - 5.9% of the dose at 0.5 cm and 2.8 – 3.9% at R_{80} for the eMLC at 6 – 21 MeV. The contribution was 1.7 – 5.0% at 0.5 cm depth and 0.2 – 0.6% at R_{80} for the applicator collimated field.

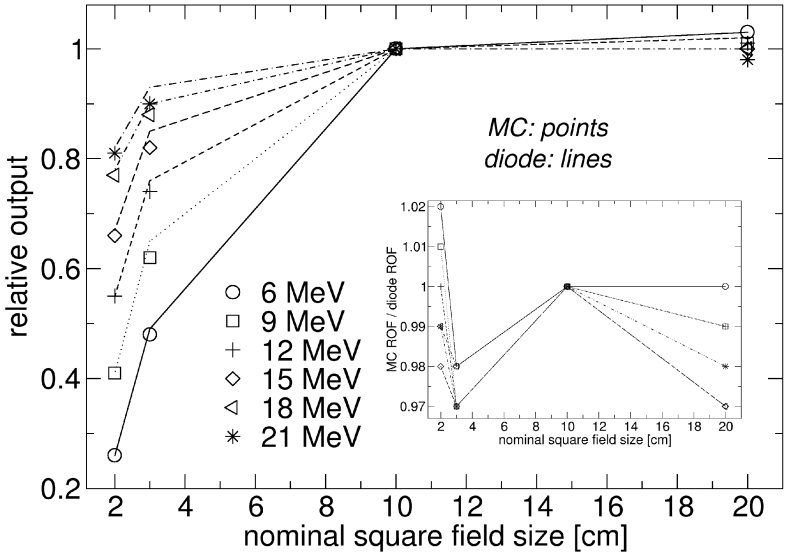

Figure 5.7 Monte Carlo calculated (points) and diode measured (lines) relative output factors for 2 × 2, 3 × 3, 10 × 10 and 20 × 20 cm^2 nominal field sizes collimated with eMLC (relative to 10 × 10 cm^2 field) at 81.6 cm SCD and 100 cm SSD. The ratio of Monte Carlo calculated to diode measured relative output is shown in the inset.

Figure 5.7 shows the Monte Carlo calculated and diode measured relative output factors (ROF) for the 2 – 20 cm square fields at 100 cm SSD. Measurements and calculations were within 2% at 90 cm and 100 cm SSD, with several exceptions. A sharp drop in output was seen for the smaller fields (3×3 cm^2 $\rightarrow$ 2×2 cm^2) at lower beam energies. The eMLC blocks scattered electrons emanating from upstream components and, in addition, for smaller fields the primary source starts to be obscured (Chetty et al. 2007). Conversely, at the largest field size the output was lowest at 21 MeV (0.985) and highest at 6 MeV (1.030) as the result of increasing scatter from the eMLC leaves.

5.3.2 Leaf Resolution

It may be prudent when abutting electron fields to avoid open or shielded regions less than the penumbra width. These narrow fields could provide negligible enhancement to the dose distribution while increasing the scattered radiation in the treatment beam. It was therefore proposed that the eMLC leaf width be such that the dose below a closed leaf section is reduced to less than 50% of maximum dose (of the adjacent open sections). Figure 5.8 shows the dose profile at 1 cm depth for 21 MeV beam at 90 cm SSD for different numbers of eMLC leaves alternating open or closed. The dose dropped to 35.4, 9.6, 5.4 and 4.2% on the central axis blocked by combined leaf widths of 0.4, 0.8, 1.2 and 1.6 cm, respectively. For 6 MeV, the dose dropped to 99.9, 67.5, 35.9

and 19.9%, respectively, for the same configurations. The wider angular distribution of electron scattering at 6 MeV means that the 0.4 – 0.8 cm leaf widths are inadequate. An optimum leaf width of 1.02 cm was determined (for 6 – 21 MeV) based on a quadratic fit of the leaf width versus maximum dose at 1 cm depth in the shield portion of the field. For this leaf width the dose at 6 MeV was reduced to 50% of maximum and 26.2, 16.0, 10.9, 8.30 and 7.2% for 9 – 21 MeV, respectively. A thinner leaf width could be employed at the higher energies to achieve a 50% dose reduction. The leaf width required to provide a 50% reduction in dose was 0.7, 0.6 and 0.4 cm for 9 – 15 MeV, respectively and < 0.4 cm at 18 – 21 MeV.

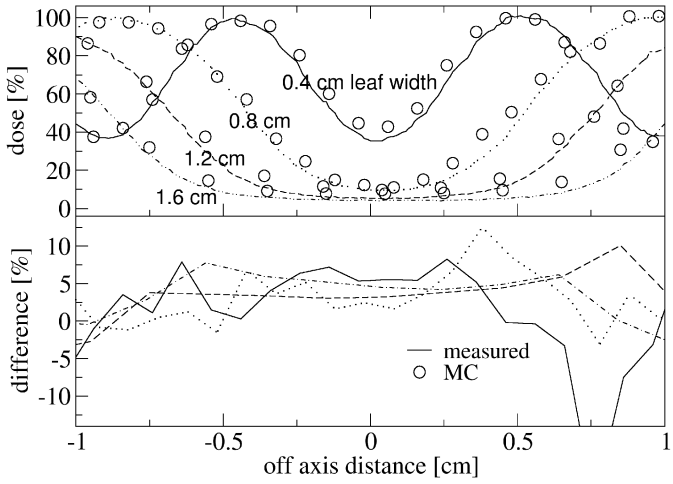

Figure 5.8 Dose profiles with various numbers of adjacent eMLC leaves open or closed (effective leaf widths of 0.4 , 0.8, 1.2 and 1.6 cm perpendicular to the beam) for 21 MeV and 90 cm SSD.

While limiting the leaf width may be prudent in most situations, the availability of thin leaves, conversely, may help improve the uniformity of the dose distribution at the junctions as a (thin) leaf could be added or removed on one side or the other of the junction. For example, the 18 / 21 MeV junction for the wedge field dose distribution (section 5.3.3) required a 2.5 mm gap. This could be approximated in the direction perpendicular to the leaf motion by having a one-leaf (0.2 cm) overlap between the fields.

5.3.3 Field Abutment

Matching of electron beams requires careful determination of the dose at the junction. A shift in the location of the field junction can be used to improve the dose distribution in certain situations. Figure 5.9 shows the dose profile across the field junction of 6 / 9 MeV and 18 / 21 MeV matched 5 cm square fields. The dosimetric effects of field overlaps and gaps of 0.2 cm on the phantom surface are included. The wider penumbrae (6 MeV: 2.01 cm, 9 MeV: 1.49 cm) and scattering of the 6 MeV and 9 MeV beams meant that the dose across the junction was less homogeneous (max. dose – min. dose = 8.9%). There was a hotspot of 112% in the junction region when the field edges were matched. This was reduced by 10% with a 0.2 cm gap. The sharper and comparable penumbrae of the 18 MeV (0.78 cm) and 21 MeV (0.73 cm) beams resulted in a more homogeneous dose distribution in the junction region (max. dose – min. dose = 4.7%).

The sharper penumbra also meant that a shift in the junction position had a larger effect on the junction dose, increasing by 13.3% and reducing by 14.2% for a 0.2 cm overlap and gap, respectively.

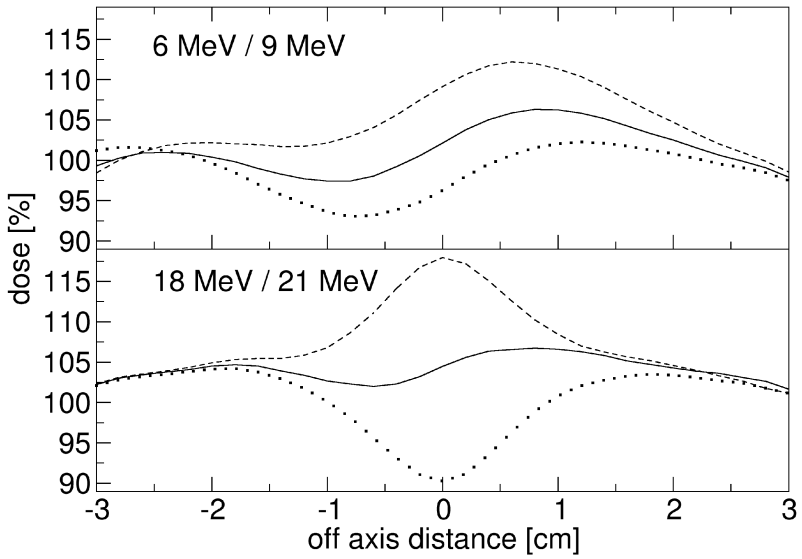

Figure 5.9 Monte Carlo calculated dose profiles for matched 6 MeV / 9 MeV and 18 MeV / 21 MeV, 5 cm square fields shaped with the eMLC (81.6 cm SCD). The dosimetric effects of a 0 cm gap (solid lines), 0.2 cm gap (points) and 0.2 cm overlap (dashed lines) of the field junction at 100 cm SSD are shown.

Monte Carlo calculated and diode measured profile components (6 – 21 MeV) for the wedge shaped dose distribution at 1 cm depth are compared in figure 5.10, demonstrating accurate calculation of the dose and penumbrae in the segments of the

energy modulated field. The wedge distribution was generated using the parameters listed in table 5.4 with the resultant Monte Carlo calculated dose distribution shown in figure 5.11. The field size and junctioning of each wedge component was adjusted to produce the greatest range in depth penetration (R_{50}) and limit the maximum hotspot to 105%. The therapeutic range (R_{80}) and depth penetration (R_{50}) varied from 2.1 – 6.8 cm

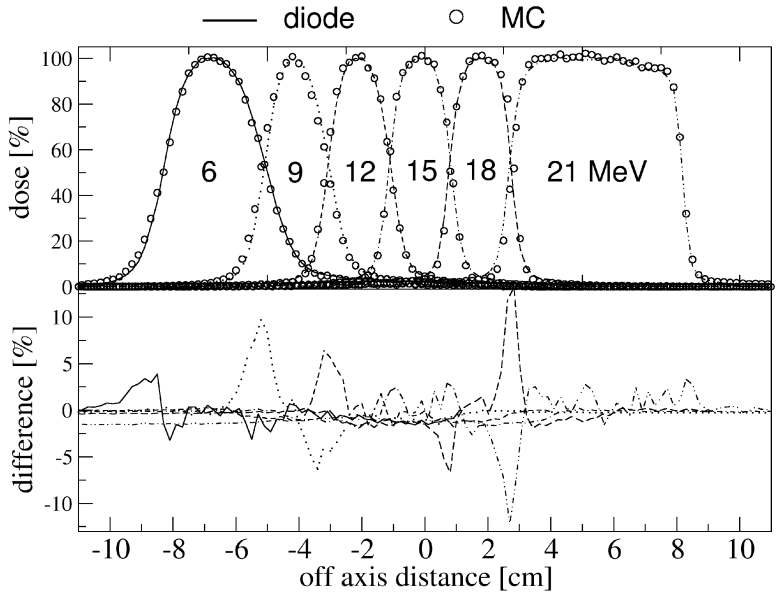

Figure 5.10 Comparison of Monte Carlo calculated and measured dose profiles at 1 cm depth for eMLC energy modulated wedge distribution. The eMLC was positioned at 81.6 cm SCD with a SSD of 100 cm.

and 2.5 – 8.2 cm, respectively. The 21 MeV beam utilised a large field width (5.15 cm) to limit the effects of loss of electronic equilibrium and consequently, achieve

maximum depth penetration. The penumbrae for the field segments used in the wedge shaped dose distribution showed a decrease in width, from 2.1, 1.8, 1.8, 1.5, 1.0 and 0.9 cm for the nominal 10×10 cm^2 field (table 5.2) to 1.7, 1.5, 1.4, 1.2, 0.8 and 0.8 cm for 6 – 21 MeV, respectively. It was necessary to have a gap at the field junctions for the lower energies and an overlap at the higher energies (table 5.4). The 6 MeV and 9 MeV junction required a 0.25 cm gap, while 9 MeV and 12 MeV junction required a 0.05 cm gap. The high energy beam junctions were each overlapped (with there corresponding lower energy abutted beam) by 0.1 cm (15 MeV) – 0.25 cm (21 MeV). The wedge distribution demonstrates the range in depth penetration available with energy modulation at 6 – 21 MeV and highlights the field matching challenge which proved to be particularly challenging at lower energies.

Table 5.4 MCRTP calculated eMLC energy-modulated wedge profile parameters at 100 cm SSD. Field junctions and beam weighting was adjusted so the maximum hotspot did not exceed 105%.

Energy [MeV]	Field size [cm]	Field offset [cm]	Neg. eMLC bank [cm]	Pos. eMLC bank [cm]	Gap [-] or Overlap [+]	Weight [%]
6	2.85	-8.71	-10.14	7.29	-	99
9	3.15	-5.48	-7.03	-3.93	-0.25 cm	84
12	3.05	-2.45	-3.98	-0.92	-0.05 cm	85
15	3.20	0.58	-1.02	2.18	+0.10 cm	84
18	3.15	3.66	2.08	5.24	+0.10 cm	92
21	5.15	7.56	4.99	10.14	+0.25 cm	97

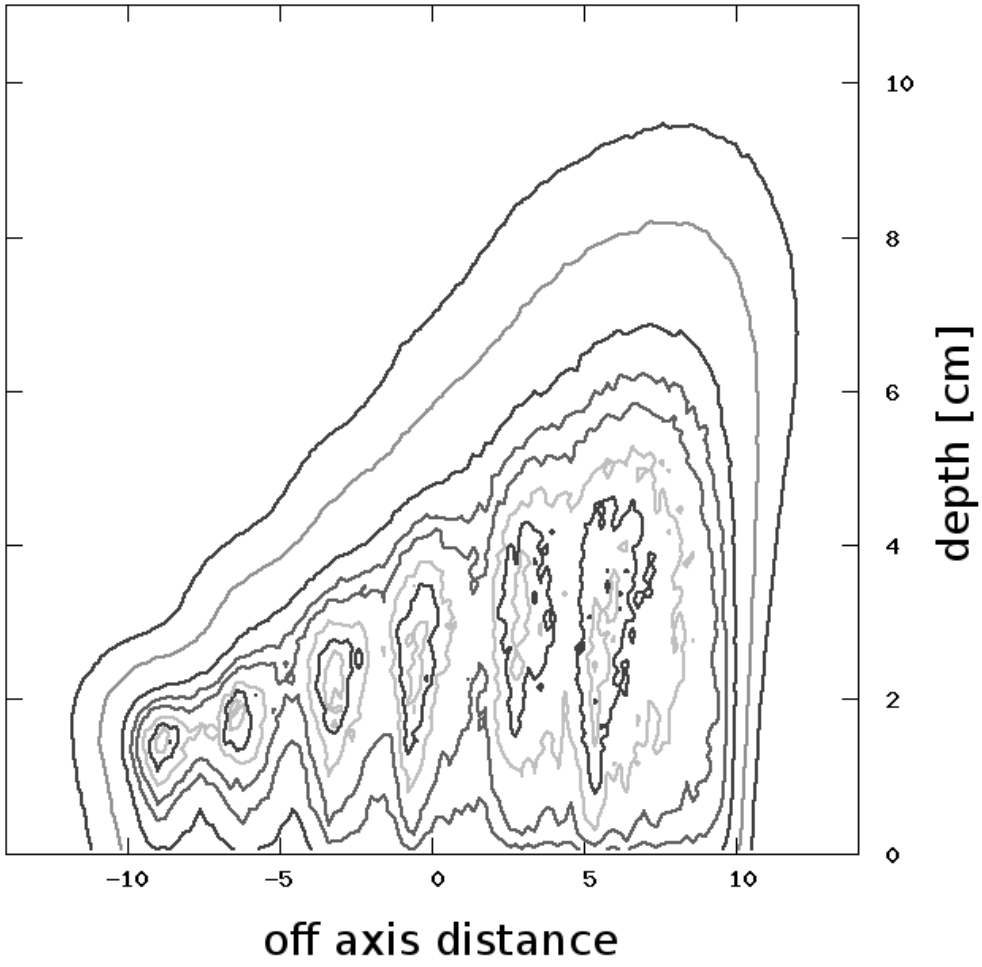

Figure 5.11 Monte Carlo calculated isodose distribution for eMLC (6 - 21 MeV) energy modulated wedge. SCD and SSD were 81.6 cm and 100 cm, respectively. The 20, 50, 80, 90, 95, 100, 103 and 105% isodose lines are displayed. The parameters used to generate the dose distribution are listed in table 5.4.

5.3.4 Patient Plan

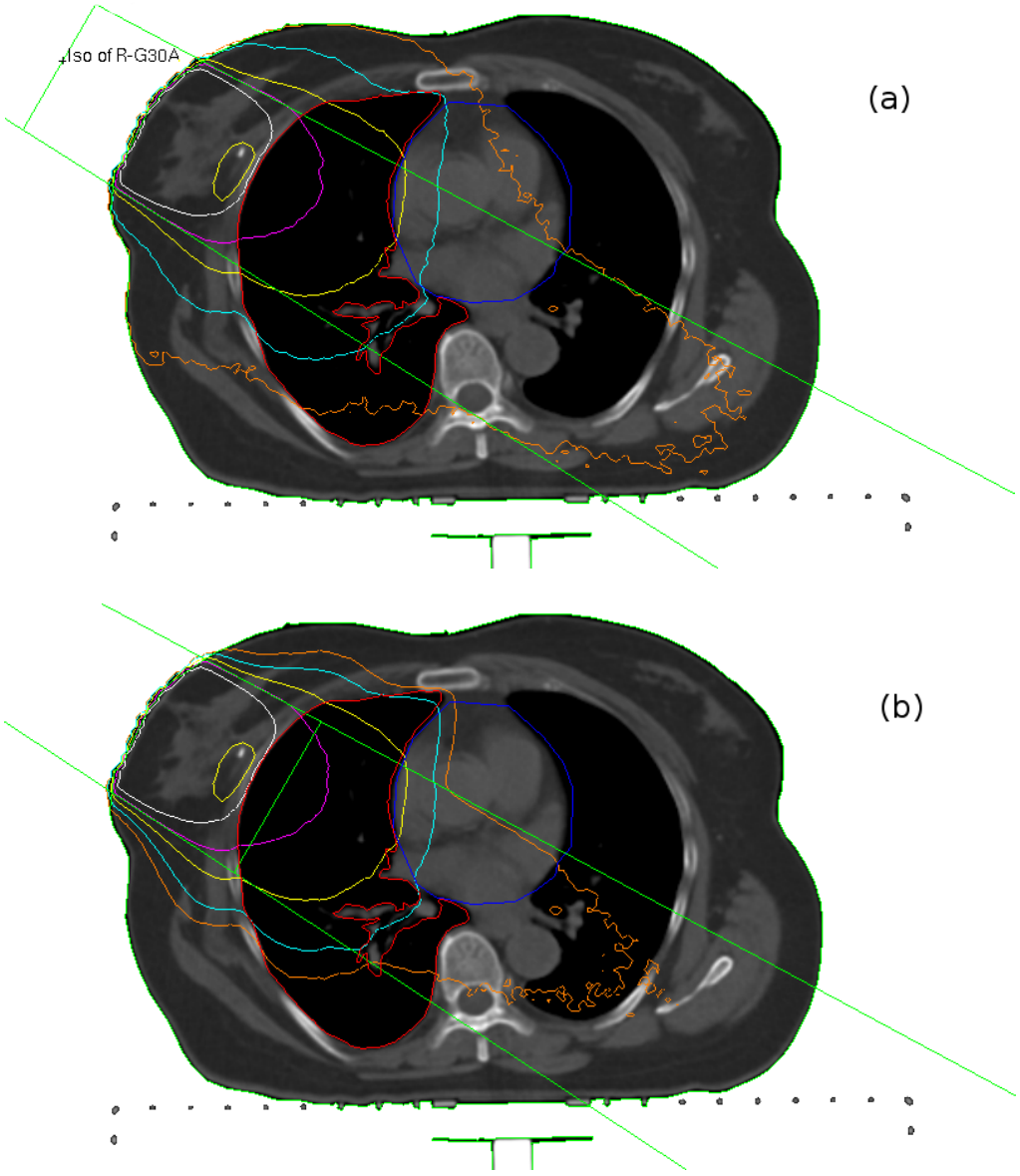

Figure 5.12 Monte Carlo calculated isodose lines displayed in PlanUNC for (a) conventional applicator and (b) eMLC isocentric, electron breast boost using an 18 MeV electron beam. The 2, 5, 20, 50 and 80% isodose lines are shown. Plan parameters are listed in table 5.1.

The Monte Carlo calculated dose distributions for the conventional applicator / SSD and eMLC isocentric electron breast boost plans are shown on patient CT in figure 5.12 (for the applicator plan isocentre CT slice). Bremsstrahlung generated in and transmissed through the 1.3 cm thick cerrobend insert used with the applicator resulted in a wider lateral extension of the 2% and 5% isodose lines. Subsequently, the 2% isodose line encompassed a larger volume of the heart. The 7 cm thick eMLC leaves effectively eliminated bremsstrahlung in the shielded areas and the lateral extension of the 2% and 5% isodose lines was constricted.

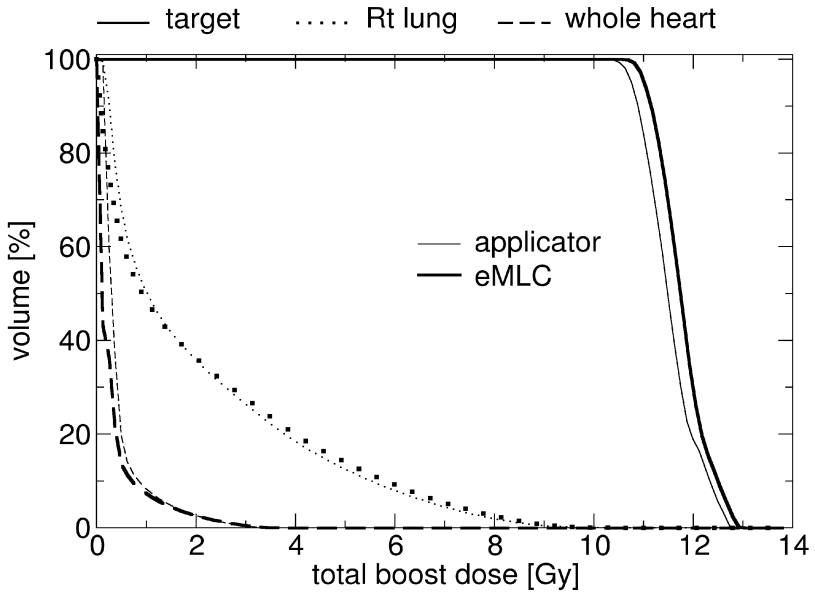

Figure 5.13 Dose-volume histograms (DVH) for conventional applicator and eMLC (concomitant) isocentric electron breast boost using an 18 MeV electron beam. The DVH for the target, Rt lung and whole heart contours are shown. Plan parameters are listed in table 5.1.

The mean dose to the target, right lung and whole heart was 91.8%, 15.8% and 3.0% for the applicator and 93.7%, 15.8% and 2.0%, for the eMLC plan, respectively. The DVHs for these structures are compared in figure 5.13. $D95_{CTV}$ was 107.5% and 110.1% for the standard applicator and eMLC plans, respectively. $V20_{lung}$ was 510.4 cm^3 and 515.9 cm^3, while $V10_{heart}$ was 66.7 cm^3 and 58.6 cm^3, for the applicator and eMLC plans, respectively.

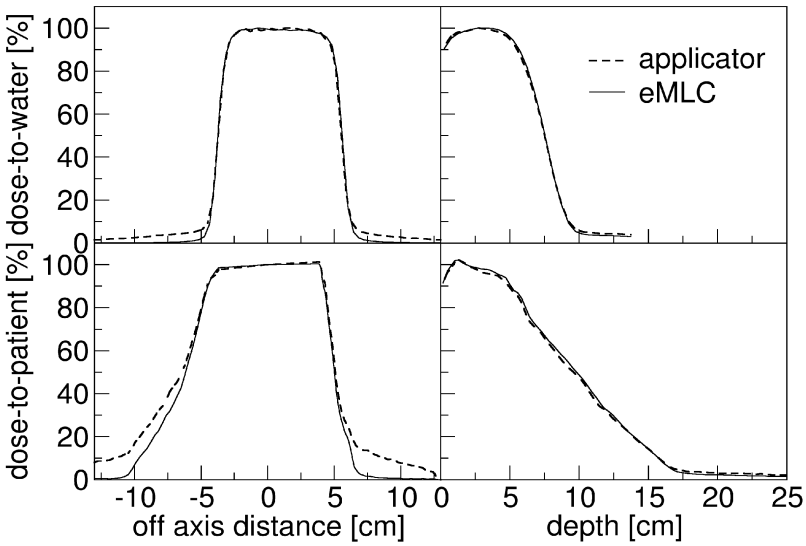

Figure 5.14 Simulated dose profiles and percentage depth dose (PDD) curves for the conventional applicator and eMLC isocentric plans delivered to the water phantom (top row) and the patient (lower row).

The Monte Carlo calculated (20%, 50% and 80%) isodose lines for the

applicator and eMLC plans delivered to a water phantom agreed to within 0.25 cm. Figure 5.14 displays the R_{max} dose profiles and central axis PDD for the two plans. The penumbral width for the eMLC (0.86 cm) and applicator (0.83 cm) plans, which employed the same airgap, agreed to 0.03 (± 0.03) cm. Scattered electrons from the eMLC did not degrade the penumbra. The reduction in dose due to low bremsstrahlung under the eMLC leave banks can be seen in the umbral region for the eMLC plan. The differences in R_{80}, R_{50} and D_x on the central axis were 0.13 cm, 0.06 cm and 0.9% for the two plans. Figure 5.13 includes dose profiles and central axis PDD for the patient. The increased bremsstrahlung for the applicator plan led to the differences seen in the applicator and eMLC dose profiles. The percentage depth dose curves were similar with differences of 0.10 cm, 0.20 cm and 0.9% in R_{80}, R_{50} and the dose at 20 cm depth, respectively.

5.4 SUMMARY AND CONCLUSIONS

An extendable electron multi-leaf collimator (eMLC), which could be positioned at 59 – 95 cm from the source, was investigated for collimation of clinical electron beams. The eMLC was modelled using the Monte Carlo code EGSnrc and validated against percentage depth dose, dose profile and relative output measurements, showing agreement to 2% / 2 mm. The penumbra for a 10 × 10 cm^2 field was up to 0.12 cm narrower for the applicator with a 5 cm air gap compared to the eMLC penumbra at

81.6 cm SCD (18 cm air gap). The main effect on the percentage depth dose curve was a reduction in dose in the build-up region, of up to 4.2% at 0.5 cm depth, with a 0.04 – 0.21 cm shift in R_{80} towards deeper beam penetration.

Scatter from the eMLC contributed 4.0 - 6.3% (6 - 21 MeV) to the dose at the depth of maximum dose, while the 7 cm thick leaves effectively eliminated bremsstrahlung leakage. Field junctioning was a challenge at lower energies due to the wider penumbrae and angular distribution of electron scattering. A Monte Carlo calculated wedge shaped dose distribution consisting of 6 – 21 MeV matched electron fields utilising the entire available field width of the eMLC exhibited a variation in therapeutic range of 2.1 – 6.8 cm.

An isocentric eMLC breast boost plan showed similar target coverage and dose to organs-at-risk as the conventional applicator and fixed source-to-surface distance approach. Dose to the whole heart was reduced as a result of the very low bremsstrahlung contamination from the thick eMLC leaves. Thick leaves may be advantageous for intensity modulated electron therapy techniques where the summation of bremsstrahlung dose from multiple fields can be a concern. The dose profiles and percentage depth dose curves for the eMLC and applicator exhibit very similar characteristics when the airgap between the collimator and patient surface is the same.

Monte Carlo simulation can accurately account for the eMLC and patient in dose calculation for treatment planning. Potential benefits of the eMLC include (i)

faster delivery (no room re-entry to insert applicator), (ii) reduction in risk of positioning errors (using a single isocentre and no couch repositioning) and (iii) a practical method of modulated delivery.

6. Conclusions

6.1 SUMMARY

Monte Carlo simulation has the potential to provide the required 2% / 0.2 cm relative dose calculation accuracy for electron beam therapy treatment planning. This thesis investigated the use of Monte Carlo simulation methods to model clinical electron beams capable of this degree of accuracy. The EGSnrc Monte Carlo user-code BEAMnrc was used to simulate the treatment head of a Siemens Oncor linear accelerator for various configurations. An initial model of the standard electron treatment head was developed based directly on manufacturer specifications (chapter 2). The model used a monoenergetic electron source description tuned to match measured profiles at the depth of dose maximum (to 2%) and depth penetration (to 0.1 cm) for standard applicator defined fields. Measured and calculated extended SSD factors showed agreement to 2%. The model proved useful in explaining some of the physical effects encoutered in extended SSD dosimetry, however, it was restriced to lower beam energies (6 – 12 MeV), four intermediate field sizes (5 cm diameter - 20 × 20 cm^2 applicators) and based on a limited amount of measured data.

An alternative approach to treatment head modelling was adopted in chapter 3 which was based on measurements in large (40 × 40 cm^2) electron fields. This method

took advantage of the absence of widely scattered electrons from the applicator which can obscure details on the electron source and treatment head geometry upstream. The model was comprehensively validated against measured data at 6 – 21 MeV for collimators ranging from the open 25 × 25 cm^2 applicator to a 1 cm diameter cerrobend insert. Monte Carlo calculated and measured dose distributions generally showed agreement of 2% / 0.1 cm. For the 18 MeV and 21 MeV beams, differences of 3% were seen in dose profiles for the largest field. This was attributed to the methods employed to compensate for a fringe field from the bending magnet in the treatment head which was not simulated.

The study in chapter 3 has shown some of the shortcomings in using a limited amount of applicator-collimated measured data to develop accurate electron treatment head models. It also demonstrates that commisioning an electron beam treatment head model using large field measurements is a viable options when asymmetries in the source and head geometry are accounted for. It is interesting to contrast the simple treatment head model of chapter 2 with the more detailed model of chapter 3. In doing so, several observations can be made:

- The electron source in the simple treatment head model was monoenergetic. The spectral composition of the beam largely effects the depth dose fall-off, or gradient, and the use of a monoenergetic source results in a depth dose fall off which is too sharp compared to measurements. The match to measured depth dose

data is improved by use of a Gaussian energy distribution with mean energy selected to match the measured depth penetration (R_{50}) and spectral width adjusted to match the fall-off gradient.

- The detailed treatment head model used a non-zero source angle. This angle was set to direct the beam towards the peak of the dose profile measured in the bremsstrahlung tail (since the x-ray peak in water is dominated by bremsstrahlung from the primary scattering foil). In the simple treatment head model, the beam was directed along the central axis and bremsstrahlung dose was not considered. It is therefore likely that the beam angle in this model is incorrect and the peak in the simulated bremsstrahlung profile is misaligned with that of the real machine.
- The simple treatment head model used an unrealistically broad source angular divergence (of up to 5° at 6 MeV). This was required to match the shoulders of the dose profiles with the exit window absent from the simulation. The Ti exit window significantly broadens the incident electron beam. Using a large angular divergence instead of simulating the exit window will result in a peak in the bremsstrahlung dose profile which is much too broad.
- The detailed model included a number of other adjustments to treatment head geometry, including, the thickness of the primary scattering foil and also the exit window to monitor chamber distance. The primary foil thickness was adjusted to match the ratio of dose in the bremsstrahlung tail to the dose at the depth of dose

maximum (which is justified since the foil thickness is usually not uniform). The exit window to monitor chamber distance was adjusted to match the 40 × 40 cm^2 field edge.

The initial simulations based on large electron field data did not explicity account for the deflection of the electron beam by a fringe magnetic magnetic field from the bending magnet, which extends into the treatment head. Instead, the secondary scattering foil and monitor chamber were unrealistically laterally offset to approximate the effects of beam deflection. This fringe field was subsequently measured and integrated into the BEAMnrc treatment head simulation. The fringe field was found to be a significant contributor to the electron beam in-plane asymmetry (3.5 – 7.6%). With the magnetic field included explicity in simulation, realistic monitor chamber and secondary scattering foil positions were achieved. The measured and simulated 40 × 40 cm^2 field dose profiles agreed to within 3% / 0.2 cm, which is a better match than previously achieved with the foil and monitor chamber in a single position and the fringe field not simulated.

The accurate treatment head model developed was used to investigate collimation of clinical electron beams using an extendable multi-leaf collimator (MLC). The Monte Carlo model was validated against measurements in a water phantom showing agreement of 2% / 0.2 cm in dose profiles, percentage depth dose curves and relative output factors. The penumbra of the MLC, mounted at 81.6 cm source-to-

collimator distance, was 0.1 cm wider than that of the 10 × 10 cm^2 electron applicator, while the dose in the build up region of the depth dose curve was 4% lower (with dose normalised to the nominal depth of maximum dose). The 7 cm thick tungsten MLC leaves added managable scatter to the beam, however, field abutment at lower energies was challenging. An isocentric electron breast boost collimated with the MLC showed similar target coverage and dose to critical structures as the conventional fixed source-to-surface distance approach using an electron applicator. The use of an extendable electron MLC could potentially lead to faster, more accurate and complex treatments.

6.2 FUTURE WORK

It is difficult and very time consuming to produce a full Monte Carlo treatment head model which retains accuracy for all beam energies, standard field sizes and patient positions. Starting with manufacturer specification, there are a large number a tunable parameters relating to the source incident on the exit window (~ 6) and the treatment head geometry details (~ 12). For example, the electron spot may be offset from the central axis as determined by the current in steering coils (inplane) or due to mechanical misalignments (crossplane), the thickness of the primary scattering foil can vary depending on where the beam strikes it and the secondary scattering foil may be offset from the beam axis. The fringe field from bending magnet adds another degree of uncertainty (chapter 4).

The accurate and detailed model of the treatment head developed (chapter 4) could be used to develop a simplified beam model which retains the accuracy needed for treatment planning (Ma et al. 1993, 1994, 1997; Ma and Rogers 1995). In this method, each component of the treatment head can be considered a subsource of particles, each with its own angular and spectral distribution. By analysing the fluence distributions, a beam model could be developed which represents only critical components of the treatment head. The particles from fixed components (e.g. the exit window and scattering foils) could be modeled analytically and represent one subsource. Fluence contributions from the secondary collimator and electron applicator, which are known to vary significantly with field size and airgap (chapter 2) could be fully simulated by Monte Carlo methods. A separate subsource of contaminant bremsstrahlung x-rays could also be introduced.

It may also be possible to develop beam models based on a small number of large field measurements (Janssen et al. 2001). These simplified beam models would be easier to implement clinically and, additionally, a lot faster than a full treatment head simulation.

Dissemination of Research

Journal Publications

O'Shea T P, Foley M J, Rajasekar D, Downes P A, van der Putten W et al 2008 Electron beam therapy at extended SSD: A Monte Carlo investigation *Journal of Applied Clinical Medical Physics* 9 (4) 2811

Faddegon B A, Sawkey D L, O'Shea T P, McEwen M and Ross C 2009 Treatment head disassembly to improve the accuracy of large electron field simulation *Medical Physics* 36 (10) 4577–4591

O'Shea T P, Sawkey D L, Foley M J and Faddegon B A 2010 Monte Carlo commissioning of clinical electron beams using large field measurements *Physics in Medicine & Biology* 55 4083-4105

O'Shea T P, Foley M J and Faddegon B A 2011 Accounting for the fringe magnetic field from the bending magnet in a Monte Carlo accelerator treatment head simulation *Medical Physics* 38 3260

O'Shea T P, Ge Y, Foley M J and Faddegon B A 2011 Characterisation of an Extendable Multi-leaf Collimator for Clinical Electron Beams *Physics in Medicine and Biology* (Submitted August 2011)

Proffered Conference Presentations

O'Shea T, B Faddegon, D Sawkey, M Foley 2009 Improved Monte Carlo simulation of small electron fields 51st AAPM Annual Meeting Anaheim, CA *Medical Physics* 36 (6)

O'Shea T P, Sawkey D L, Foley M J, Faddegon B A 2009 Improved simulation of small electron fields for external beam radiation therapy *Proceedings of the World congress on Medical Physics & Biomedical Engineering* 25 (1) Munich, Germany Springer

Ge Y, O'Shea T and Faddegon B 2010 X-Ray Plus Electron Radiotherapy with An Extendable MLC 52nd AAPM Annual Meeting Philadelphia, PA *Medical Physics* 36 (6)

O'Shea T P, Sawkey D L, Foley M J, Faddegon B A 2010 Accounting for the Effect of a Magnetic Field From the Bending Magnet in Monte Carlo Accelerator Treatment Head Simulation 52nd AAPM Annual Meeting Philadelphia, PA *Medical Physics* 36 (6)

Faddegon B A, Sawkey D, OShea T and Schreiber E 2011 The accuracy of linear accelerator treatment head simulation with condensed history codes *International Workshop on Recent Advances in Monte Carlo Techniques in Radiation Therapy*, Montreal, Canada: www.medphys.mcgill.ca/~ws2011/Abstract_book_files/Binder1.pdf

Bibliography

Almond P R, Biggs P J, Coursey B M, Hanson W F, Saiful Huq M, Nath Ravinder and Rogers D W O 1999 AAPM's TG-51 protocol for clinical reference dosimetry of high-energy photon and electron beams *Medical Physics* 26 1847–70

Antolak J A, Bieda M R and Hogstrom K R 2002 Monte Carlo methods to commission electron beams: a feasibility study *Medical Physics* 29 771–86

Attix F H 1986 *Introduction to radiological physics and radiation dosimetry* Berlin Wiley-VCH

Bartelink H, Horiot J-C, Poortmans P, Struikmans H, Van den Bogaert W, Barillot I, Fourquet A, Borger J, Jager J, Hoogenraad W, Collette L and Pierart M 2001 Recurrence Rates after Treatment of Breast Cancer with Standard Radiotherapy with or without Additional Radiation *New England Journal of Medicine* 345 (19) 1378-1387

Bass G, Thomas R and Pearce J 2009 The calibration of parallel-plate electron ionization chambers at NPL for use with the IPEM 2003 code of practice: summary data *Physics in Medicine and Biology* 54 N115–24

Batchelor A, Bewley D K, Morrison R, Stevenson J A 1959 Electron therapy at 8 MeV. *British Journal of Radiology* 32 (377) 332-338

Berger M I and Seltzer S M 1969 RSIC Computer Code Collection CCC-107: ETRAN Monte Carlo code system for electron and photon transport through extended media. *Radiation Shielding Information Center*, Oak Ridge Natl. Lab.

Berger M J 1963 Monte Carlo Calculation of the penetration and diffusion of fast charged particles In: Alder B, Fernbach S, and Rotenberg M, editors *Methods in Computational Physics* 1 135 – 215 Academic (NY)

Berger M J and Wang R 1988 Multiple-scattering angular deflections and energy-loss straggling In: Jenkins T M, Nelson W R and Rindi A(Eds.) *Monte Carlo Transport of Electrons and Photons* Plenum Press (NY) p. 21

Bethe H A 1953 Molière's Theory of Multiple Scattering *Physical Review* 89 1256–1266

Bielajew 1993 The effect of strong longitudinal magnetic fields on dose deposition from electron and photon beams *Medical Physics* 20 1171–9

Bielajew A F and Rogers D W O Electron Step-Size Artefacts and PRESTA In: *Monte Carlo Transport of Electrons and Photons* edited by Jenkins T M, Nelson W R, Rindi A, Nahum A E and Rogers D W O 115 - 137 Plenum Press (NY)

Björk P, Knöös T and Nilsson P 2002 Influence of initial electron beam characteristics on Monte Carlo calculated absorbed dose distributions for linear accelerator electron beams *Physics in Medicine and Biology* 47 4019-4041

Boyd R A, Hogstrom K R and Starkschall G 2001 Electron pencil-beam redefinition algorithm dose calculations in the presence of heterogeneities *Medical Physics* 28 2096

Brahme A 1975 Simple relations for the penetration of high energy electrons in matter *SSI: 1975-011 National Institute of Radiation Protection*, Stockholm, Sweden

Buckley L A and Rogers D W O 2006 Wall correction factors, Pwall, for parallel-plate ionization chambers *Medical Physics* 33 (6) 1788-96

Burns D, Ding G, and Rogers D W O 1996 R50 as a beam quality specifier for selecting stopping-power ratios and reference depths for electron dosimetry *Medical Physics* 23 383 – 388

Chen J, Irion J and Faddegon B 2009 Validation of the final aperture superposition technique to calculate electron output factors and depth dose curves *Medical Physics* 36 3397–405

Chetty I J et al 2007 Report of the AAPM Task Group No. 105: issues associated with clinical implementation of Monte Carlo-based photon and electron external beam treatment planning *Medical Physics* 34 4818–53

Coleman J, Park C, Villarreal-Barajas J E, Petti P and Faddegon B 2005 A comparison of Monte Carlo and Fermi-Eyges-Hogstrom estimates of heart and lung dose from breast electron boost treatment International *Journal of Radiation Oncology Biology Physics* 61 (2) 621-628

Cygler J E, Daskalov G M, Chanb G H and Ding G X 2004 Evaluation of the first commercial Monte Carlo dose calculation engine for electron beam treatment planning *Medical Physics* 31 (1) 142-153

Cygler J, Allen Li X, Ding G X and Lawrence E 1997 Practical approach to electron beam dosimetry at extended SSD *Physics in Medicine and Biology* 42 1505–14

Das I J, Ding G X and Ahnesjo A 2008 Small fields: nonequilibrium radiation dosimetry *Medical Physics* 35 206–15

Das I J, McGee K K and Cheng C W 1995 Electron-beam characteristics at extended treatment distances *Medical Physics* 22 1667–74

Das I J, Zhu T C, Cheng C-W Watts R J Ahnesjo A, Gibbons J Li X A, Lowenstein J, Mitra R K and Simon W E 2008 Accelerator beam data commissioning equipment and procedures: Report of the TG-106 of the Therapy Physics Committee of the AAPM *Medical Physics* 35 4186

Ding G X, Rogers D W, Mackie T R 1995 Calculation of stopping-power ratios using realistic clinical electron beams *Medical Physics* 22 (5) 489-501

du Plessis F C, Wilemse C A, Lotter M G and Goedhals L 1998 The indirect use of CT numbers to establish material properties needed for Monte Carlo calculation of dose distributions in patients *Medical Physics* 25 1195-1201

Ebert M A and Hoban P W 1995 A model for electron-beam applicator scatter *Medical Physics* 22(9) 1419-1429

Eldib A, ELGohary M, Fan J, Jin L, Li J, Ma C, Elsherbini N 2010 Dosimetric characteristics of an electron multileaf collimator for modulated electron radiation therapy *Journal of Applied Clinical Medical Physics* 11 (2) 5-22

Enge H A 1963 Achromatic Magnetic Mirror for Ion Beams *Review of Scientific Instruments* 34 385

Eyges L 1948 Multiple Scattering with Energy Loss *Physical Review* 74 1534–1535

Faddegon B A, Asai M A, Perl J, Tinslay J, ross C, Sempau and Salvat F Benchmarking of Monte Carlo simulation of bremsstrahlung from thick targets at radiotherapy energies *Medical Physics* 35 4308

Faddegon B A, Balogh J, Mackenzie R and Scora D 1998 Clinical considerations of Monte Carlo for electron radiotherapy treatment planning *Radiation Physics and Chemistry* 53 217–27

Faddegon B A, Kawrakow I, Kubyshin Y, Perl J, Sempau J and Urban L 2009 The accuracy of EGSnrc, Geant4 and PENELOPE Monte Carlo systems for the simulation of electron scatter in external beam radiotherapy *Physics in Medicine and Biology* 54 6151

Faddegon B A, Perl J and Asai M 2008 Monte Carlo simulation of large electron fields *Physics in Medicine and Biology* 53 1497-1510

Faddegon B A, Sawkey D L, O'Shea T P, McEwen M and Ross C 2009 Treatment head disassembly to improve the accuracy of large electron field simulation *Medical Physics* 36 (10) 4577-91

Faddegon B A, Schreiber E and Ding X 2005 Monte Carlo simulation of large electron fields *Physics in Medicine and Biology* 50 741–53

Fix M K, Frei D, Volken W, Neuenschwander H, Born E J and Manser P 2010 Monte Carlo dose calculation improvements for low energy electron beams using eMC *Physics in Medicine and Biology* 55 4577

Fraser D J, Wong P, Sultanem K and Verhaegen F 2010 Dosimetric evolution of the breast electron boost target using 3D ultrasound imaging *Radiotherapy and Oncology* 96 (2) 185-91

Gauer T, Albers D, Cremers F, Harmansa R, Pellegrini R and Schmidt R 2006 Design of a computer-controlled multileaf collimator for advanced electron radiotherapy *Physics in Medicine and Biology* 51 5987

Gauer T, Sokoll J, Cremers F, Harmansa R, Luzzara M and Schmidt R 2008 Characterization of an add-on multileaf collimator for electron beam therapy *Physics in Medicine and Biology* 53 1071

Ge Y, O'Shea T and Faddegon B 2010 X-Ray Plus Electron Radiotherapy with An Extendable MLC *Medical Physics* 37 3375

Gerbi B J, Higgins P D, Khan F M, Antolak J A, Herman M G, Deibel F C, Followill D S, Huq M S, Mihailidis D N, Yorke E D, Hogstrom K R 2009 Recommendations for clinical electron beam dosimetry: supplement to the recommendations of Task Group 25 *Medical Physics* 36 3239–79

Ginzton E L and Hunan C S 1985 History of Microwave Linear Accelerators in Radiation Therapy *International Journal of Radiation Oncology Biology Physics* 11 (2) 205-216

Goldman U, Wennberg B, Svane G, Bylund H, Pehr Lind P 2010 Reduction of radiation pneumonitis by V20-constraints in breast cancer *Radiation Oncology* 5 (99) 1-6

Goudsmit S and Saunderson J L 1940 Multiple Scattering of Electrons *Physical Review* 57 24–29

Greene D and Williams P C 1997 *Linear Accelerators for Radiation Therapy* Second Edition New York (NY) Taylor and Francis Group, LLC

Hendee W R, Ibbott G S and Hendee E G 2005 *Radiation Therapy Physics* Hoboken (NJ) Wiley

Hogstrom K R and Almond P R 2006 Review of electron beam therapy physics *Physics in Medicine and Biology* 51 R455–89

Hogstrom K R, Antolak J A, Kudchadker R J, Ma C-M and Leavitt D D 2003 Modulated Electron Therapy *AAPM Summer School Intensity Modulated Radiation Therapy* Colorado College www.aapm.org/meetings/03SS

Hogstrom K R, Boyd R A, Antolak J A, Svatos M, Faddegon B and Rosenman J G 2004 Dosimetry of a prototype retractable eMLC for fixed-beam electron therapy *Medical Physics* 31 443

Hogstrom K R, Mills M D and Almond P R 1981 Electron beam dose calculations *Physics in Medicine and Biology* 26 (3) 445-459

Hu Y A, Song H, Chen Z, Zhou S and Yin F-F 2008 Evaluation of an electron Monte Carlo dose calculation algorithm for electron beams Journal Appl. Clin. *Medical Physics* 9 (3) 1

Huang V W, Seuntjens J, Devic S and Verhaegen F 2005 Experimental determination of electron source parameters for accurate Monte Carlo calculation of large field electron therapy *Physics in Medicine and Biology* 50 779-786

Huq M S and Andreo P 2004 Advances in the determination of absorbed dose to water in clinical high-energy photon and electron beams using ionization chambers *Physics in Medicine and Biology* 49 R49–104

ICRU 1972 Radiation dosimetry: Electrons with initial energies between 1 and 50 MeV *ICRU Report 21* (Bethesda,MD: International Commission on Radiation Units and Measurements)

ICRU 1984 Radiation Dosimetry: Electron beams with energies between 1 and 50 MeV *ICRU Report 35* (Bethesda,MD: International Commission on Radiation Units and Measurements)

Janssen J J, Korevaar E W, van Battum L J, Storchi P R M and Huizenga H 2001 A model to determine the initial phase space of a clinical electron beam from measured data *Physics in Medicine and Biology* 46 269–86

Jiang S B, Kapur A and Ma C-M 2000 Electron beam modeling and commissioning for Monte Carlo treatment planning *Medical Physics* 27 180

Jin L, Ma C-M, Fan J, Eldib A, Price R A, Chen L, Wang L, Chi Z, Xu Q, Sherif M and Li J S 2008 Dosimetric verification of modulated electron radiotherapy delivered using a photon multileaf collimator for intact breasts *Physics in Medicine and Biology* 53 (21) 6009

Kapur A, Ma C M, Mok E C, O Findley D and Boyer A L 1998 Monte Carlo calculations of electron beam output factors for a medical linear accelerator *Physics in Medicine and Biology* 43 3479-3494

Karzmark C J 1984 Advances in Linear Accelerator design for Radiotherapy *Medical Physics* 11 (2) 105-127

Karzmark C J, Nunan C S and Tanabe E 1993 *Medical Electron Accelerators* McGraw-Hill ISBN-13: 978-0071054102

Kawrakow I 2000 Accurate condensed history Monte Carlo simulation of electron transport.I. EGSnrc, the new EGS4 version *Medical Physics* 27 (3)
485-498

Kawrakow I 2001 VMC++, electron and photon Monte Carlo calculations optimized for Radiation Treatment Planning Advanced Monte Carlo for Radiation Physics, Particle Transport Simulation and Applications. *Proceedings of the Monte Carlo 2000 Conference 229*

Kawrakow I and Bielajew A F 1998 On the representation of electron multiple elastic-scattering distributions for Monte Carlo calculations *Nuclear Instruments and Methods in Physics Research Section B: Beam Interactions with Materials and Atoms* 134 (3-4) 325-336

Kawrakow I and Rogers D W O 2006 The EGSnrc code system: Monte Carlo simulation of electron and photon transport *NRCC Report PIRS-701*

Kawrakow I and Walters B R B 2006 Efficient photon beam dose calculations using DOSXYZnrc with BEAMnrc *Medical Physics* 2006 33(8) 3046-3056

Kawrakow I, Fippel M and Friedrich K 1996 3D electron dose calculation using voxel based Monte Carlo algorithm (VMC) *Medical Physics* 23 445–57

Kawrakow I, Mainegra-Hing E, Rogers D W O, Tessier F and Walters B R B 2011 The EGSnrc Code System: Monte Carlo Simulation of Electron and Photon Transport *NRCC Report PIRS-701*

Khan F M 2003 *The Physics of Radiation Therapy* 3rd edition Philadelphia (PA) Lippincott, Williams & Wilkins

Khan F M, Doppke K P, Hogstrom K R, Kutchner G J, Nath R, Prasad S C, Purdy J A, Rozenfeld M and Werner B L 1991 Clinical electron-beam dosimetry: Report of AAPM Radiation Therapy Committee Task Group 25 *Medical Physics* 18 73–109

Khan FM 1984 *The Physics of Radiation Therapy* Baltimore (MD) Williams and Wilkins

Kirkby C, Stanescu T, Rathee S, Carlone M, Murray B and Fallone B G 2008 Patient dosimetry for hybrid MRI-radiotherapy systems *Medical Physics* 35 (3) 1019

Klein E E 1998 Modulated electron beams using multi-segmented multileaf collimation *Radiotherapy and Oncology* 48 (3) 307-311

Klein E E, Mamalui-Hunter M and Low D A 2009 Delivery of modulated electron beams with conventional photon multi-leaf collimators *Physics in Medicine and Biology* 54 327

Klein E E, Vicic M, Ma C-M, Low D L and Drzymala R E 2008 Validation of calculations for electrons modulated with conventional photon multileaf collimators *Physics in Medicine and Biology* 53 1183

Kudchadker R J, Hogstrom K R, Garden A S, McNeese M D, Boyd R A and Antolak J A 2002 Electron conformal radiotherapy using bolus and intensity modulation *International Journal of Radiation Oncology Biology Physics* 53 (4) 1023-1037

Lee M C and Ma C-M 2000 Monte Carlo characterization of clinical electron beams in transverse magnetic fields *Physics in Medicine and Biology* 45 (10) 2947

Lee M C, Jiang S B and Ma C-M 2000 Monte Carlo and experimental investigations of multileaf collimated electron beams for modulated electron radiation therapy *Medical Physics* 27 2708

Li Z A, Naqvi S, Chu J and Reiffel L 2001 Conformal photon-beam therapy with transverse magnetic fields: A Monte Carlo study *Medical Physics* 28 127

Ma C M and Jiang S 1999 Monte Carlo modelling of electron beams from medical accelerators *Physics in Medicine and Biology* 44 157–89

Ma C M and Rogers D W O 2005 BEAMDP as a General-Purpose Utility *NRCC Report PIRS-0509(E)revA*

Ma C M and Rogers D W O 2009 BEAMDP as a General-Purpose Utility *NRCC*

Report PIRS-0509

Ma C M, Ding M, Li J S, Lee M C, Pawlicki T and Deng J 2003 A comparative dosimetric study on tangential photon beams, intensity-modulated radiation therapy (IMRT) and modulated electron radiotherapy (MERT) for breast cancer treatment *Physics in Medicine and Biology* 48 909–24

Ma C-M, Faddegon B, Rogers D W O and Mackie T R 1997 Accurate characterization of Monte Carlo calculated electron beams for rediotherapy *Medical Physics* 24 (3) 401-416

Ma C-M, Rogers D W O, Ding G X, Wei J S and Mackie T R 1994 Electron beam characterization: Reconstruction models and dose distributions in a homogeneous phantom *Medical Physics* 21 895

Ma C-M, Rogers D W O, Faddegon B, Ding G X, Wei J S, Bielajew A F and Mackie T R 1993 Simplified models of electron beams from a 2100C accelerator *Medical Physics* 20 1295

McGowan H C E, Faddegon B A and Ma C M 2005 STATDOSE for 3D dose distributions *NRCC Report PIRS-0509(F)*

Metropolis N 1987 The beginning of the MC method *Los Alamos Sci* 15 125-130

Metropolis N and Ulam S 1949 The Monte Carlo Method *Journal of the American Statistical Association* 247 44 335-341

Meyer J A, Palta J R and Hogstrom K R 1984 Determination of relatively new electron dosimetry measurement techniques on Mevatron 80 *Medical Physics* 1984 11 670-677

Nahum A E 1999 Condensed-history Monte-Carlo simulation for charged particles: what can it do for us? *Radiation Environmental Biophysics* 38 (3) 163-73

Nelson W R, Hirayama H and Rogers D W O 1985 *EGS4 User Manual SLAC-265 Appendix 2*

Neuenschwander H, Mackie T R and Reckwerdt P J 1995 MMC-a high-performance Monte Carlo code for electron beam treatment planning *Physics in Medicine and Biology* 40 543

Oline L, Krispel F and Sagalovsky L 1990 Simulation of Magnetic Optics in the Focusing Magnet of a Medical Accelerator *2nd European Particle Accelerator Conference (EPAC 90) Proceedings* 1807

Ostwald P M, Metcalfe P E, Denham J W and Hamilton C S 1994 A comparison of three electron planning algorithms for a 16 MeV electron beam *Medical Physics* 28 (3) 731-740

Pavon E C, Sanchez-Doblado F, Leal A, Capote R, Lagares J I, Perucha M and Arrans R 2003 Total skin electron therapy treatment verification: Monte Carlo simulation and beam characteristics of large non-standard electron fields *Physics in Medicine and Biology* 48 2783–96

Perkins G H, McNeese M D, Antolak J A, Buchholz T A, Strom E A and Hogstrom K R 2001 A custom three-dimensional electron bolus technique for optimization of postmastectomy irradiation *International Journal of Radiation Oncology Biology Physics* 51 (4) 1142-1151

Podgorsak E B 2005 *Radiation Oncology Physics: A Handbook for Teachers and Students* Vienna, Austria, International Atomic Energy Agency

Popescu I A, Shaw C P, Zavgorodni S F and Beckham W A 2005 Absolute dose calculations for Monte Carlo simulations of radiotherapy beams *Physics in Medicine and Biology* 50 3375–92

Rajasekar D, Datta N R, Maria Das K J and Ayyagari S 2002 Electron beam therapy at extended SSD: an analysis of output correction factors for a Mitsubishi linear accelerator *Physics in Medicine and Biology* 47 3301–3311

Reynaert N, van der Marcka S C, Schaarta D R, Van der Zeea W, Van Vliet-Vroegindeweija C, Tomseja M, Jansena J, Heijmena B, Coghea M and De Wagtera C 2007 Monte Carlo treatment planning for photon and electron beams *Radiation Physics and Chemistry* 76 (4) 643-686

Rogers D W O 2006 Fifty years of Monte Carlo simulations for medical physics *Physics in Medicine and Biology* 51 R287–R301

Rogers D W O and Bielajew A F 1990 In: Kase K, Bjarngard B, Attix F H (Eds.) *The Dosimetry of Ionizing Radiation* Academic Press (NY) 3 427-539

Rogers D W O, Faddegon B A, Ding G X, Ma C M and We J 1995 BEAM: A Monte Carlo code to simulate radiotherapy treatment units *Medical Physics* 22 (5) 503-524

Rogers D W O, Walters B and Kawrakow I 2005 BEAMnrc Users Manual *NRCC Report PIRS-0509(A)revK*

Rogers D W O, Walters B and Kawrakow I 2006 BEAMnrc users manual *NRCC Report PIRS-0509(A)revK*

Rogers D W O, Walters B, Kawrakow I 2009 BEAMnrc Users Manual *NRCC Report PIRS-0509(A)revL*

Ross C K, McEwen M R, McDonald A F, Cojocaru C D and Faddegon B A 2008 Measurement of multiple scattering of 13 and 20 MeV electrons by thin foils *Medical Physics* 35 4121

Saw C B, Ayyangar K M, Pawlicki Todd and Korb L J 1995 Dose distribution considerations of medium energy electron beams at extended source-to-surface distance *International Journal of Radiation Oncology Biology Physics* 32 (1) 159-164

Sawkey D L and Faddegon B A 2009 Determination of electron energy, spectral width, and beam divergence at the exit window for clinical megavoltage x-ray beams *Medical Physics* 36 698

Sawkey D L and Faddegon B A 2009 Simulation of large x-ray fields using

independently measured source and geometry details *Medical Physics* 36 698–707

Schreiber E C and Faddegon B A 2005 Sensitivity of large-field electron beams to variations in a Monte Carlo accelerator model *Physics in Medicine and Biology* 50 769

Schreiber E, Tracton G, and Chaney E 2006 Tools for Integrating Monte Carlo Dose Engines with a Radiotherapy Planning System *Medical Physics* 33 2146

Shiu A S and Hogstrom K R 1991 Pencil-beam redefinition algorithm for electron dose distributions *Medical Physics* 18 7-18

Siebers J V, Keall P J, Nahum A E and Mohan R 2000 Converting absorbed dose to medium to dose to water for Monte Carlo based photon beam dose calculations *Physics in Medicine and Biology* 45 983-998

Song H, Ahmad M, Deng J, Chen Z, Yue N J and Nath R 2006 Limitations of silicon diodes for clinical electron dosimetry *Radiation Protection Dosimetry* 120 56–9

Spencer LV and Attix F H 1955 A Theory of Cavity Ionisation *Radiation Research* 3 (3)

Steel J, Stewart A, and Satory P 2009 Matching extended-SSD electron beams to multileaf collimated photon beams in the treatment of head and neck cancer *Medical Physics* 36 4244

Thwaites D I, DuSautoy A R, Jordan T, McEwen M R, Nibet A, Nahum A E and

Pitchford W G 2003 The IPEM code of practice for electron dosimetry for radiotherapy beams of initial energy from 4 to 25 MeV based on an absorbed dose to water calibration *Physics in Medicine and Biology* 48 2929-2970

Turian J V, Smith B D, Bernard D A, Griem K L and Chu J C 2004 Monte Carlo calculations of output factors for clinically shaped electron fields *Journal of Applied Clinical Medical Physics* 5 42–63

van Battum L J 2003 Scattered radiation from applicators in clinical electron beams *Physics in Medicine and Biology* 48 2493–507

Vatanen T, Traneus E and Lahtinen T 2009 Comparison of conventional inserts and an add-on electron MLC for chest wall irradiation of left-sided breast cancer *Acta Oncologica* 48 (3) 446-451

Verhaegen F, Mubata C, Pettingel J, Bidmead A M, Rosenberg I, Mockridge D and Nahum A E 2001 Monte Carlo calculation of output factors for circular, rectangular, and square fields of electron accelerators (6–20 MeV) *Medical Physics* 28 938–49

Walters B R B, Kawrakow I and Rogers D W O 2002 History by history statistical estimators in the BEAM code system *Medical Physics* 29 2745

Walters B, Kawrakow I and Rogers D W O 2011 DOSXYZnrc Users Manual *NRCC Report PIRS-794revB*

Walters B, Kawrakow I, Rogers D W O 2005 DOSXYZnrc Users Manual *NRCC*

Report PIRS-794revB

Wang L L W and Rogers D W O 2007 Monte Carlo study of Si diode response in electron beams *Medical Physics* 34 1734–42

Weinberg R, Antolak J A, Starkschall G, Kudchadker R J, White R A and Hogstrom K R 2009 Influence of source parameters on large-field electron beam profiles calculated using Monte Carlo methods *Physics in Medicine and Biology* 54 105-116

Wideröe R 1928 Über ein neues Prinzip zur Herstellung hoher Spannungen *Archiv für Elektrotechnik* 21 387

Yang J, Li J S, Qin L, Xiong W and Ma C M 2004 Modelling of electron contamination in clinical photon beams for Monte Carlo dose calculation *Physics in Medicine and Biology* 49 2657–2673

Zackrisson B and Karlsson M 1996 Matching of electron beams for conformal therapy of target volumes at moderate depths *Radiotherapy and Oncology* 39 (3) 261-270

Zhang G G, Rogers D W O, Cygler J E and Mackie T R 1998 Effects of changes in stopping-power ratios with field size on electron beam relative output factors *Medical Physics* 25 (9) 1711-1716

Zhang G G, Rogers D W O, Cygler J E, and Mackie T R. 1999 Monte Carlo investigation of electron beam output factors versus size of square cutout *Medical Physics* 26(5) 743-750